Characterization of a fully equipped ALICE TPC Readout Chamber

Charakterisierung einer vollständig ausgestatteten ALICE TPC Auslesekammer

Diplomarbeit von Michael Linus Knichel
Mai 2009

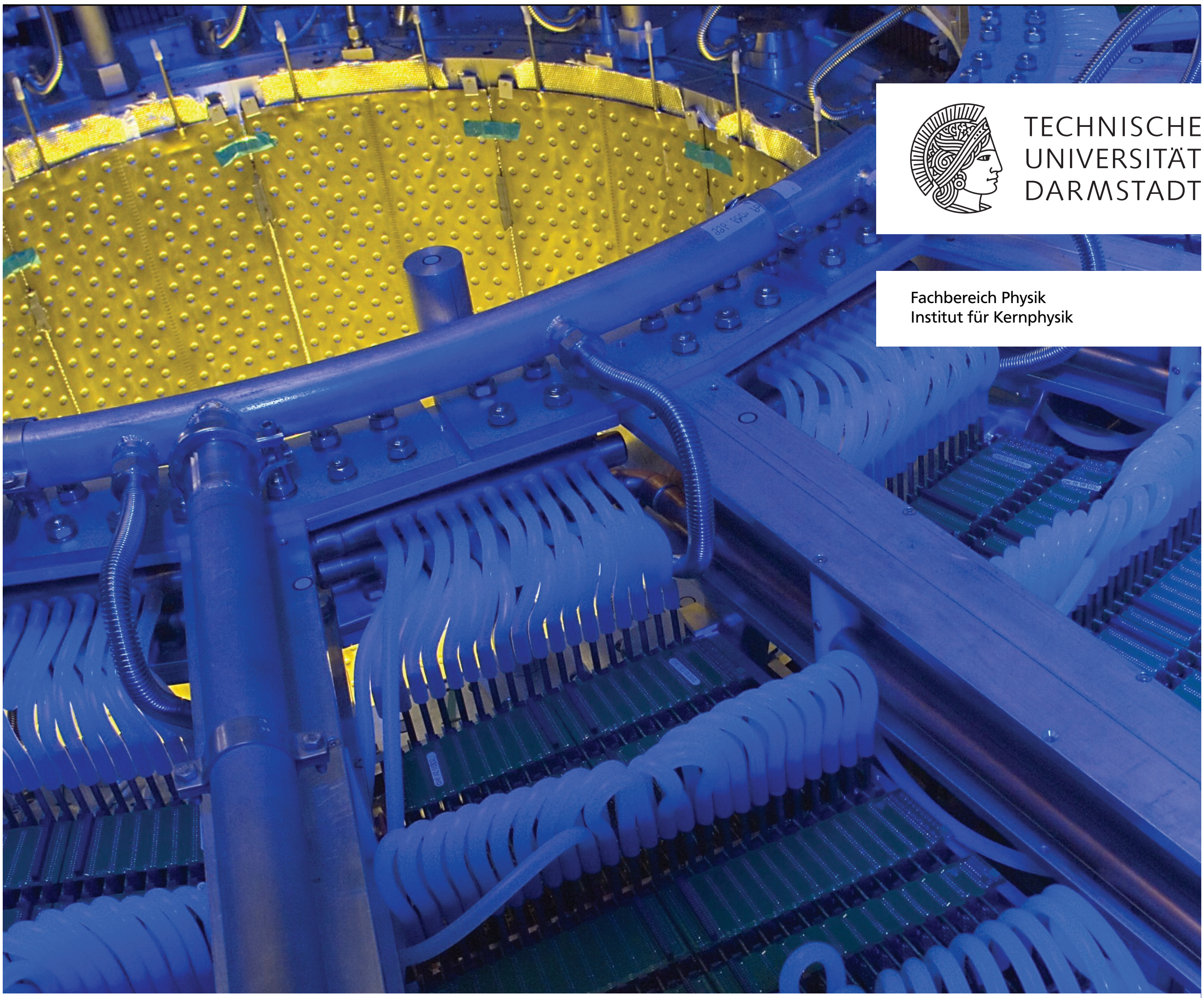

TECHNISCHE
UNIVERSITÄT
DARMSTADT

Fachbereich Physik
Institut für Kernphysik

GSI
Helmholtzzentrum
für Schwerionenforschung GmbH

ALICE

CERN
European Organization
for Nuclear Research

Abstract

The time projection chamber (TPC) is the central tracking detecor of the ALICE experiment at the Large Hadron Collider. The readout chambers that are used are custom-built multiwire proportional chambers. It is essential for the choice of operational parameters and the correct operation to have a detailed understanding of the characteristics of these readout chambers – under normal operating conditions as well as under conditions exceeding the specifications.

In the course of this thesis a test setup for the readout chambers has been constructed and commissioned. Besides the readout chamber, this includes all associated services that are necessary to carry out many sorts of tests as well as software for control, data acquisition and data analysis purposes. This thesis contains a detailed description of the test setup and its components as well as the documentation of the software.

With the test setup the noise behaviour and gas amplification of the readout chamber was studied along with the characterization of the impact of electronics and data analysis methods. The results are presented in this thesis.

Zusammenfassung

Die Zeitprojektionskammer (TPC) ist der zentrale Spurdetektor des ALICE Experiments am Large Hadron Collider. Als Auslesekammern der TPC werden speziell entwickelte Vieldraht-Proportional-Kammern verwendet. Ein genaues Verständnis des Verhaltens dieser Auslesekammern – sowohl unter den betriebsmäßigen Bedingungen – als auch unter davon abweichenden, außergewöhnlichen Bedingungen ist unverzichtbar für die Wahl der Betriebsparameter und die einwandfreie Funktion.

Im Rahmen dieser Arbeit wurde ein Teststand für die Auslesekammern aufgebaut und in Betrieb genommen. Dazu gehören neben der Auslesekammer auch alle für umfangreiche Tests notwendigen Unterstützungssysteme sowie Computerprogramme zur Steuerung, Datenaufnahme und Datenauswertung. Die Arbeit enthält eine ausführliche Darstellung des Testaufbaus und eine Beschreibung der Komponenten sowie die Dokumentation der Software.

Der Teststand wurde benutzt um das Rauschverhalten und die Gasverstärkung der Auslesekammern zu untersuchen, sowie die Einflüsse von Elektronik und Auswertmethoden zu charakterisieren. Die Ergebnisse werden in dieser Arbeit präsentiert.

Contents

1 Introduction

Strongly interacting particles are called *hadrons* which are subdivided into two groups. Bosons, i. e. particles with integer spin quantum number, are called *mesons* whereas the fermions with an half-integer spin are called *baryons*. The protons and neutrons are bound together by the strong interaction to form the nucleus.

Within the framework of the *Standard model of elementary particle physics* strongly interacting matter is described by the the theory of *quantum chromodynamics (QCD)*. The QCD is a quantum field theory made up of *quark* and *gluon* fields. There are six different types of quarks: up, down, strange, charm, bottom and top[1] bound together to the hadrons by the gluons. The eight massless gluons are the gauge bosons that mediate the strong interaction, they couple to the *color charge*. The complication of the theory arises from the fact that not only the quarks carry color charge, but also the gluons. This interaction of the vector fields among each other leads to the concept of the running coupling constant that depends on the momentum scale. For high momentum scales (corresponding to short distances between the quarks) the coupling gets weak explaining the *asymptotic freedom* of quarks. At small momentum scaled (corresponding to large distances between the quarks) the coupling gets strong and explains the *confinement* of quarks.

The terms “asymptotic freedom” and “confinement” describe the two seemingly contradictory observations that quarks are always bound into hadrons and no free quarks are seen (confinement) and that in scattering experiments with large momentum transfer the measured cross-sections match the predictions under the assumption of free quarks.

For small coupling constants predictions from the theory can be approximately calculated as a power series of the coupling constant (pertubation theory), for large coupling constants (when the strong interaction is really strong) the continous theory is formulated on a discrete lattice and solved numerically (“lattice QCD”).

When the temperature or density of nuclear matter is increased it is expected from lattice QCD calculations that the quarks are deconfined and form a new state of matter, the *quark-gluon plasma (QGP)*. Such conditions with high energy densities are believed to have existed in the early phase of the universe, a few microseconds after the big bang. A QGP could also exisist in the core of neutron stars where the density exceeds the density of the nucleus. The properties of the QGP are described by thermodynamical models and lattice QCD.

In the laboratory such extreme conditions can be created in the collisions of heavy nuclei at ultra-relativistic energies. The ALICE experiment is designed to study the properties of the QGP among other collective phenomena of strongly interacting matter. The collision energies of $\sqrt{s_{NN}} = 5.5$ for lead-lead nuclei provided by the LHC will create energy densities of 1-1000 GeV/fm^2 under which the QGP will be produced and the transition from the QGP to a hadron gas will be observed.

In a collision of two lead nuclei a “fireball” with very high temperature and density is produced. This might be the QGP which then expands and cools down do form hadrons in the freeze-out phase. These hadrons or, for particles with a short lifetime, their decay products will form the majority of particles

---

[1] In simplified model normal matter (protons, neutrons) contains only up and down quarks, the others can be produced in particle accelerators or by cosmic rays.

observed in the ALICE detectors and they provide information of the freeze-out phase. In the very early phase of the collision hard scattering can occur where heavy particles or particles with large transverse momenta are produced. Photons and dileptons created at all stages of the collision are not subject to the strong interaction and can leave the medium.

ALICE detects a large fraction of the produced particles, identifies them and measures their momenta. Short-lived particles are reconstructed from their decay products. The effects of the formation of a QGP will be observed in the particle spectra. The spectra for different particles produced at the freeze out can be used to calculate the freeze-out conditions such as temperature, baryon chemical potential, energy density, etc. Signatures of the QGP are especially strangeness enhancement, J/Ψ suppression and jet quenching.

2 The ALICE Experiment

The ALICE[1] Experiment [1, 2] is one of the four big experiments at the CERN LHC and the only one dedicated to the study of heavy-ion collisions. The other three experiments are the general-purpose detectors ATLAS and CMS and the specialized b-physics experiment LHCb which are optimized for proton-proton (p-p) collisions.

The Large Large Hadron Collider (LHC) is a large (27 km circumference) synchrotron with two beam pipes to accelerate nuclei to unpresedented energies, up to 7 TeV for a proton. The ALICE detector is installed in one of the four interaction points (IPs) where the beams cross and the particles are colliding (for protons: center-of-mass energy $\sqrt{s} = 14$ TeV).

The physics programme of ALICE focuses on the study of lead-lead (Pb-Pb) collisions at a center-of-mass energy per nucleon pair of $\sqrt{s_{NN}} = 5.5$ TeV. For many observables measured in ALICE it is important to compare them to p-p or proton-nucleus (p-A) collisions. Therefore runs with p-Pb, lighter ions (such as argon) and lower energies are also intended.

In the Pb-Pb collisions a very large number of particles will be produced, early extrapolations from data measured at lower collision energies lead to charged particle multiplicities of up to 8000 charged particles per rapiditiy unit. These high multiplicities are a challenge for all detectors and in particular for the TPC.

The ALICE detector is located in an underground cavern at Point 2 of the LHC tunnel. It is composed of many subdetectors (c. f. figures 2.1 and 2.2) that are described below. With the exception of the muon arm, the ZDC and ACORDE the detectors are installed inside the 0.5 T solenoid L3[2] magnet.

2.1 Coordinate system

The global coordinate system of ALICE [4, 5] has the origin at the Interaction Point (IP), where the two beams collide. The z-axis is parallel to the mean beam direction with positive z pointing towards the access shaft (this side is also called A-side[3]) and negative z towards the muon arm (called C-side[4]). The x-direction is horizontal and perpendicular to z with positive x pointing inside the LHC (also called I-side) and negative x outside the LHC ring (called O-side). The y-direction is perpendicular to x and z with positive y pointing upwards to the surface.

The corresponding spherical coordinate system is given by the radial distance $r = \sqrt{x^2 + y^2 + z^2}$, azimuthal angle $\varphi = \mathrm{atan2}(y, x)$ and polar angle $\theta = \arccos z/r$. The polar angle can be expressed in terms of the *pseudorapidity* η that in turn can be written in terms of a particles total momentum $p = |\vec{p}|$ and its component along the beam axis p_z:

$$\eta = -\ln\left[\tan\left(\frac{\theta}{2}\right)\right] = \frac{1}{2}\ln\frac{p + p_z}{p - p_z} \tag{2.1}$$

---

[1] A Large Ion Collider Experiment

[2] The magnet was used before by the L3 experiment of the Large Electron-Positron Collider (LEP), hence the name.

[3] The next experiment in this direction is ATLAS at Point 1.

[4] The next experiment in this direction is CMS at Point 5.

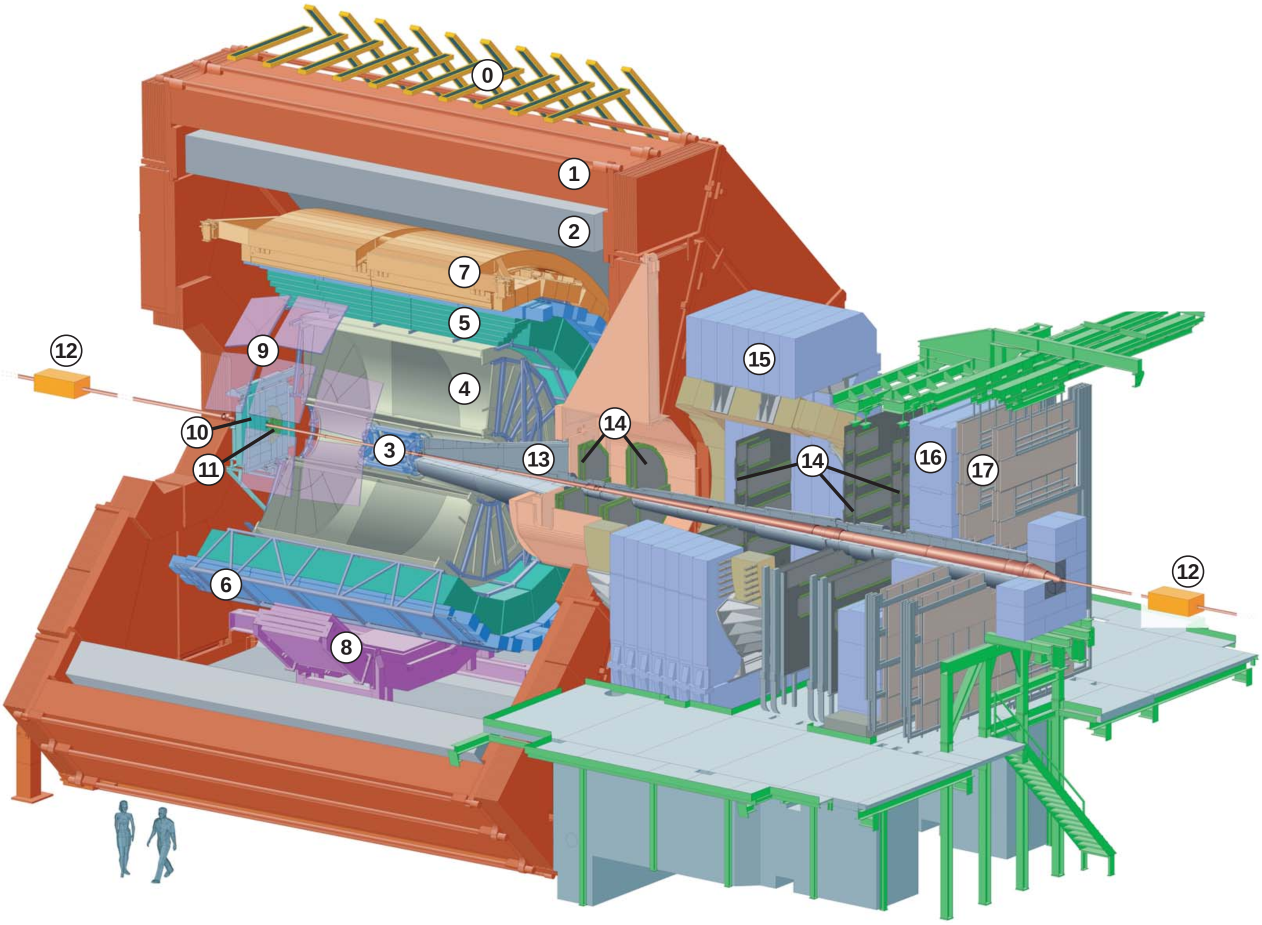

Figure 2.1: The layout of the ALICE detector with its subdetectors: L3 magnet with return yoke (1) and coils (2); ITS surrounding the interaction point (3); TPC (4); TRD (5); TOF (6); EmCAL (7); PHOS (8); HMPID (9); PMD (10) and T0-A (hidden by PMD); FMD-1 and VO-A (11); ZDC (12) 116 m from IP; muon absorber (13); muon tracking chambers (14); muon dipole magnet (15); filter wall (16); muon trigger chambers (17) and ACORDE (18). [3]

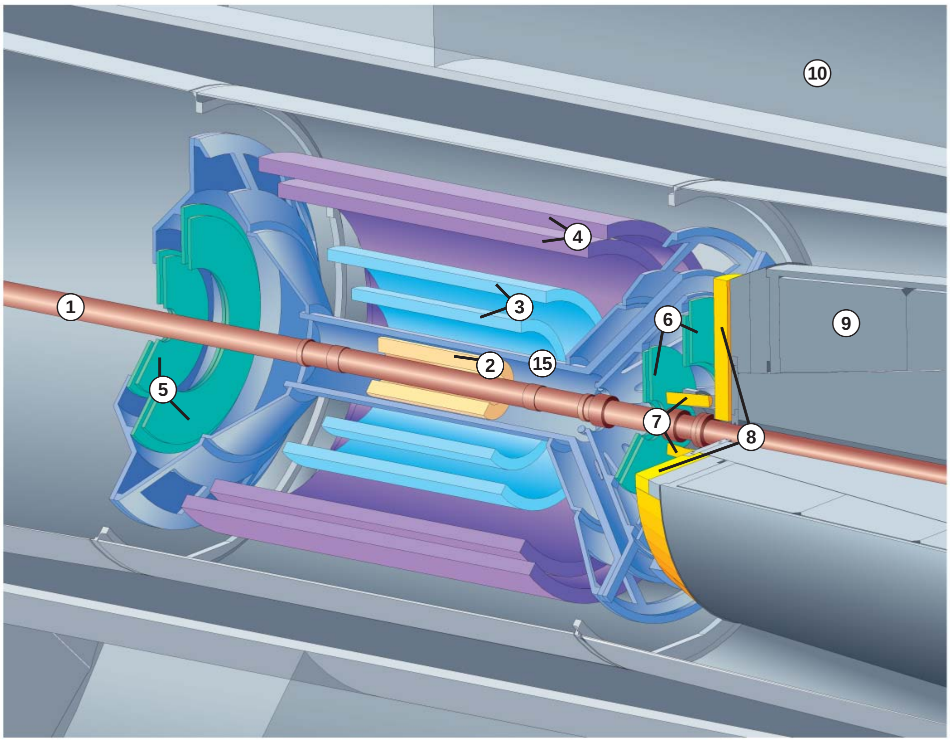

Figure 2.2: The layout of the inner detectors surrounding the beam pipe (1): SPD (2), SDD (3), SSD (4), FMD-2 (5) and FMD-3 (6), TO-C (7), V0-C (8). The muon absorber (9) and the TPC (10) are also visible. [3]

The pseudorapidity is an approach to the rapidity of special relativity in the limit $E \to p$. The positive x-axis along the beam corresponds to $\eta = \infty$ while $\eta = 0$ is perpendicular to the beam.

For the description of the sub-detectors azimuth and pseudorapidity are used to characterize the acceptance; r is used in the meaning of distance from the beam axis, i. e. $r = \sqrt{x^2 + y^2}$.

2.2 Inner Tracking System

The Inner Tracking System (ITS) [6] is used to determine the position of the primary interaction vertex and secondary vertices from weak decays, which are important for the reconstruction of quickly decaying particles. Particles at low momenta (below 100 MeV) are only visible to the ITS and tracking and particle identification of these low energy particles is done with the ITS. The information from the ITS is also used together with the data from the TPC to improve momentum and dE/dx measurements. The innermost layers (SPD) overlap with the FMD in order to allow the measurement of the charged particle multiplicity in a large pseudorapidity range.

The ITS uses semiconductor detectors made of silicon and consists of six layers. The innermost two layer make up the Silicon Pixel Detector (SPD) which is located as close as possible to the beam pipe ($r = 3.9$ cm and $r = 7.6$ cm). The two intermediate layers are the Silicon Drift Detector (SDD) and the two outermost layers are the Silicon Strip Detector (SSD). The outer four layers (located at $r = 15$, 24, 38 and 43 cm) cover the pseudorapidity range $-0.9 < \eta < 0.9$ and have analog readout for $\mathrm{d}E/\mathrm{d}x$ measurements. The SPD which has almost 10 million pixels is read out digital. Overlapping of the active detector elements within one layer ensures full acceptance.

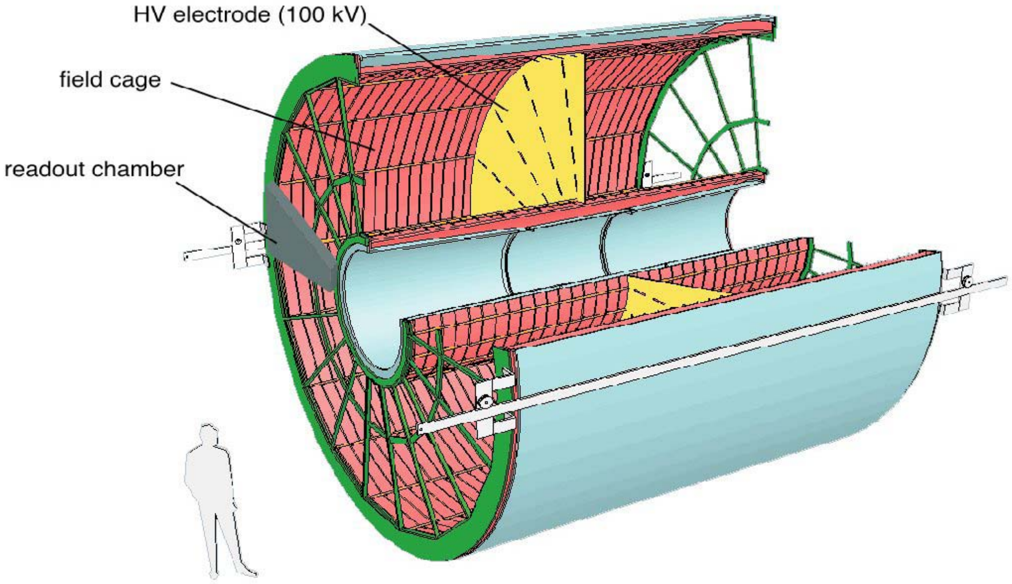

Figure 2.3: The ALICE TPC. [7]

2.3 Time Projection Chamber

The Time Projection Chamber (TPC) is the main tracking device of the ALICE experiment. Its objective is to measure the three dimensional trajectories of charged particles along with the specific energy loss $\mathrm{d}E/\mathrm{d}x$ to provide particle identification. It is the largest TPC ever build and designed to cope with the high particle multiplicities expected for Pb-Pb collisions. It covers 2π in azimuth (with small dead zones between the chambers) and the pseudorapidity range $-0.9 < \eta < 0.9$ for tracks with the full radial length matching the acceptance of the other central barrel detectors (ITS, TRD and TOF).

The TPC has the shape of a hollow cylinder with 0.57 m inner radius, 2.78 m outer radius and a length of 5.1 m. Inside the inner radius the ITS is located and on the outside the TPC is followed by the TRD. Figure 2.3 shows the layout of the TPC.

In between the inner and outer containment vessels it contains a 90 m^3 active volume filled with a gas mixture of Neon, Carbon dioxide and Nitrogen in the ratio 90-10-5 and a high voltage drift electrode in the center. The drift electrode produces the drift field, it is held at a voltage of 100 kV and divides gas volume into two drift regions with a length of 250 cm each. This results in a drift field of 400 V/cm. To produce a highly uniform electric field in the drift region aluminized Mylar strips surrounding the drift volume are connected to potential degrader network fed by the drift voltage. Each of the two endplates is instrumented with 36 readout chambers arranged in 18 sectors. Each sector contains an Inner Readout Chamber (IROC) and an Outer Readout Chamber (OROC).[5].

Charged particles crossing the chamber ionize the atoms/molecules of the gas, the created electrons drift along the electric field. The magnetic field is oriented parallel to the electric field, thus the drifting electrons are not influenced by it. At the end of their drift path the electrons are amplified by an avalanche process around the anode wires. The cathode is segmented into pads that are read out by the front end electronics (details in section 3.5).

---

[5] The readout chambers are described to more detail in section 3.4

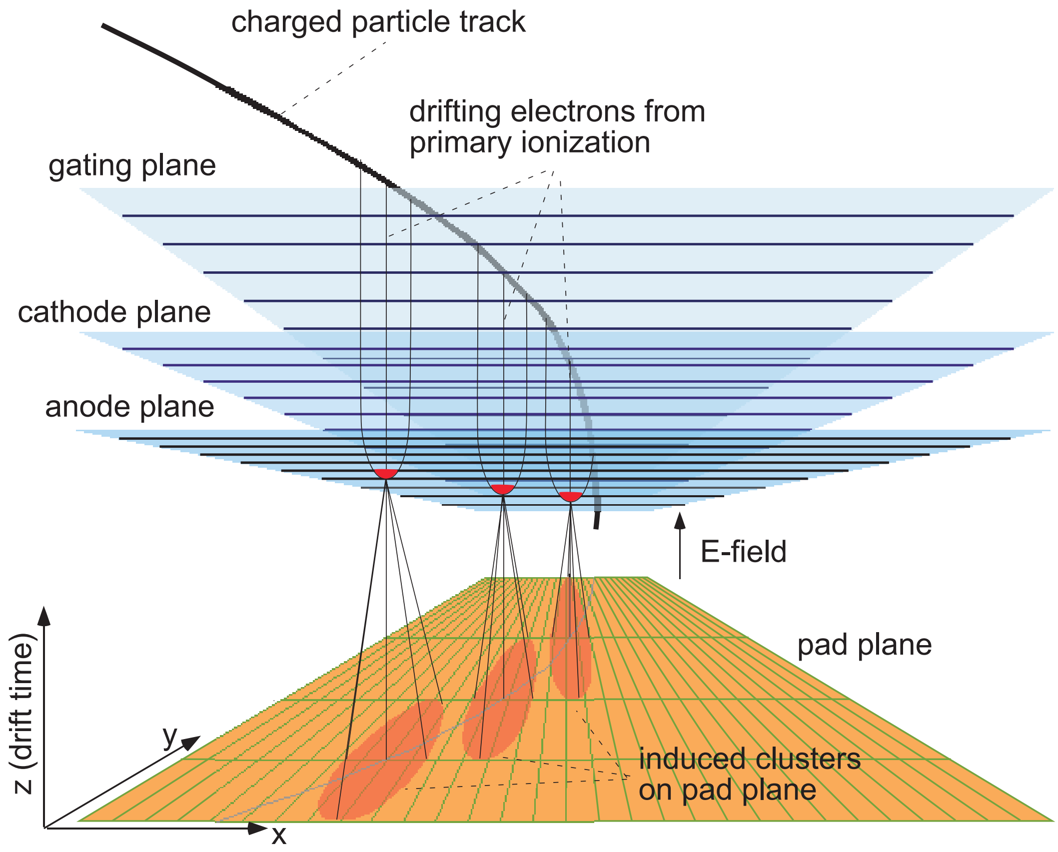

Figure 2.4: Illustration of the principle of a time projection chamber.[7]

The segmentation of the two readout planes (into 278784 pads each) gives the coordinates in the r and φ direction (the plane perpendicular to z), the time of arrival is also recorded so – with the known drift velocity – the z component can be calculated. It is apparent that this only works if the time at which the particle entered the chamber (and created the drift electrons) is known. Thus a trigger is mandatory for the operation of the TPC.

The gas mixture chosen for the TPC is a mixture of Ne (85.7%), Carbon dioxide (CO_2) (9.5%) and Nitrogen (N_2) (4.8%) optimized for low diffusion and high drift velocity. However its properties (especially the electron drift velocity and the Townsend coefficient) depends strongly on the exact gas composition, the pressure and the temperature. A drift velocity monitor is installed to measure changes of the gas properties, the stability of the temperature is achieved with the cooling system.

The cooling system of the TPC serves two purposes: removal of the heat generated by the front end electronics ($\approx$ 30 kW) and to provide a high temperature stability and homogeneity ($\Delta T < 0.1$ °C) within the active volume of the TPC. The Front-End Cards (FECs) are wrapped in copper plates equipped with cooling pipes to remove the heat. To further remove the heat transfered to the chambers the Readout Chamber (ROC) aluminum bodys have embedded cooling loops. The surface of the TPC towards the ITS (except for the central region around the IP) and the TRD is equipped with water-cooled heat screens, the ROCs are also covered with heat screen panels. The cooling plant employes the principle of a leakless underpressure cooling circuit. The high voltage degrader network is supplied by its own cooling unit and cooled with high-resistivity water.

For calibration and alignment of the TPC uses a laser calibration system is used in addition to cosmic tracks. The laser produces straight tracks perpendicular to the beam axis that are crossing the chamber boundaries (alignment) for the drift velocity studies the electrons emitted at the central electrode by scattered light are useful. For the gain calibration radioactive krypton gas can be added to the gas mixture.

2.4 Transition Radiation Detector

The primary aim of the Transition Radiation Detector (TRD) [8] is to provide electron/pion separation for momenta above 1 GeV.

Charged particles passing the boundary of two polarizeable media with different refractive indices emit photons called transition radiation. The intensity depends on the Lorentz factor γ, so for a fixed momentum electrons emit far more transition radiation compared to other particles. This makes the transition radiation detector an excellent tool for electron identification.

The TRD consists of 540 chambers arranged in 18 super modules (following the segmentation of the TPC) with six chambers stacked in radial direction and covers the full azimuth with $-0.84 < \eta < 0.84$. Each chamber consists of a radiator, a drift chamber and the readout electronics. The radiator contains polypropylene fibre mats, this ensures the large number of transitions that is essential to generate a detectable amount of radiation. This radiation has energies in the X-ray range thus the drift chamber is filled with a high-Z gas to ensure a large conversion rate. In addition to the transition radiation all charged particles ionize the counting gas thus the TRD is also contributing to the tracking and dE/dx measurements.

2.5 Time of Flight Detector

The Time-Of-Flight Detector (TOF) [9] measures the velocity of charged particles (by the time it takes to travel from the IP to the TOF) allowing Particle Identification (PID) in the momentum range above the coverage from $\mathrm{d}E/\mathrm{d}x$ by TPC+ITS. The start signal is delivered by the T0 detector.

The TOF was designed as a Multi-gap Resistive Plate Chamber (MRPC) which features fast signals and a very good time resolution (better than 40 ps for the TOF).

The TOF is surrounding the TRD and follows the segmentation of the TPC and TRD (18 supermodules covering the full azimuth) with a pseudorapidity coverage of $-0.9 < \eta < 0.9$ that matches the acceptance of the TPC for full radial track length.

2.6 High Momentum Particle Identification Detector

The High High Momemtum Particle Identification Detector (HMPID) [10] is designed for the detection of hadrons with high transverse momenta $p_t >$ GeV and to discriminate between kaons, pions and protons. The high p_t hadrons are produced by hard processes and their spectra provide information on qet quenching.

In the HMPID charged particles travelling through the liquid perfluorohexane (C_6F_{14}; n=1.2989) radiator with a velocity $\beta > 1/n$ produce Cherenkov radiation in a cone with the Cherenkov angle $\cos\theta_C = 1/(\beta n)$. This cone is projected to Caesium Iodide (CsI) photocathode resulting in a ring[6] of released electrons that are amplified and detected in a CH_4 filled Multi-Wire Proportional Chamber (MWPC) with

---

[6] Thus those detectors are called Ring Imaging Cherenkov (RICH) detectors

pad readout. Via the opening angle θ_C the velocity of the particle is measured; with its momentum determined by TPC+ITS it can be identified.

The HMPID constists of seven modules with three radiator modules each. It covers the pseudorapidity range $-0.6 < \eta < 0.6$ in the azimuthal range $1.2° < \phi < 58.8°$.

2.7 Photon Spectrometer

With the Photon Spectrometer (PHOS) [11, 12, 13] it is possible to measure the energy of photons with high energetic and spatial resolution in the range from 100 MeV to 100 GeV. Photons are coming from different sources: mainly the $\gamma\gamma$ decay of neutral mesons (π^0, η), thermal photons from the medium, and diphotons from $q\bar{q} \rightarrow \gamma\gamma$.

The PHOS is a homogenous calorimeter with high-density PWO (Lead-tungstate, $PbWO_4$) crystals as scintillators (approximately 20 radiation length thickness) and large area avalanche photo diodes for readout[7]. It has a high granularity and is segmented into 17920 crystals arranged in five modules. Placed at the bottom of the L3 magnet and are oriented towards the IP it covers the pseudorapidity range $-0.12 < \eta < 0.12$ and azimuthal range of $\Delta\phi = 100°$. To discriminate between charged particles and photons every module has a segmented MWPC on top which acts as a charged particles veto counter.

2.8 Electromagnetic Calorimeter

The Electromagnetic Calorimeter (EmCAL) [14, 15] was added to the ALICE setup as an upgrade to enhance the capabilities of jet measurements and high p_t photon and electron identification. It also provides an efficient trigger for hard jets, photons and electrons.

It is placed between the TOF and the L3 magnet in the space available between PHOS and HMPID. It provides coverage in the pseudorapidity region $-0.7 < \eta < 0.7$ with the azimuthal acceptance of $\Delta\phi = 107°$ and partial back-to-back coverage with PHOS.

The EmCAL is a sampling calorimeter made of alternating layers of plastic scintillator (active component: 77 layers) and lead (passive component: 76 layers) with a thickness of 20 radiation lengths. Wavelength shifting fibres are embedded in radial direction into the tower and guide the light to an avalanche photo diode for detection (one tower: 4 towers make up one module). The 3072 identical modules are oriented to face the IP and arranged in 12 super modules following the sector structure of the other central barrel detectors.

2.9 Muon Spectrometer

The Muon Spectrometer [16, 17, 18] is designed to detect the dimuon decays of the mesons $J/\Psi, \Psi', \Upsilon, \Upsilon'$ and Υ'' as well as muons from open charm and bottom decays. The heavy flavour mesons $c\bar{c}$ and $b\bar{b}$ are sensitive probes of the formation of a Quark-Gluon Plasma (QGP) since they are expected to “melt” when traversing the deconfined medium.

---

[7] It also uses the ALTRO chip and RCU developed for the TPC.

The identification of muons at low p_t is not possible in the central barrel due to huge pion background. Thus the muon spectrometer is designed as a forward spectrometer with an acceptance covering a pseudorapitidy range of $-4.0 < \eta < -2.5$ where the muons have higher (total) momentum (Lorentz boost). An absorber made of concrete and carbon (front absorber) stops most of the hadrons and photons while high-energy muons, which have lower energy loss, can pass it. The muons are deflected in a large dipole magnet (field integral: 3 Tm) and detected in five tracking stations (two in front of the magnet, one inside the magnet and two after the magnet). Each station consists of two layers of a thin gas detector with high-granularity readout resulting in more than 10^6 channels.

The tracking chambers are followed by a second absorber (muon filter wall) and the four trigger chambers (arranged in two stations), which are used to trigger on dimuons. Since beam-gas interactions are source of a large background in the muon trigger the V0 detector is employed as a fast interaction trigger.

2.10 Zero Degree Calorimeter

Depending on the impact parameter a different number of nucleons is participating in the nuclear collisions, the Zero Degree Calorimeter (ZDC) [19, 20] measures the energy taken away by the non-interacting spectator nucleons. This is a direct measure for the centrality of the collision and is used as a Level-1 trigger (L1) in ALICE.

The spectator nucleons leave the interaction point along the beam axis, they are separated from the beam by the LHC magnets (which also separate the two beams). The hadronic detectors of the ZDC are located 116 m away from the IP where the beams are separated from the spectator nucleons and the neutrons and protons are separated as well[8]. The hadronic ZDC consists of the neutron detector (ZN) and the proton detector (ZP) which detect the Cherenkov light produced by the showers of charged particles.

On the A-Side (7.5 m from IP) two electromagnetic calorimeters (ZDC Electromagnetic detector (ZEM)) complete the setup and help to determine the centrality for very peripheral events where nuclear fragments are produced that cannot be detected[9] by the ZN/ZP.

2.11 Photon Multiplicity Detector

The Photon Multiplicity Detector (PMD) [21, 22] measures the distribution of photons in the pseudorapidity range of $2.3 < \eta < 3.5$ (full azimuthal coverage). Besides the photon multiplicity the PMD also gives an estimate of the reaction plane and the transverse electromagnetic energy.

The detector has a fine granularity (182 000 readout channels with a cell cross-section 0.22 cm^2) to provide a low occupancy and high efficiency within the high particle flux environment. It is located on the A-side, approximately 3.6 m from the IP and consists of two proportial gas counters with a honeycomb cell structure and a lead converter in-between. The first (from the IP) detector plane is used as a charged particle veto counter, in the converter photons induce electromagnetic showers that are detected by the preshower counter. The showers initiated by photons produce large signals in many cells while hadrons normally hit only one cell which allows to distinguish them.

---

[8] Protons are deflected stronger while neutrons are unaffected by the magnets.

[9] Q/m similiar to lead.

2.12 Forward Multiplicity Detector

Charged particles at high pseudorapidities ($-3.4 < \eta < -1.7$ and $1.7 < 5.0$) are detected in the Forward Multiplicity Detector (FMD) [23] which provides informations on multiplicity fluctuations and determiniation of the reaction plane. Together with the ITS pixel detector the charged-particle multiplicity coverage extends to $-3.4 < \eta < 5.0$ with overlaps between FMD and SPD.

The FMD consists of five rings (three inner rings and two outer rings) arranged in three systems surronding the beam pipe. On both sides of the IP (at a distance of approximately 0.7 m) the FMD-2 and FMD-3 stations cover about the same pseudorapidity range; on the A-side the FMD-3 (3.2 m from IP) extends the coverage to higher pseudorapidities (on the C-side there is the muon absorber). Each of the five FMD rings is made of 10 200 (single-layer) silicon strip detectors that use the ALTRO chip and RCU for readout.

2.13 V0 and T0 forward detectors

The Vertex-0 detector (V0) and Time-0 detector (T0) detectors [23] measure charged particles in the very forward regions to provider trigger and timing information.

The V0 detector provides a trigger for the central barrel detectors and muon spectrometer. The measured coincident signals and the total collected charge provide a fast (on-line) information on the multiplicity and centrality of the collision. In addition the V0 will measure the luminosity in p-p collisions. The timing information from the two counters is used to distinguish between beam-beam and beam-gas interactions.

It consists of two disk-shaped arrays of plastic scintillators on either side of the IP (V0-A at 340 cm and V0-C at 90 cm distance). The scintillators are connected to photomultiplier tubes (PMTs)[10] via wavelength shifting fibres. The covered pseudorapidity ranges are $2.8 < \eta < 5.1$ (V0-A) and $-3.7 < \eta < -1.7$ (V0-C) and partially overlap with the FMD.

The two T0 detectors are placed close to the V0 covering a smaller pseudorapidity range of $4.5 < \eta < 5.0$ (T0-A) and $-2.9 < \eta < -3.3$ (T0-C). They provide very fast and accurate timing signals of the collision (50 ps RMS time resolution) that are used as Level-0 trigger (L0), as a start time for the TOF detector and as wake-up pretrigger of the TRD. The timing difference from the two detectors allows to approximately locate the position of the vertex. Redudant to the V0, the T0 provides rough estimates on multiplicity and provides minium bias and multiplicity triggers.

The T0 detectors constists of 12 Cherenkov counters each with quartz radiators and PMTs.

2.14 ACORDE

The ALICE Cosmic Ray Detector (ACORDE) [24] is a trigger-detector and provides a fast L0 on cosmic rays. It consists of 120 plastic scintillators with PMTs arranged in 60 modules of two stacked scintillators and distributed over the three upper faces of the L3 magnet yoke. The coinicdent signal from two overlapping signals a single muon event, the coincidence of many modules is used to trigger on multimuon events (muon-bundles).

---

[10] It is noticeable that they are operating inside the L3 magnetic field.

The ACORDE trigger is used for calibration and alignment purposes and will be used – during normal data taking – to study cosmic rays with primary energies of 10^{15} to 10^{17} eV corresponding to muons with 20 GeV to 2 TeV using the TPC, TRD and TOF.

3 The Experimental Setup

The test setup is installed in a laboratory at the CERN main site in Meyrin, Geneva. The objective of this test setup is to study the characteristics of the readout chambers in the lab – especially fully equipped readout chambers including the full electronics readout chain and all services. Besides investigating the noise and pedestal behaviour the present configuration of the setup can be used for gain measurements (with an ^{55}Fe source), energy-loss studies (by utilizing cosmic rays) and general electronics and readout tests. With the intended completion of the laser optics and the adequate safety protection equipment studies of drift velocity properties will become possible.

Generally the setup follows the design of the ALICE TPC as far as possible, similaritys as well as differences will be pointed out; the test setup in the lab is refered to as *test setup*, the ALICE TPC as *TPC*.

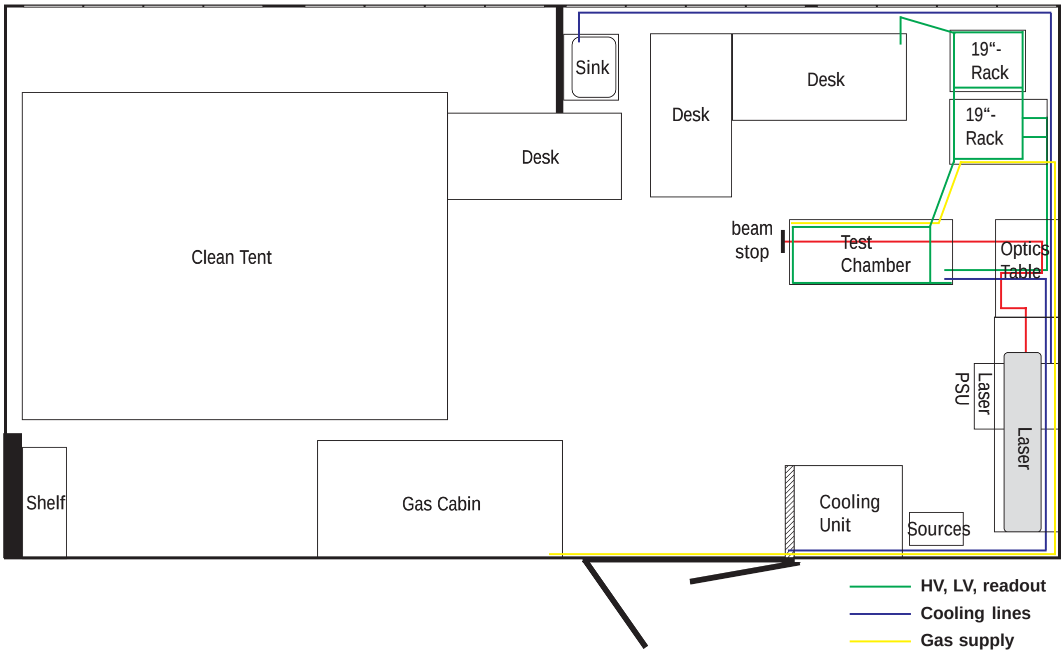

Figure 3.1: Schematic arrangement of the laboratory including the proposed laser layout.

3.1 The general layout

One OROC (No. 10)[1] is mounted in a test box containing a small field cage with 11 cm drift length. The chamber is operated with the TPC gas mixture at atmospheric pressure. The gas supply uses premixed gas with an adjustable flow up to 40 l/h, temperature, oxygene content and absolute pressure are measured at the gas exhaust of the test box.

---

[1] This chamber was showing instabilities during previous irradiation tests and was therefore excluded from installation to the TPC.[25]

Figure 3.2: Layout of the test setup installation in “LaTotal”: Test box (1) containing the field cage and readout chamber; support frame with front end electronics (2); high voltage power supplies (3) for field cage, chamber and photomultiplier; NIM electronics (4) used as trigger and calibration pulser; scintillators for cosmic triggering (5); low voltage power supply for electronics (6); gating pulser (7); systems for slow control (8) i. e. temperature, pressure, cathode current, oxygen content, cooling water flow; cooling unit and instrumentation (9), laser head (10) with power supply unit (11) and interlock (12); radioactive source with adjustable support (13); computers (14) for data acquisition, slow control and front end electronics. The gas supply station is not visible.

A support frame is attached to the test box and completely[2] equipped with the full readout electronics arranged in four readout partitions. Every partition is connected via an optical fibre (DDL) to a computer where the data is written to disc. The readout is performed using the ALICE Data Acquisition and Test Environment (DATE) software system which provides a GUI to control the data taking. A slow control system based on LabView programs running on a Windows machine provides monitoring of operational parameters. The services such as cooling unit, power supplies for operating the field cage, chamber and electronics complete the setup. Radioactive sources and cosmic rays can be used to generate charge in the sensitive volume. The laser is in place but not yet operational.

Figures 3.1 and 3.2 give an impression of the general layout of the laboratory, figure 3.3 provides a detailed view of the electronics and connections to the readout chamber.

---

[2] This is not quite true, currently one Front End Card (out of 78) is missing.

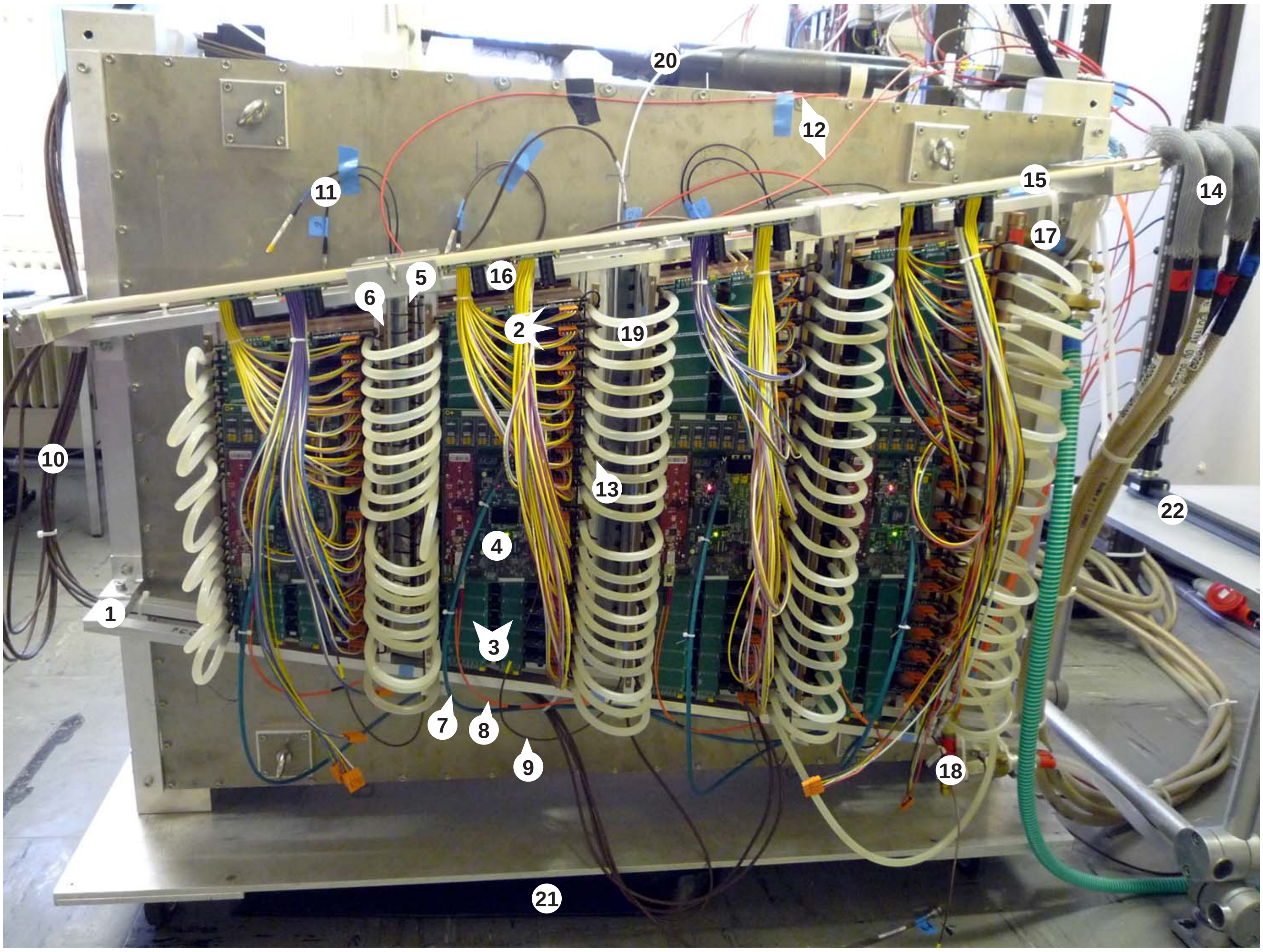

Figure 3.3: The test detector: FEE support frame (1) with front end cards (2) wrapped in cooling plates and backplane (3) connection to RCU (4) equipped with DDL-SIU and DCS board; analog grounding bar (5) attached to chamber body; digital grounding bar (6) attached to support frame; ethernet connection (7) to DCS board; DDl optical readout fibre (8); lemo trigger cable (9); BNC cables (10) to gating grid, cathode wires, edge wires and cover strip; patch cables (11) with capacitive connection to sense wires; high voltage lemo cables (12) for anode voltages; temperature sensor (13) mounted to chamber body; low voltage power supply cables (14) and connection to the bus bar (15) distributing the power to patch cables (16) with buffer capacitors connected to the FEE; cooling supply (17) and return (18) lines with distribution manifold; interconnections of the FEC cooling with silicon hoses (19); scintillators with photomultipliers (20, 21); (20); table (22) to be used for the foreseen laser installation. Gas supply connections, oxygene and pressure sensor are on the righthand side of the chamber but not visible in the picture.

3.2 Test box and field cage

The test box utilized for the present setup has already been used to test the OROCs after production and prior to installation in the TPC. It is made of 1 cm thick aluminum panels and has brick-shaped layout with outer dimensions 1298 × 1028 × 249.5 mm^3.

For the installation of the readout chamber the top plate can be removed and the readout chamber is screwed to the top plate; sealing of the interface is done with an O-Ring and a small amount of Apiezon vaccuum grease to ensure a gas-tight connection. In the same fashion the top plate is connected to the test box. These tasks are performed in a clean tent installed in the lab to provide a low-dust environment since dirt on the wires can lead to discharges. For the same reason chamber and test box have to be carefully cleaned with a CO_2 gas jet prior to installation.

The box contains a field cage with a drift length of 112.5 mm (measured from the High Voltage (HV) plane to the cathode wire plane) which consists of a HV electrode made of 4 mm thick aluminum and eight field defining strips (aluminum) held in position by 12 support rods. The high voltage electrode has 69 holes that are covered with thin (25 μm thick) aluminzied Mylar foil permeably for X-rays (see below). The field strips are 10 mm wide, the gap between two adjacent strips is 5 mm resulting in a pitch of 15 mm between the centers of adjacent strips. The field strips are connected to a voltage degrader network with a 1 MΩ resistor between adjacent strips an 500 kΩ resistor between the drift electrode and the first strip (distance drift electrode – center of first strip: 7.5 mm). The last strip is held at ground potential and its center is aligned to the position of the cathode wire plane.

The general layout of the field cage and the surrounding box is shown in figure 3.4 and a picture of open the box is seen in figure 3.6(a).

In order to carry out measurements with radioactive sources the back side of the box has 69 holes distributed over the sensitive area of the OROC (see figure 3.5), allowing to measure local variations of the gain. The holes are aligned with the holen in the drift electrode. Thin aluminized Mylar foil is covering the holes and acts as a gas barrier while at the same time allowing the passage of X-rays to the detectors sensitive volume. With an adjustable support the source can be precisely positioned.

Two opposing windows at the short sides made of UV transparend quartz allow traversing the chamber with one or more laser beams. The position of the beam is restriced to be between the two strips neighbouring the drift electrode. A third window is located at the long side.

For the connection of the box to the gas system inlet and outlet are providing stainless steel Swagelok connectors. Eletrical connections are made with BNC (gating, cathode, edge, cover), SHV (drift) and HV Lemo (Anode) connectors.

3.2.1 Drift voltage supply

The drift voltage is delivered by a Fluke 415B HV Power Supply (PS), with a maximal output voltage of 3.1 kV. A combined voltmeter/amperemeter build at GSI (F478 Detektor-Ampere-Meter-B) is connected in-between power supply and drift electrode to monitor drift voltage and current through the resistor chain. Power supply and amperemeter have manual operation/readout and are used for visual supervision.

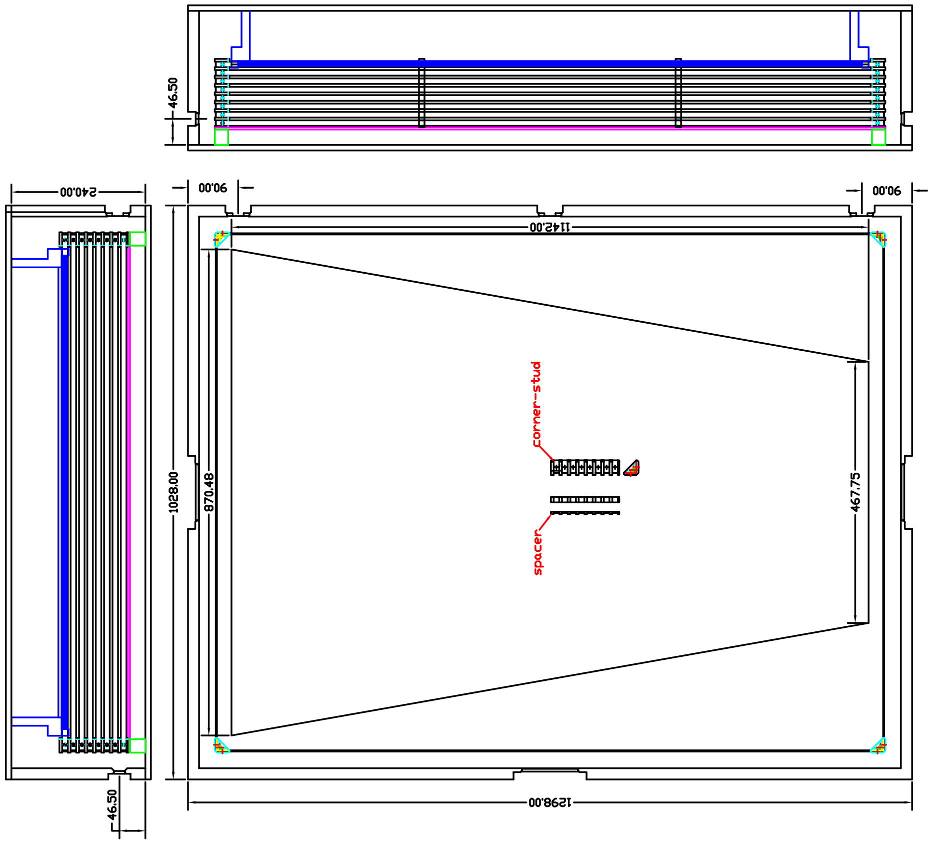

Figure 3.4: The test box with the field cage [26]. The position of the readout chamber is shown in blue, the drift electrode is drawn in pink. The windows for the laser are also visible.

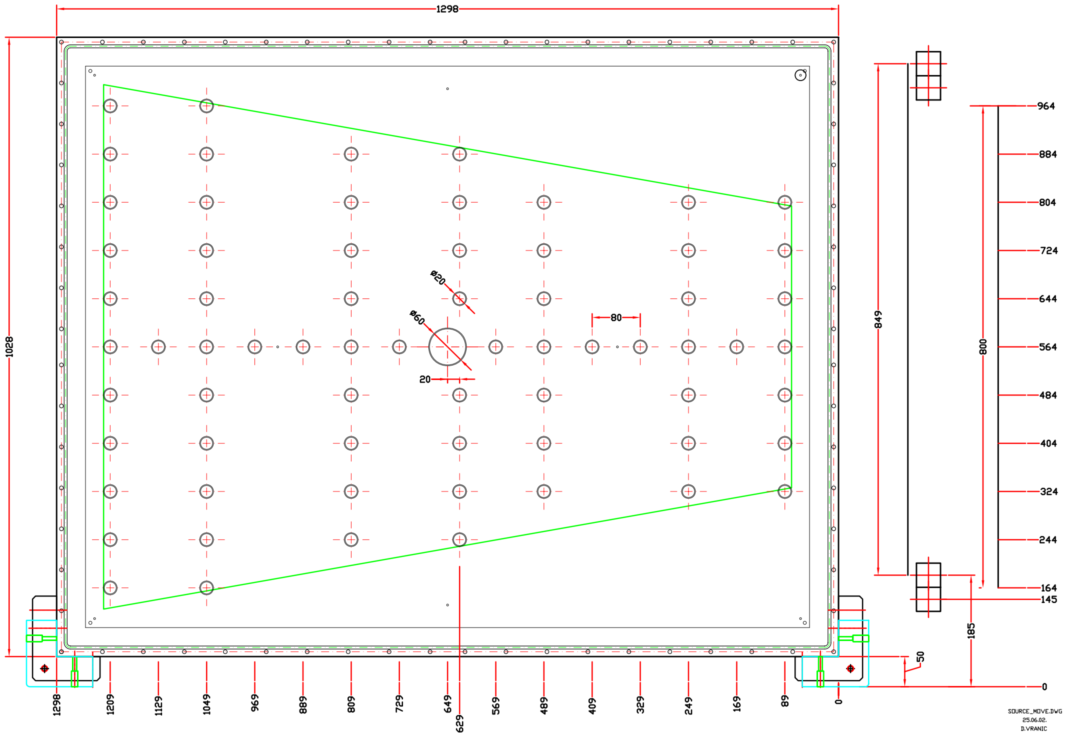

Figure 3.5: Back side of the test box [26] with holes for the source and the position of the OROC.

A drift voltage of 3 kV has been employed for the data taking, corresponding to a drift field of 267 V/cm. This leads to a power dissipation of 1.2 W in the 7.5 MΩ resistor chain. The field is lower compared to the TPC with a drift field of 400 V/cm, but can easily be increased by replacing the power supply.

3.2.2 Support frame

The Front-End Electronics (FEE) are held in place by an aluminum support frame that in turn is mounted on the test box. It is attached at four points located at the corners of the box resulting in a low thermal coupling between the electronics (support frame) and detector. Copper bars screwed to the support frame are used for grounding of the digital side of the FECs.

The support frame (shown in figure 3.6(b)) is furthermore used to retain the cooling distribution manifolds, the Low Voltage (LV) bus bar which delivers the electrical power to the FEE and various readout and supply cables.

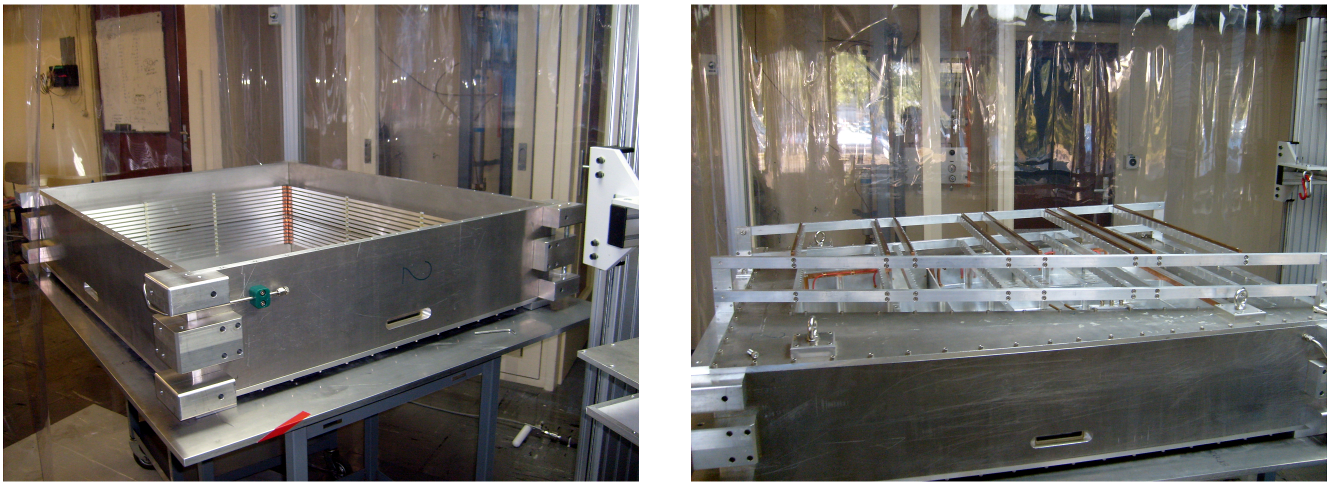

(a) Top plate removed: drift electrode and field strips are visible. On the outside one gas connection and one laser window are seen.

(b) OROC installed and support frame to hold the FECs mounted.

Figure 3.6: The test box with field cage.

3.3 Gas system

The chamber is operated with a mixture of Ne, CO_2 and N_2 with 90-10-5 ratio, the same mixture used in the TPC. The gas mixture that was initially choosen for the TPC was neon and CO_2, the neon predominance is attributed to the high particle multiplicities[27]. Nitrogen was added to improve the stability at high gains and reduce the sensitivity to the unavoidable nitrogen contamination[28].

The test chamber is held at atmospheric pressure; the relatively low gas flow of typically 5 to 10 l/h does not result in a noticeable increase of pressure. This low gas flow rate allows the use of an open gas sytem without circulation even in the present case of high-cost-gas mixture. The pre-mixed gas that was used, had a composition of 4.82% N_2 (purity[3] 5.0), 9.51 % CO_2 (purity 4.8) and 85.67% Ne (purity 4.0).

---

[3] The fist digit of abbreviated purity is the number of leading 9s and the last digit gives the following digit, i. e. 4.8 translates as 99.998%.

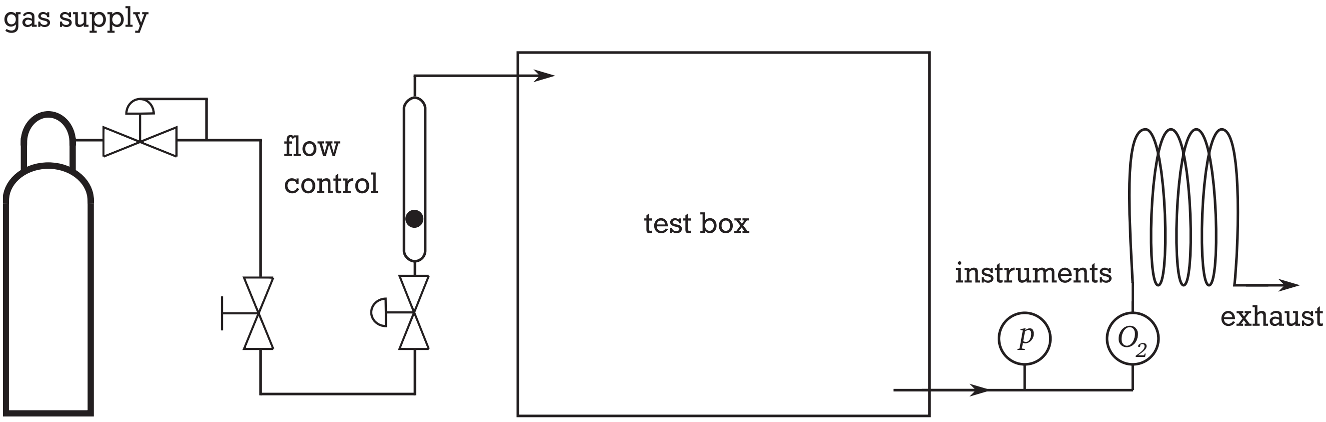

Figure 3.7: Schematic layout of the gas system.

An overview of the gas system is shown in figure 3.7. The flow is measured with a rotameter (range 0-40 l/h) and controlled with a needle valve prior to the detector volume. The gas outlet if followed by an absolute pressure transmitter and an orbishpere oxygen meter (also containing a temperature sensor) allowing to monitor pressure, temperature[4] and oxygen content of the gas. A pit-tail before the exhaust prevents air from diffusing into the oxygen sensor and chamber volume.

The oxygen sensor (Orbisphere model 3600) allows to determine the oxygen content of the gas down to a few parts-per-million (ppm) with high accuracy. It has been calibrated in air prior to installation. Via an RS-232 interface the sensor is connected to the slow control computer and read out with a `LabVIEW`[5] program that allows visual inspection of temperature and O_2 content as well as data recording to disc.

The absolute pressure transmitter (JUMO model 4364-242/91) delivers a 4-20 mA current output corresponding to the absolute pressure from 0-1.6 bar that is digitized with an ADC and read out with a `LabVIEW` program as well.

Interconnections in the gas system are made with Swagelok tube fittings, for short connecting pieces stainless steel and copper tubes are used, the link between gas supply and test box is made of a polyamide hose.

Prior to operation the box if filled and purged with a higher gas flow (40 l/h) for about ten volume exchanges; with the box volume of roughly 240 l this corresponds to 60 hours of flushing. During operation the gas flow is adjusted corresponding to the acceptable oxygen contamination defined by the leak conductance and gas flow.

Oxygen in the chamber causes electron attachment by formation of negative ions. This loss of electrons occurs in the avalanche process resulting in a lower gain and in the drift region resulting in a signal loss corresponding to the drift length. Therefore it is generally desired to achieve an oxygen level as low as possible. For the test setup with its drift length beeing about 25 times shorter than in the TPC it seems reasonable to accept an 25 times higher oxygen content (≈ 25 ppm).

With the assumption that the gas flowing into the box mixed completely with the gas inside before escape the oxygen content decreases exponentially:

$$\alpha(t) = \alpha_Q + \left(\alpha(t_0) - \alpha_Q\right) \cdot \exp\left(-\frac{Q}{V}\,(t - t_0)\right)$$

---

[4] More precisely the temperature of the oxygen sensor; the gas quickly acquires the temperature of the surrounding material.

[5] LabVIEW is a graphical programming environment developed by National Instruments.

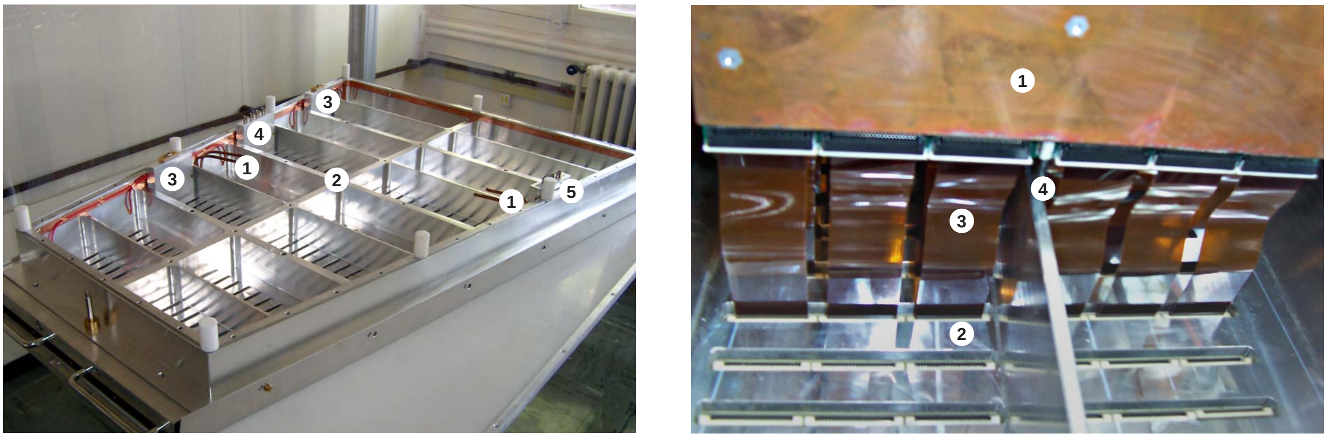

(a) Backside view of the OROC: with cooling lines (1) connection boxes for anode (3), gating (4) and cathode/edge/cover (5) and the position of the temperatur sensor (2).

(b) Detailed view of the connection between FEC (1) and readout chamber (2) via Kapton cables (3). The analog grounding cable (4) is also seen.

Figure 3.8: Pictures of the OROC before installation and connection to the FECs.

Here $\alpha(t)$ is the oxygen content and V is the volume of the box. The limit is given by the oxygen content α_Q of the gas inflow. The flow Q and oxygen content α_Q consists of two compontents: fresh gas flow F and leak rate L:

$$\alpha_Q = \frac{\alpha_F\ F + \alpha_L\ L}{F + L} \qquad Q = F + L$$

The stable oxygen levels achieved after long term operation were 13.5 ppm at $F = 10$ l/h and 24 ppm at $F = 5$ l/h which gives a leak rate $L \approx 0.6$ ml/h, neglecting potential oxygen contamination of the fresh gas.

3.4 Readout Chamber

The ALICE TPC readout chambers are multiwire proportional chambers with cathode pad readout. Two different types of readout chambers are used in the TPC, the Inner Readout Chamber (IROC)) and Outer Readout Chamber (OROC). They have different wire geometries and pad sizes adapted to the different track densities. In the test setup an outer chamber is used.

3.4.1 Support structure

The aluminum body mechanically supporting the wires and pad plane is milled out of a monolithic aluminum block leaving ribs as mechanical support (see figure 3.8(a)). Holes in the frame allow the feedthrough of signal lines from pad plane to FECs via connectors and Kapton cables (see figure 3.8(b)). A cooling pipe is embedded in the aluminum body to keep the temperature constant and remove heat transfered from the FECs, in the test setup this cooling pipe was not used.

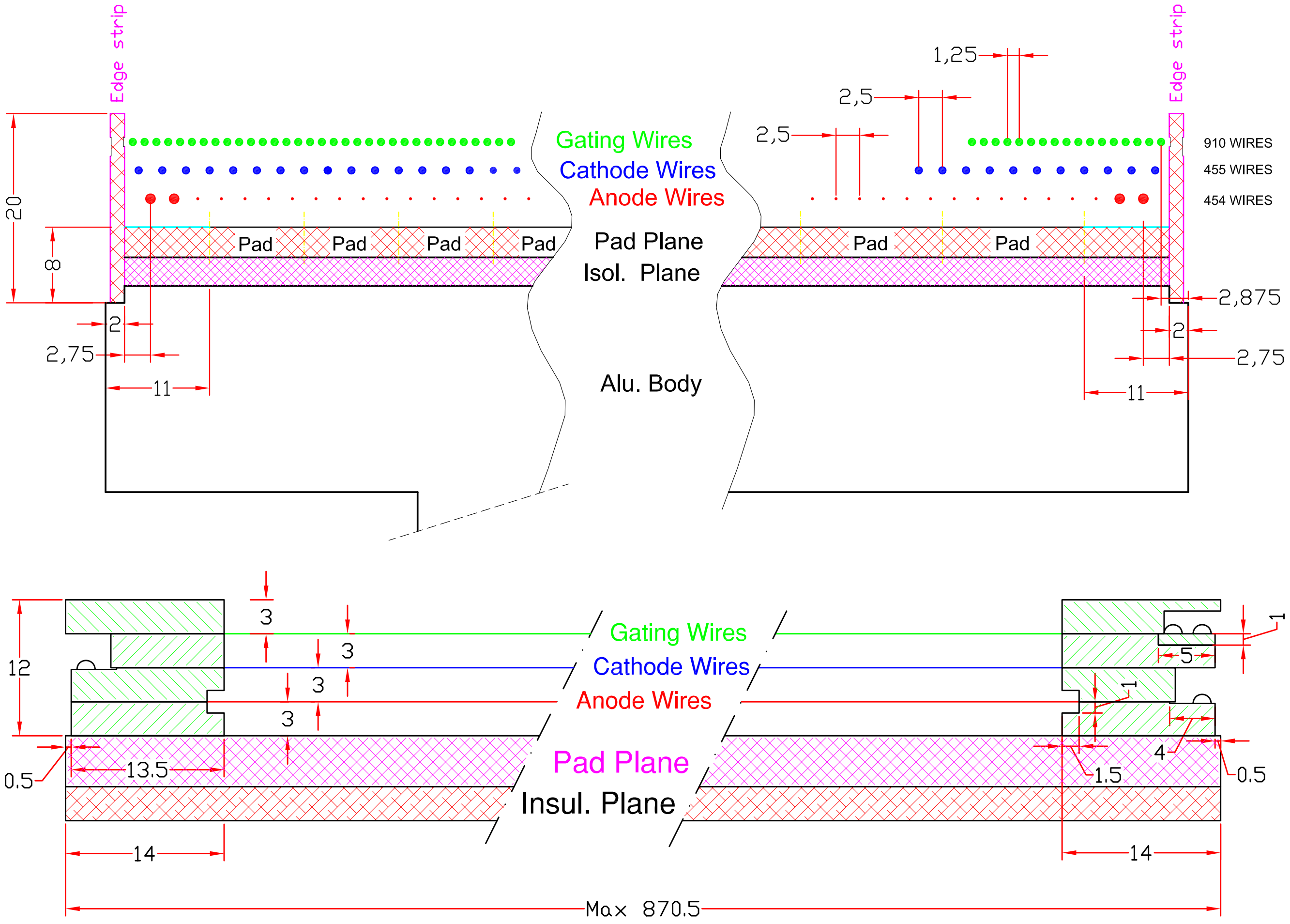

Figure 3.9: OROC wire geometry viewed in azimuthal (upper drawing) and radial direcation [26].

3.4.2 Wire planes and connection

The wire geometry for the OROC is shown in figure 3.9 (IROC: figure 3.10) and constists of three layers which are spanned in azimuthal direction: the anode wire grid (also called sense wires), the cathode wire grid and the gating grid. The spacing between pad plane and the anode wires and between the anode and cathode wires is 3 mm for the OROC and 2 mm for the IROC. The spacing between gating grid and cathode is 3 mm for both chamber types. The smaller spacing in the IROC leads (along with the smaller pad size) to a more narrow pad response function that is necessary to cope with the higher track densities. A *cover electrode* strip (see 3.9, labeled edge strip there) runs arround the top of the wire frames and can be connected to appropriate voltage to minimize distortions of the drift field on the chamber edges. In the test setup this cover connection was grounded through a 50 Ω resistor.

Anode wires

The anode wire grid is responsible for the avalanche creation and needs a strong electric field around the wires to cause secondary ionization. Thus the wires are thin (20 μm diameter) and are made of gold-plated tungsten which has a higher strength compared to Copper-Beryllium (CuBe) used for the other wires. To aviod high fields (and thus high gain) at the edge of the anode wire grid the last two wires on either side – called edge wires – are thicker (75 μm – same diameter as the cathods). The inner

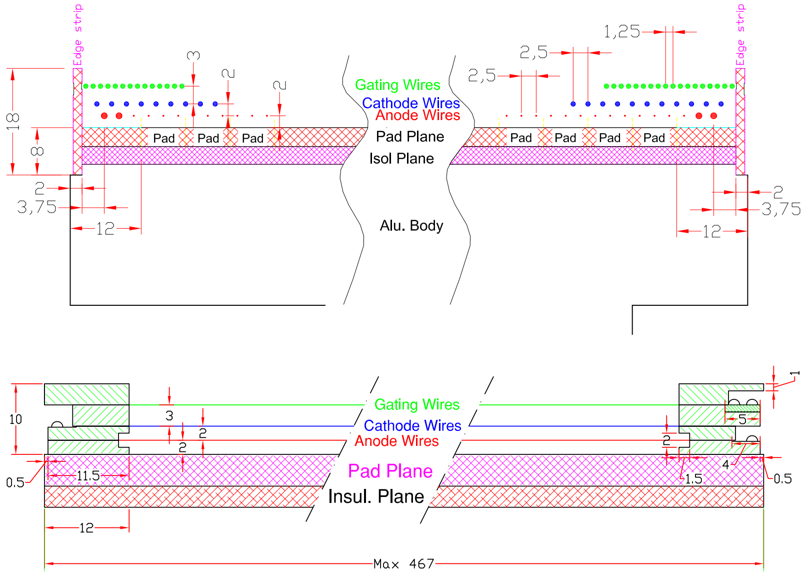

Figure 3.10: IROC wire geometry viewed in azimuthal (upper drawing) and radial direcation [26].

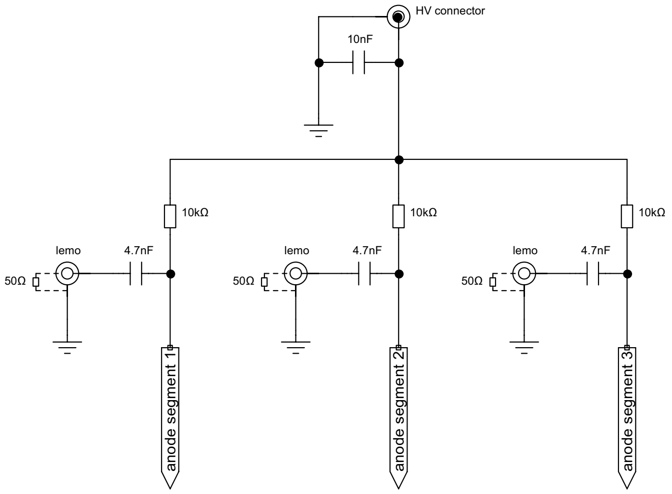

Figure 3.11: Connection scheme of the anode wire box for the outer part of the chamber (large pads). The "small pad" part of the connection contains four segments.

one is at anode potential and the outer one is held at the lower *edge wire potential*; an edge voltage of 600 V is used for the test setup.

The anode wire grid of the OROC is subdivided into seven parts, each part has its own protection restistor (10 kΩ) and buffer capacitor (4.7 nF). Four respectivley three anode wire segments are grouped together in two connection boxes (a circuit diagram is shown in figure 3.11), corresponding to the different pad sizes. After a common 10 nF buffer capacitor they are connected to the high voltage connector. This allows operating the chamber with different anode voltages at the different pad sizes, though this feature has not been used. Rather the two partitions were connected together to a single power supply to avoid (in the case of a trip) the high field between the two anode wires at the partition boundary. Each buffer capacitor is connected to a short cable with a lemo connector at its end that is routed out of the connection box and – while not used – terminated with a 50 Ω resistor. This additional connection was implemented to gain access to the sense wire signal via capacitive coupling.

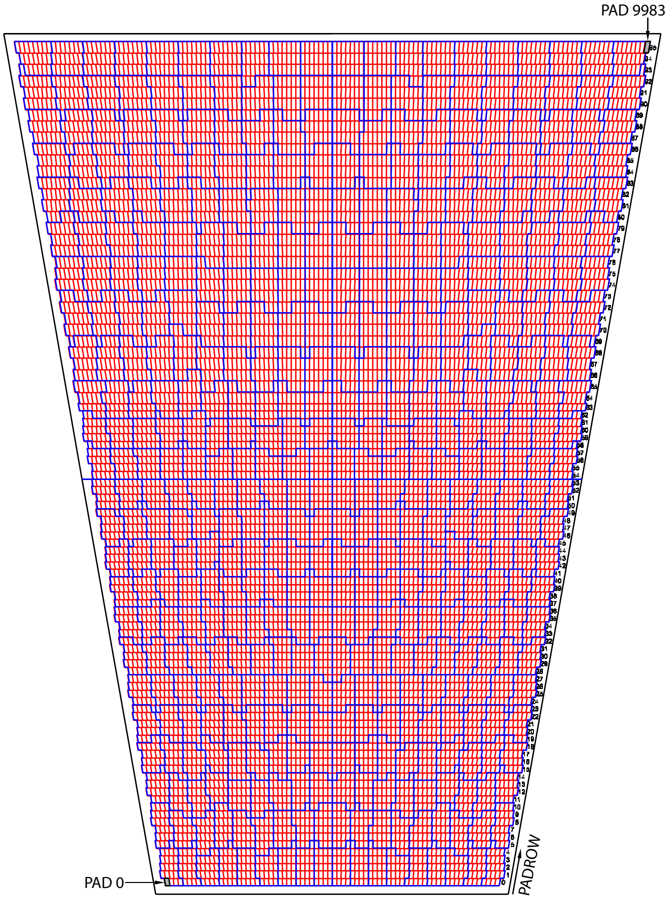

Figure 3.12: The OROC pad plane [5]. The blue lines sepereate groups of pads that are connected to one Kapton cable.

Cathode wires

The cathode wire grid with a spacing of 2.5 mm is displaced by half the wire pitch with respect to the anode wires and consists of the thicker 75 μm CuBe wires. The cathode wires of the test chamber are connected directly to the BNC connector – the internal 50 Ω connection to ground was removed so that the cathode current can be measured. If pulses are to be injected to the cathode wires (used for electronics calibration) an external 50 Ω resistor can be plugged in for terminating the signal.

Gating wires

The gating grid serves two purposes: in the closed state it prevents electrons from entering the amplification region and ions created in the amplification region to enter the drift region. When it is open it has to be fully transparent for electrons, obviously in this case is is also transparent for ions. Since the drift velocity is much slower for ions the distance to the anode wires of 6 mm (OROC) respectively 5 mm (IROC) is sufficient to collect ions created during the opening time of 100 μs. As apparent from figures 3.9 and 3.10 the gating grid extends very close to the side walls of the chamber body to prevent ions to leak out of the amplification region in this area.

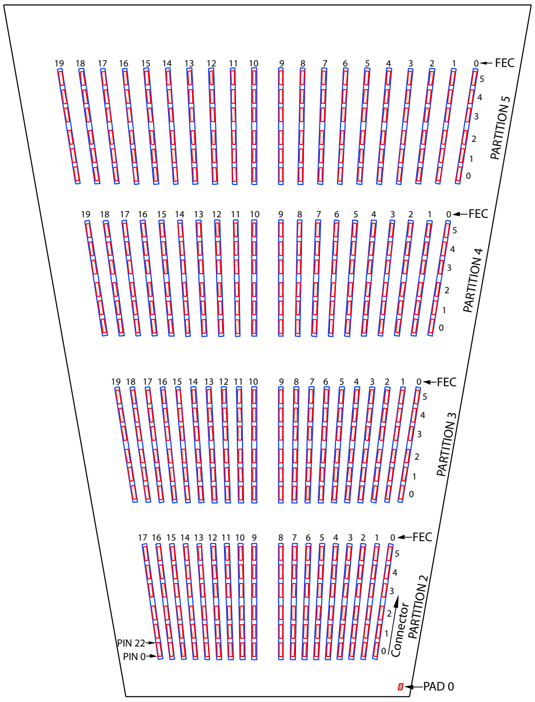

Figure 3.13: OROC backside view [5].

The gating wires have a spacing of 1.25 mm are alternately connected to the gating voltages $\pm\Delta V$. ΔV is adjusted to make the gate opaque for ions and was 90 V for the test setup. In addition, an common offset voltage V_0 is applied to all gating wires, corresponding to the potential at the wire position. It is chosen to maximize the electron transparency in the open gate mode . If the gating is closed (which is the case in the absence of a trigger) the voltage on the wires is $V_0 \pm \Delta V$ and drift lines from electrons (drift region) and ions (amplification region) end at the gating. When a trigger is received, the gating grid is opened by setting $\Delta V = 0$ and thus applying V_0 to all wires allowing electrons to enter the amplification region, start avalanche processed and induce charge on the readout pads. The offset voltage V_0 chosen for the test setup was -70 V.

The gating grid of the OROC is divided into two partitions, each fed by a gating pulser unit. Each of the four sockets for the gating grid is connected to a coil in series with the gating grid to reduce the switching time.

For the TPC with the high multiplicity and long drift distance the gating grid is essential to reduce space charge accumulation in the drift region. In the test setup the chamber is only operating at lower occupancy allowing to run with the gating grid constantly open. Furthermore the method of gain measurement as described in section 5.4.2 is only possible with the gating grid permanently open and the software trigger used for the readout can not be used to switch the gating.

3.4.3 Pad plane

The avalanches created around the anode wires induce charge in the cathode pads that is transfered to the electronics via flexible Kapton cables. Each socket is connected to 21 or 22 pads resulting in six cables for one FEC. The pad plane is manufactured as a multilayer Printed Circuit Board (PCB) and consists for the OROC of four pieces glued together (IROC: one piece). Figure 3.14 shows a cross section of the pad plane with the insulation plane and chamber body.

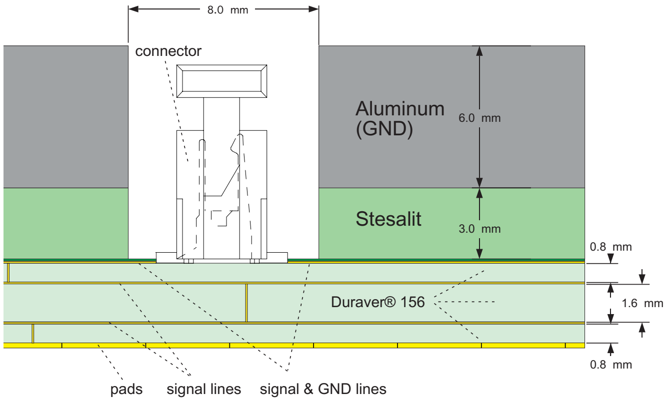

Figure 3.14: Cross section of the pad plane. [29].

	distance from beam axis (mm)	pad size (mm^2)	rows	pads
IROC	848.5-1321	4 x 7.5	63	5504
OROC	1346-1986	6 x 10	64	5952
OROC	1986-2466	6 x 15	32	4032
entire sector			159	15488

Table 3.1: Readout pads.

The size of the pads increases to larger radii, for the IROC it is 4 × 7.5mm^2 (all 63 padrows) the OROC is divided into two parts with different pad sizes: 6 × 10 mm^2 for the innermost 64 padrows and 6 × 15 mm^2 for the outermost 32 padrows (see also table 3.4.3). The pads are radially oriented and their shape is not exacly rectangular but they are slightly tilted (see figure 3.12) following the radial tracks in the TPC. The spacing between two adjacent pads is 0.1 mm [30] (except for the chamber boundaries) so the actual dimension of the pads is reduced by 0.1 mm in each direction.

3.5 Front-end electronics and readout

The front-end electronics (FEE) reads out and processes the signals from the cathode pads. The connection to the padplane is done via short Kapton cables and Harwin connectors.

A total number of 78 FECs is required to read out one OROC (43 for an IROC), the FECs are grouped into readout partitions (RP). One full sector (IROC and OROC) of the TPC consists of six readout partitions, numbered from 0 (innermost) to 5 (outermost). Table 3.5 summarizes the readout partitions. The numbering of the partitions and the FECs is shown in figure 3.13. The four partitions of the OROC are thus numbered from 2 to 5 and henceforth labeled RP2 through RP5. All FECs of one RP are connected a PCB backplane, a parallel bus which connects the FECs to the Readout Control Unit (RCU).

3.5.1 Front-end card

Each FEC [31, 32] has 128 input channels which are interconnected to the cathode pads via six Kapton cables. 16 analog circuits are integrated to a custom Preamplifier/Shaping Amplifier (PASA) chip; the digital part of the signal processing is done by the ALICE TPC Readout (ALTRO) chip [33] integrating 16 channels likewise. Figure 3.16 shows one side of the FEC, half of the ALTRO and PASA chips are visible.

chamber	readout partition	number of FECs	number of channels
IROC	0	18	2304
IROC	1	25	3200
OROC	2	18	2304
OROC	3	20	2560
OROC	4	20	2560
OROC	5	20	2560

Table 3.2: Readout partitions.

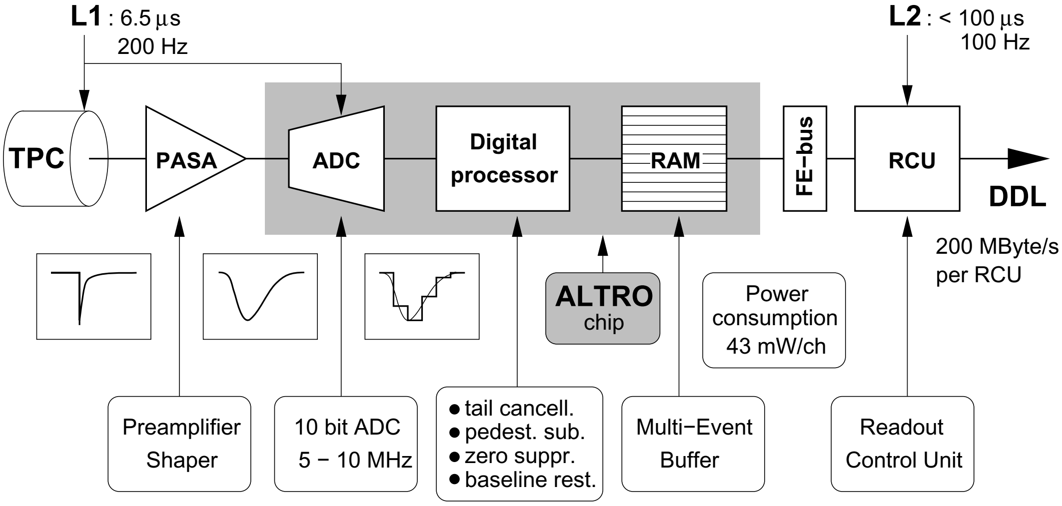

Figure 3.15: Basic compontents of the front end electronics.[2].

The processing chain for one single channel is shown in figure 3.15. The signal from each channnel is first processed by the PASA which amplifies and shapes the signal with a conversion gain of 12 mV/fC and a shaping time of 190 ns [31]. This results in a Γ-4 shape of the signal. The PASA output is subsequently digitized by a pipelined Analog-to-Digital Converter (ADC) with 10-bit dynamic range and up to 25 MHz sampling rate (part of the ALTRO – block diagram in figure 3.17). The following steps of the digital processing are: first baseline correction, tail cancellation, second baseline correction and zero supression.

The first baseline correction removes long-range (i.e. slow) baseline variations with a self-calibration circuit and corrects for systematic pertubations using a correction look-up table stored in memory. The tail cancellation removes the long tail inherent to wire chambers by approximating the signal with a sum of exponentials and removing all but fastest term. The second baseline correction removes fast baseline variations occuring inside the read-out window. Baseline correction and tail cancellation are important to obtain an effective zero supression, which is a lossy compression of the data. All values below a given threshold are discarded, an optional glitch filter checks for multiple consecutive values above threshold to accept the data. It is also possible to keep a specified number of pre- and post-samples around the peak. The zero-supressed data is formatted (compressed) to reduce the data volume before it is written to the Multi-Event Buffer. The implemetation with a pipelined ADC makes it possible to acquire up to 14 pretrigger samples. The two triggers relevant for the FECs are the Level-1 trigger (L1) and Level-2 trigger (L2): the L1 trigger starts the data acquisition of data to memory and has to be followed by a L2 to start the readout.

The described readout chain runs with the sampling clock which has a nominal frequency of 10 MHz. The clock signal is delivered from the RCU via the readout and control bus. In the test setup ADC and

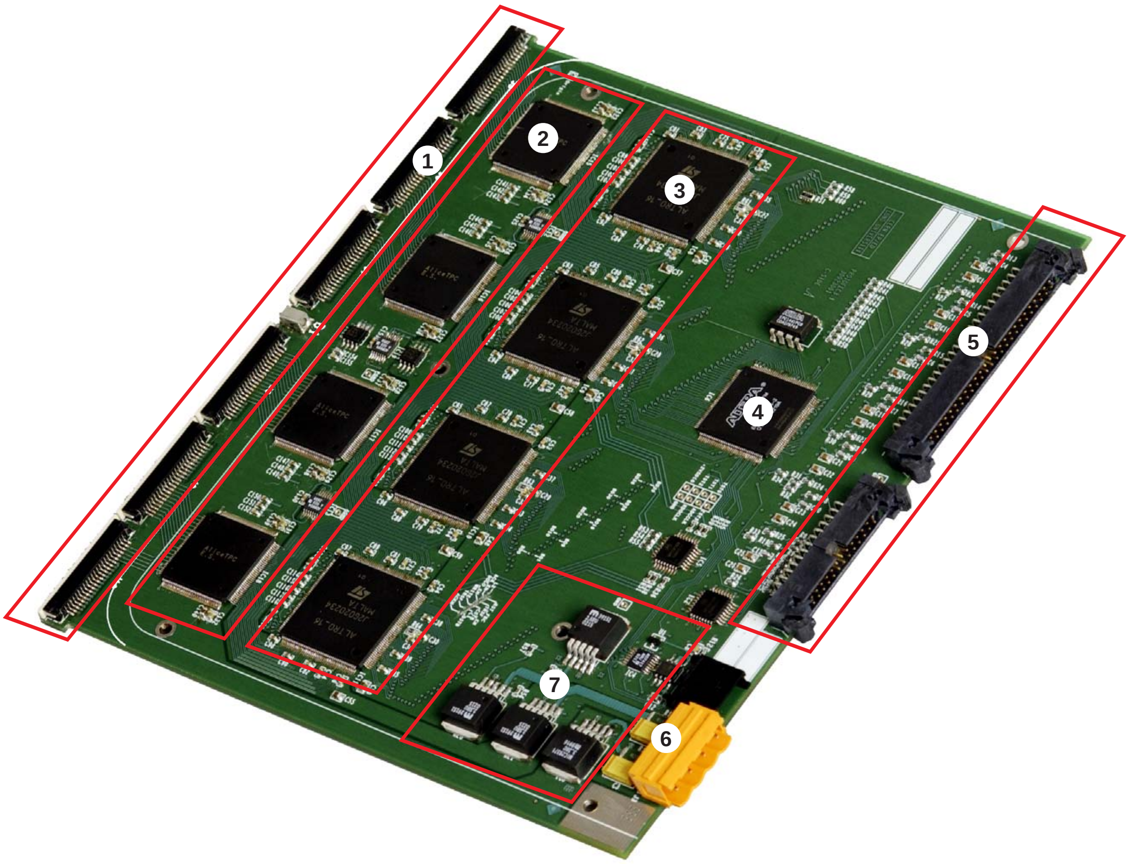

Figure 3.16: Layout of the FEC with the main compontents: Harwin connectors (1) for connection to the pad plane, PASA chips (2), ALTRO chips (3), board controller (4), readout and control bus connectors (5) connects to the RCU via the back plane, power connector (6) via patch cables to bus bar, voltage regulators (7). Another eight PASA and ALTRO chips and the GTL transceivers are on the bottom side.

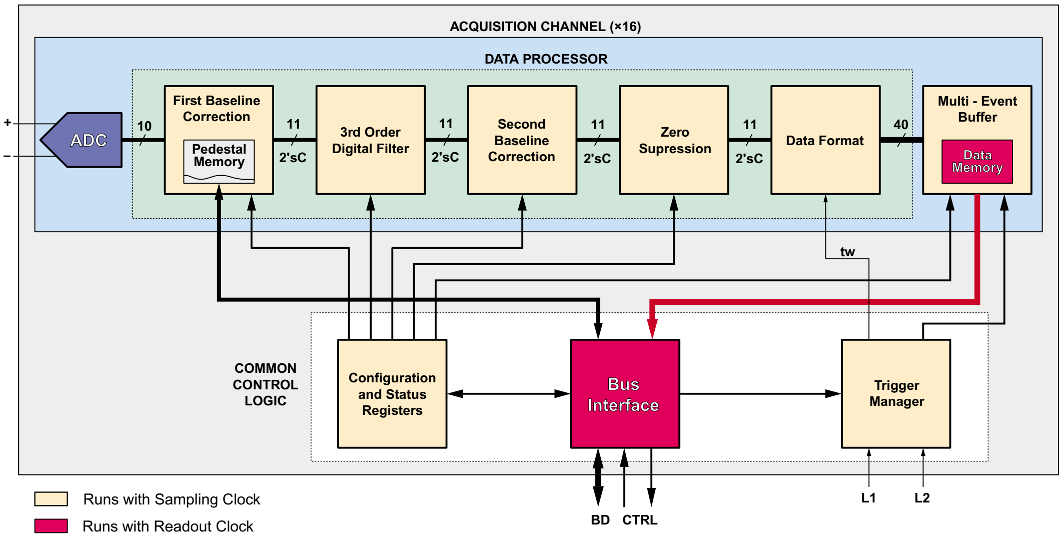

Figure 3.17: ALTRO block diagram illustrating the different steps of data processing. [34].

ALTRO were always running with this frequency. Besides the digitized data from the pads the FECs also have sensors to measure the board temperature, analog and digital voltages and currents. These values can be read out via the Detector Control System (DCS) boards attached to the RCU.

Configuration of the FECs is done from the RCU which is described in the next section. The logical connection between FECs and RCU is a parallel readout bus which is essentially an extension of the internal ATRO bus and a serial Front-End Control Bus (FCB). The ALTRO bus runs with a nominal frequency of 40 MHz and is 40 bit wide – resulting in a maximal data rate of 200 MB/s for the readout. It is used for configuration of the FECs and data readout. The Front-end control bus provides an independent access to the FECs and is used to monitor temperature, currents, etc.

Electrically the connection is done with a backplane (consisting of two parts) that connects the FECs of one branch to the RCU. Besides the ALTRO and Front-end control bus, the backplane has dedicated lines to distribute trigger and clock signals and switching the power on the FECs.

3.5.2 Readout control unit

The Readout Control Unit (RCU) [35, 36, 37] provides the interface between the FECs and the back-end systems, namely Data Acquisition, Detector Control System and Trigger and Timing Circuit (TTC) through the backplane described above. Between 18 and 25 FECs (the number in one readout partition) are connected to one RCU. The RCU servers the purpose of configuring the FECs, readout the data and ship it to the DAQ, monitor the temperatures, currents and voltages of the FECs and distribute trigger and timing information to the FECs.

A schematic of the RCU within the readout electronics is shown in figure 3.18. The RCU is connected to two mezzanine cards (see figure 3.19: the DDL Source Interface Card (DDL-SIU) which provides the interface to the optical fibres used to tranfer the data to the Readout Receiver Card (RORC); and the DCS board provides the interface to the detectors slow control system and the trigger system. The Detector Data Link (DDL) interface can also be used to access the ALTROs via the FCB. The optical link between DDL-SIU and RORC consists of two fibres with LC plugs and is capable of transfering 200 MB/s. The DCS board is equipped with a 10 MBit/s Ethernet interface for slow control and connection to the DCS and

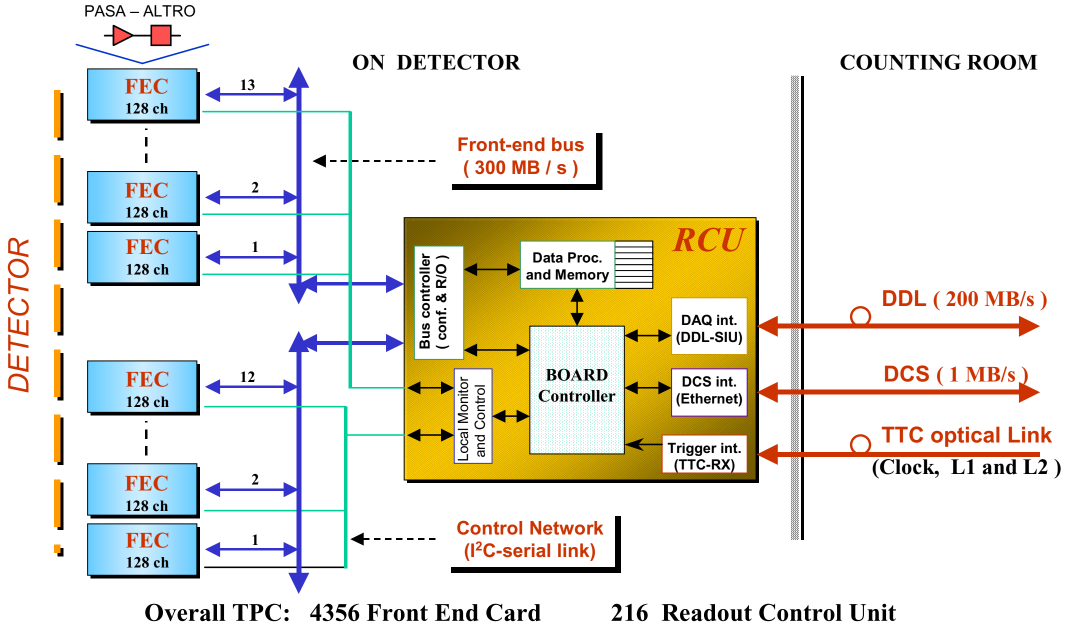

Figure 3.18: Schematic layout of the RCU and overall integration in the readout process.[36]

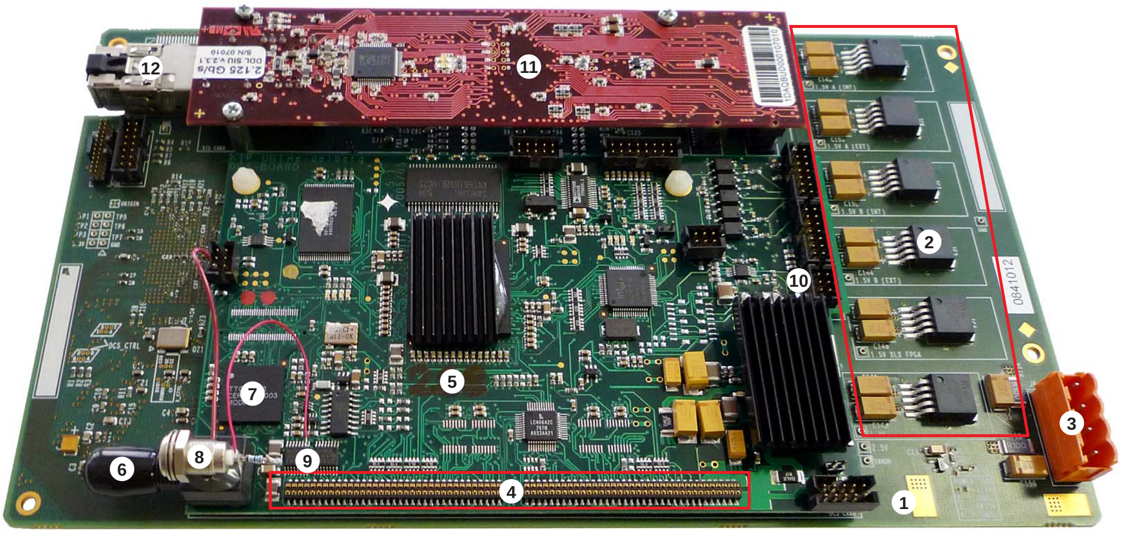

Figure 3.19: The RCU in the configuration used for the test setup. The RCU itself (1) with voltage regulators (2) and power connector (3) is connected (4) to the DCS board (5). The optical trigger (8) connected to the TTCRx chip (7) replaced by a lemo connector (8) connected to the LVTTL/LVDS converter, connector (10) provides the ethernet interface. The DDL-SIU (11) has an optical link (12) for data readout. The connectors to the backplane (for the link to the FECs), both FPGAs and the GTL transceivers are located on the bottom side.

an optical fibre connection for trigger and timing purposes. Software triggers are send over the ethernet connection (they can also be sent over the DDL connection).

The RCU contains two FPGAs (Field-Programmable Gate Arrays), an Flash-based ACTEl ProASIC+ and an SRAM-BASED XILINX Virtex II Pro which is the main controller and provides most of the functionality. The firmware for the ACTEL FPGA has to be written to the non-volatile memory only once This is done via the JTAG port on the RCU. The XILINX firmware is stored on a computer and loaded via the DCS board.

A dedicated Linux based computer (`tpcfee01.cern.ch`) is used for the communication with the DCS boards over the ethernet interface. The four DCS boards are connected to the computers `eth1` network interface via an ethernet switch. A DHCP (Dynamic Host Configuration Protocol) server running on the computer assigns IP adresses to the DCS boards which during startup mount special directories via the Network File System (NFS) protocol from the host PC. These directories are used to store the RCU firmware as well as additional software. The DCS board provide a shell (telnet/SSH) which is used to load the firmware for the XLINX with a special program (this is the only task that cannot be performed via the DDL). With the firmware the RCU becomes operational and can be accessed via the DDL link. From the DCS side the RCU shell (`rcu-sh`) provides direct access to the RCU registers, memory and instructions.

For testing the FECs and readout chain the program `altro-loopback`[6] is used, it provides a loopback test on the ALTRO and is useful to spot FECs, ALTROs or single channels that are causing errors. Configuration of the FECs and RCUs is done with the `rcuscope` and `fecscope` programs[7], they have been modified to write the correct L1-L2 latency (time between the L1 and L2 triggers) to the *Trigger Configuration Register*. The Configuration of the FECs includes the definition of the number of samples, trigger mode, zero supression, etc.; in the RCU the hitlist memory (defining the channels that are read out) has to be set. All these programs use the DDL connection to the RCU.

Readout of the slow control information from the FECs (temperature, voltages, currents) is done via the Distributed Information Management system (DIM) based on TCP/IP and using the ethernet connection as well. A DIM server is running on the DCS board and the information can be monitored with the DIM Information Display (DID). The TPC uses the PVSS software communicating via an intercom layer with the DCS boards.

External trigger

The triggers in ALICE are generated centrally by the Central Trigger Processor (CTP) and distributed to the Local Trigger Uni (LTU) of the subdetectors which further distribute the trigger signals to the front end electronics. The LTUs are also able to generate CTP signals (CTPEmulator). The trigger system is based on the LHC Trigger and Timing Circuit (TTC) system with optical fibres used to transmit the trigger and timing information. Therefore the DCS boards embeds a TTC Receiver (TTCRx) asic to receive and decode trigger signals. The timing information is used to synchronize the readout clock between the different RCUs (aka readout partitions).

For the test setup an LTU was not available, so the DCS boards were modified to accept an external LVTTL trigger bypassing the TTCRx chip. Figure 3.20 shows a detailed picture of the modification. The DCS board uses Low-Voltage Differential Signaling (LVDS) the TTCrx chip (used LHC-wide) Low-Voltage TTL (LVTTL) with a signal level of 3.3 V. A LVDS driver (with LVTTL input) provides the interface to

---

[6] written by Magnus Mager.

[7] written by Luciano Musa.

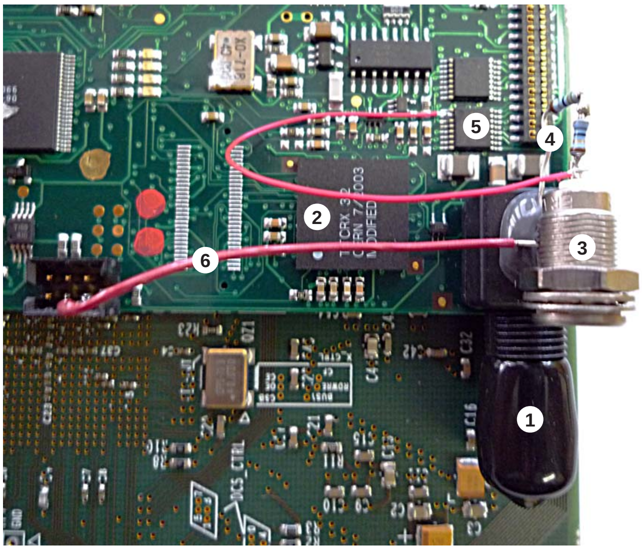

Figure 3.20: Close-up view of the trigger modification on the DCS board. The optical connector (1) and TTCRx chip (2) are disconnected from the driver (5) and replaced by a lemo socket (3) terminated by a 50 Ω resistor (4) and grounded to the DCS board ground (6).

the DCS board. To allow an external LVTTL trigger signal a lemo connector was glued on top of the ST connector and its signal line was connected to the LVDS driver chip and the shielding (=ground) is connected to an unused grounded pin on the DCS board. To terminate the signal a 51 Ω resistivity in soldered between signal and ground lines. The resistivity is split into two resistors (33 Ω and 18 Ω) so it is easy to modify the trigger for a normal TTL signal (5 V level).

The use of this external trigger has some impact on the timing: When the TTCRx chip receives a timing signal the sampling clock for the FECs is derived from this signal. In the absence of a valid incoming clock the RCU uses its own clock leading to unsynchronous readout of the different partitions (the FECs in one partition still get the same clock information).

To use the external trigger the RCU firmware has to be configured to generate the required trigger sequence from the single trigger received. For the RCU firmware used for the TPC in the 2008 runs (version 0908) this mode of operation did not work. A modified firmware was available later but came with a different data format that could not be decoded by the AliROOT readers.

3.5.3 Data acquisition

The Data Acquisition (DAQ) system is based on the Detector Data Link (DDL) [38, 39] and the DATE software [40]. The connection from the Source Interface Card (SIU) to the Destination Interface Card (DIU) is made with bidirectional optical fibres capable of a readout data rate of 200 MByte/s. The computer used to receive and record the data (`alicetpc01.cern.ch`) is equipped with two DAQ Readout Receiver Cards D-RORCs, each card has two channels, so four links (one to each readout partiton) exist.

The D-RORC is 64-bit PCI-X expansion card develeloped for the ALICE Experiment. It integrates two DIUs used to transfer data from the detector and uses the PCI bus to write the data directly into the computer's memory. In the TPC only one channel is connected to an RCU, the other one transfers a copy of the data stream to the High-Level Trigger (HLT).

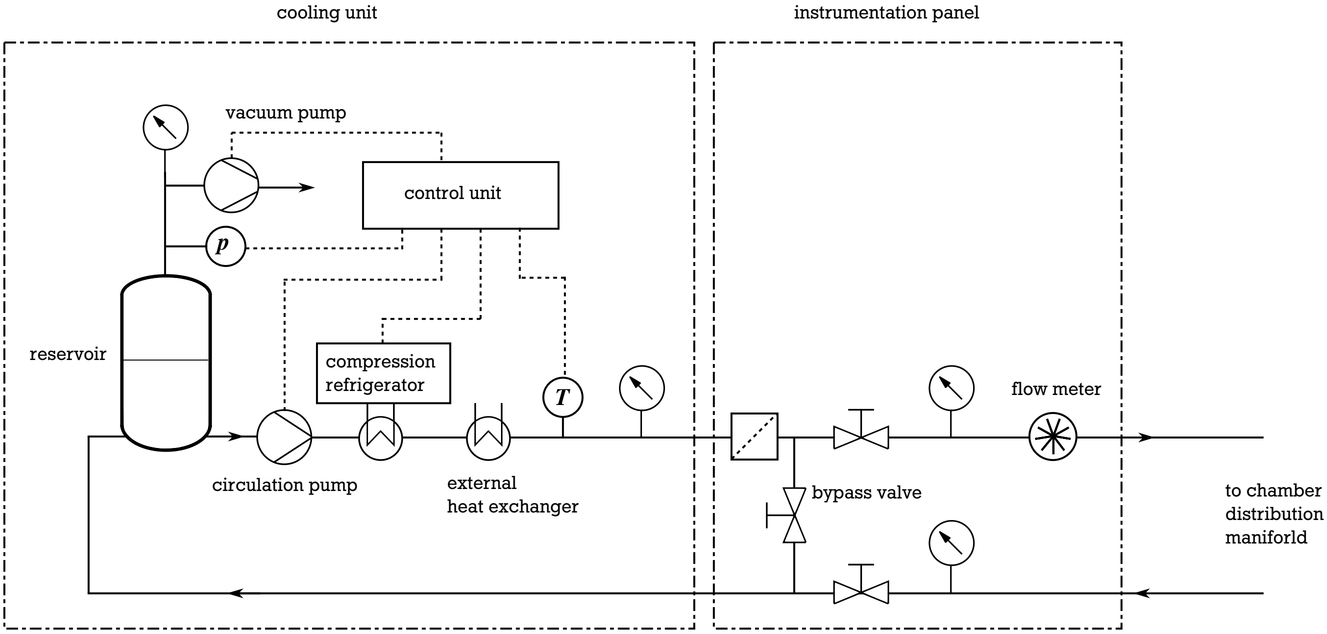

Figure 3.21: Schematic layout of the cooling system.

In the terminology of ALICE the readout computer is a Local Data Concentrator (LDC). The DATE software provides a Graphical User Interface (GUI) to configure, start and stop the data taking. It is used to write the data from the RORCS to RAW files. Errors and messages occuring during the readout are recorded to a database (done by `infoLoggerServer`), together with a graphical frontend (`infoBrowser` this helps to locate and fix errors occuring during readout. The DATE software also contains command-line programs to test the RORC and perform loopback tests on the SIUs.

The Online monitor, written in the ROOT framework and using some AliRoot classes, is a very useful tool to look at the data during the readout. This visual inspection gives an immediate impression on the data quality.

3.6 Services

3.6.1 Cooling

Each FEC has a power consumption of about 6 W [31], for the complete OROC with 78 FECs this sums up to a total power dissipation of nearly 500 W. To avoid over-heating of the electronics and to minimize heat transfer to the chamber the FECs have to be cooled. The FECs are wrapped in cooling plates made of copper. One side is equipped with a U-shaped cooling pipe the other half is connected by six screws which also ensure the thermal coupling of the two parts. In the TPC the RCUs are water-cooled as well, for the test setup they are sufficiently cooled by air convection.

The cooling system in use is a closed-cycle, leakless underpressude sytem similiar to the one used in the TPC. The advantage to have sub-atmospheric pressure in the whole system is that in case of a leak no water (that could potentially damage the electronics) is released. Demineralized water is used as a cooling liquid.

The main components of the cooling system are the cooling unit[8] including a vacuum pump to maintain the underpressure, a circulation pump, a refrigerating plant and a control system, a panel with valves (to control the flow), pressure gauges and a flow meter and the distribution of the cooling lines to the FECs.

The cooling unit has the capacity to supply two full-sectors of the TPC. Since the throughput of the circulation pump cannot be regulated, for the test setup most of the output has to be bypassed by a valve to avoid overpressure in the cooling circuits. The output temperature of the refrigerating plant was set to 16.5 °C resulting in a temperature of about 30 °C for the FECs (on-board temperature sensor). The flow is limited by the maximal pressure allowed in the cooling unit and was adjused to 7.5 l/min (corresponding to -150 mbar at the output) which is more than adequate to remove the heat from the electronics. The main cooling line from the cooling unit it connected to distribution manifold which supplys a variable number (6-8) FECs, interconnected with flexible silicone hoses (cf. figure 3.3).

The laboratory itself is cooled by two air conditioning units to remove the heat produced by all the equipment and keep the temperature at a stable level to the extend possible. Nevertheless temperature variations of about 2 °C could be observed.

3.6.2 Low voltage supply and grounding

The FECs require the supply with two different voltages 4.3 V for the analog part and 3.5 V for the digital part of the signal processing. These voltages are not used directly but lowered to 3.3 V respectivley 2.5 V and stabilized by linear voltage regulators[31]. Additional measures are taken to stabilize the reference voltages for PASA/ALTRO.

The power supply used for the test setup is a Wiener Plein&Baus PL 508 that was used for TPC tests in the clean room before and is very similiar to the PL 512 powering the FEE in the cavern. The voltages delivered by the power supply are floating and grounded only on the detector side through the FECs.

The currents for the supply of the FEC are remarkable: For one sector they are 83 A for the analog voltage and 133 A for the digital voltage. These currents need cables with large cross-sections, in the TPC the cables are about 40 m long causing a significant voltage drop. For this purpose the power supply has *sense lines* that are connected on the detector side (bus bar) and feed back the voltage to the power supply which attempts to keep the sense wire voltage at the desired voltage. For the test setup the cables are much shorter and the sense wires have been connected directly at the power supply side. However, it turned out that one connection between cable and bus bar had a larger restistivity and caused a noticeable voltage drop. With all FECs switched on the voltage is getting to low and has to be manually enhanced by about 0.3 V to ensure sufficient supply voltages for all electroncis.

The distribution of the LV to the electronics follows the design of the TPC. A distribution line (called bus bar) runs along the OROC, each readout partition is connected via a patch cable to the bus bar with a buffer capacitor (6800 μF) for each voltage.

The grounding of the FECs is done seperately for the analog and the digital part, the two grounds are connected through chamber and test box. Each FEC is connected with two short cables to copper bars attached to the aluminium body of the chamber (analog ground) respectively to the support frame (digital ground). The chamber itself is grounded through the shielding of the coaxial cables used for anode voltage, gating, cathode etc. and additionally connected with a thick copper belt to one of the electronics racks.

---

[8] The cooling unit was used during the commissioning of the TPC in SLX2.

3.6.3 High Voltage power supply

For the supply of the anode and edge voltages different power supplies are available. The Iseg EDS 20025p (the type used for the TPC) with a connection to the slow control PC via Controller-Area Network (CAN) bus has a current resolution of 4 nA which excludes it from use for direct gain measurements. Instead two Iseg CHQ 222M power supplies (with a Computer Automated Measurement and Control (CAMAC) interface) capable of measuring the current with a resolution of 0.1 nA are used. Each module has two indepedent power outlets, so one module is sufficient to supply the anode and edge wires, the other one is supplying the two PMTs used for the cosmic trigger.

Both modules feature the possibility to give two limits on the current. A *hardware limit* is set with a tuning screw on the module and can be set to either limit the current to this value or switch off (“trip”) the HV if the current exceeds the limit (“kill-enable”). In addition a *software limit* can be defined in the program controlling the power supplies that switches of the HV if the current rises above this limit. The hardware limit is reacting fast (order of ms) while the software limit has a much slower reaction time (a second or less).

3.6.4 Calibration Pulser

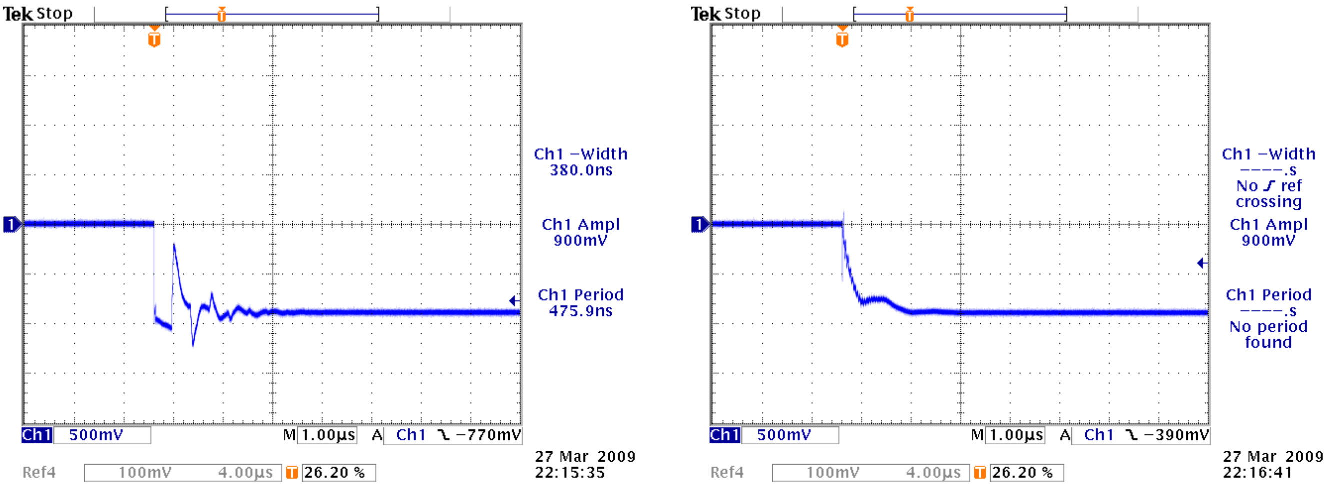

(a) With 50 Ω termination.

(b) With 50 Ω and additional 4.7 nF.

Figure 3.22: Calibration pulser signals.

The calibration pulser injects electric pulses to the cathode wires that can be used for calibration of the electronics, i. e. correction for the relative differences of gain and timing in the channels. That includes

- Test of the general operation of the readout chain to detect dead or defective channels.
- Detection of unconnected or improperly connected cathode or anode wires (so-called *floating wires*)
- Calibration of the electronics gain, where differences between the channels occur due to manufacturing tolerances.
- With pulses of different amplitudes: Determination of the linearity of the electronics.
- Calibration of the readout timing.

A special calibration pulser was designed for the TPC with connection to the ALICE DCS. In the test setup the pulses are generated using a dual timer unit (CAEN Model N93B) for the Nuclear Intrumentation Module (NIM) standard. The two timers have been connected to generate rectangular pulses with adjustable width and frequency. With an oscilloscope the shapes of the pulses were monitored. Since the internal 50 Ω resistor was disconneted to inspect the cathode current an external 50 Ω termination resistor has been placed as close as possible to the chamber. As apparent from Figure 3.22(a) there were still large distortions of the pulses from reflections (impedance mismatch). With an additional 4.7 nF capacitor this could be improved (figure 3.22(b)) for the sacrifice of rise time. It turned out that the modification leads to pulses induced on the padplane that were sufficient for the calibration. The pads couple capacitively to the cathode wires which leads to differentiation of the injected signal.

3.6.5 Trigger system

With the modified DCS board it is possible to trigger the readout with a LVTTL signal (3.3 V). This signal is delivered by the leCroy Model 688AL level adapter (NIM-TTL). The input to the level adapter can be connected to the cosmic trigger described below or to a timing unit generating single, manually initiated or periodic triggers. The output of the timing unit can also be fed to the gating pulser to open the gate or used to generate the calibration pulses. In connection with the planned laser operation the trigger can be taken from the lasers SYNC output and delivered to the RCUs. The timing unit can also be used to trigger the laser. Figure 3.23 shows an example of a trigger pulse. Alternatively a software trigger signal can be send via the DCS network.

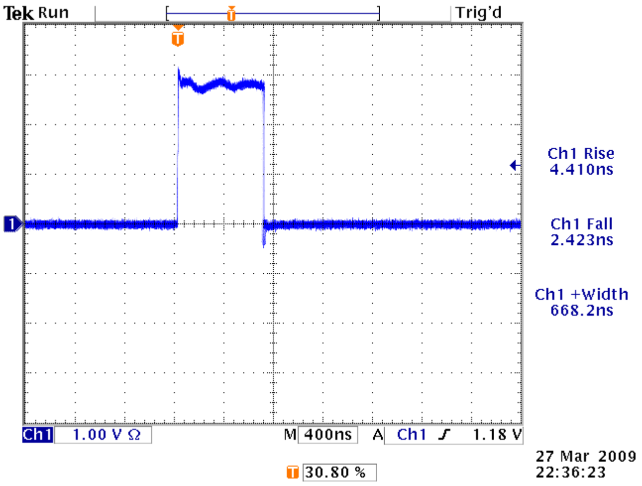

Figure 3.23: Example of a trigger signal sent to the DCS board (from cosmic trigger).

For pedestal runs, pulser data and data taking with the ^{55}Fe source the software trigger was used. The trigger signal is issued by executing a trigger command on the DCS board. This implies a jitter of the software trigger in different readout partitions.

Cosmic trigger

A setup to trigger on cosmic rays has been installed using the external trigger connection described above. Two organic scintillators with PMTs are installed: one above and one below the test box. The required electronics to generate a LVTTL trigger are plugged together using standard NIM modules. The

PMTs are supplied with HV of -1960 V (top) and -1980 V (bottom)[9] from an ISEG CHQ 222M two-fold HV PS.

The fast signals from the PMTs (figure 3.24(a)) are fed to leading-edge discriminators which produce a rectangular NIM pulse about 1 μs wide (figure 3.24(b)). A subsequent coincidence unit produced a standard signal if the pulses from the two PMTs overlap in time. Due to the relatively long discrimantor pulse of 1 μs the difference of a some ten ns in the signals from the two PMTs (mainly depending on the different characteristics of PMTs used and on the fact that the timing of a leading-edge discrimminator varies with the pulse amplitude) is not relevant. The output of the coincidence unit is a very narrow pulse ($\approx$ 1 ns), again a discriminator is used to transform it into a pulse of convenient length (600 ns). A Fan-In/Fan-Out unit splits the signal into four lines (one for each readout partition) and a 4-fold NIM-to-TTL converter transformes the negative NIM pulses to a positive LVTTL pulses with 3 V amplitude that are fed to the modifidied DCS boards.

The FEE cannot handle a second trigger before the last event is processed and read out, thus a mechanism to ensure an appropriate spacing between successive triggers is required. For this reason an artifical dead time is introduced by taking one outlet of the conicidence unit to start a timer whose output is fed back as a veto to the conincidence unit. The dead time can be easily adjusted to different readout configurations, for full readout at low rates a dead time of 10 ms was found to be sufficient.

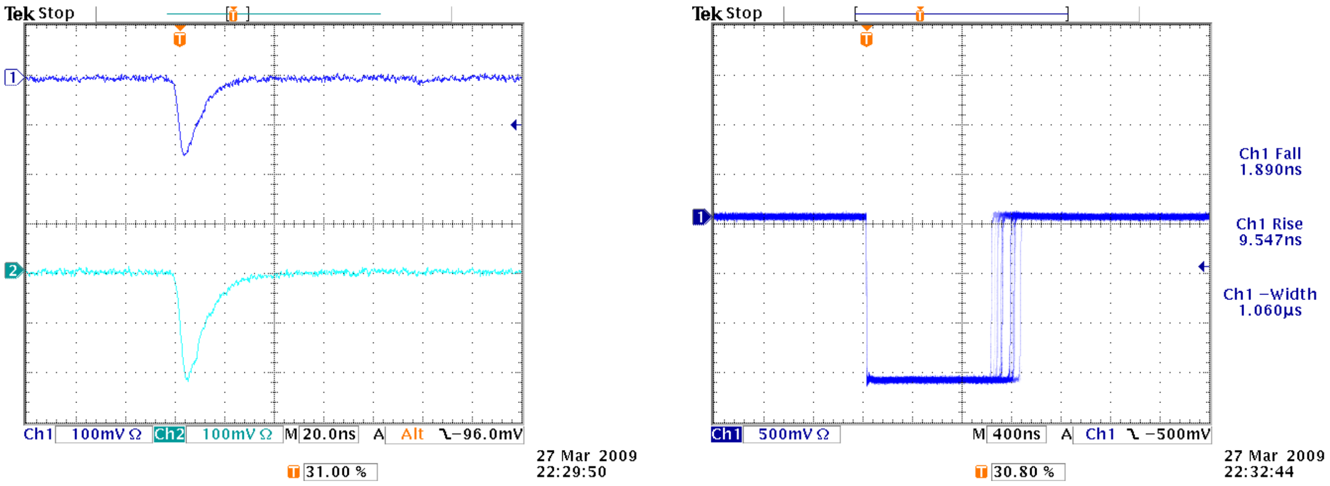

(a) (b)

Figure 3.24: Example of signals from the two photomultipliers (a) and result of the discriminator (b).

3.6.6 Slow control

For controlling and monitoring the services and the ambient conditions a Windows based computer with LabView programs, called Virtual Instruments (VIs) is used. Several different VIs are used for the different devices, they also provide the possibility to write the data to disk. For reading out analog signals a modular ADC system WAGO I/O is used. It uses the Profibus field bus for communication with the computer where an OPC Server is running and provides easy access to the acquired data. Different WAGO modules are in use digitizing currents (4-20 mA), voltages (0-10 V) and restistance (designed for measurements with a Pt100 temperature sensor).

---

[9] The voltage of the bottom PMT was increased compared to the specification to get a signal above the discriminator threshold for the whole active area.

The systems that can be controlled/monitored are

- The oxygen sensor installed at the exhaust is connected via a serial RS-232 interface and measures the oxygen content and the temperature.
- The absolute pressure transmitter installed close to the oxygen sensor delivers a 4-20 mA analog current output. The current is measured with the WAGO ADC and translated to the pressure in a VI.
- The cathode current is measured with Keithley Instruments 414A Picoammeter, which has an analog output that is digitzed and read out with the WAGO ADC. The different ranges have to be selected manually and adjusted also in the VI reading the currents.
- A Pt100 temperature sensor attached to the center rib of the aluminum ROC body is read out with the WAGO ADC.
- The high voltage power supplies for anode, edge and PMTs are read out and controlled via CAMAC (iseg CHQ 222M) respectively CAN bus and OPC server (iseg EDS 20025p).
- The low voltage power supply for the FEE is connected via the CAN bus and is used to measure and control the voltages and currents.
- The flow meter of the cooling unit has 4-20 mA output and can also be connected to the WAGO ADC.

3.7 Laser system

A laser is a powerful tool for calibrating a gas detector and studies on the drift velocity. The TPC has two laser systems (for the A-side and C-side) designed (and used) for calibration and alignment. Besides the straight tracks generated by the incident beam, laser light is scattered and can release electrons from metallic surfaces, particularly from the drift electrode. These electrons can be used to measure the drift velocity and field distortions.

In order to generate ionization in the gas the laser has to have a sufficiently short wavelength and a narrow beam with high energy densitiy since ionization occurs via two photon absorption.

The laser system is based on an off-the-shelf pulsed Nd:YAG laser with two frequency doubling crystals (Spectron SL404T Series) [41].

The laser medium is an yttrium aluminum garnet ($Y_3Al_5O_{12}$) crystal doped with neodymium. The Nd^{3+} ions replace a small (typically below 1%) fraction of the Y^{3+} ions in the crystal and are responsible for the laser emission. The crystal structure broadens the absorption lines of neodymium making the optical pumping (done with a flashlamp) more efficient. The strongest (60%) transition in the Nd^{3+} is in the near infrared and characterized by a wavelength of 1064 nm. With nonlinear effects the frequency of the laser light is doubled twice (by the *second harmonic generator* and the *fourth harmonic generator*) resulting in a wavelength of 266 nm. This corresponds to a photon energy of 4.64 eV, with a second order process it is possible to ionize organic impurities in the gas. The flash lamp is pulsed with a 10 Hz frequency. The short pulses of high intensity (with a duration of 15 ns and a frequency of again 10 Hz) are generated by a Q-switch inside the laser cavity based on a polarizer and a Pockels cell.

The repetition rate and the voltage for the flashlamp can be adjusted to control the pulse energy and rate. External triggering of the flashlamp and Q-switch is also possible. However, for stable operation of the laser it it preferable to run it with the nominal voltage and rate and use one of the syncronization outputs (flashlamp or Q-switch) to trigger the readout of the chamber.

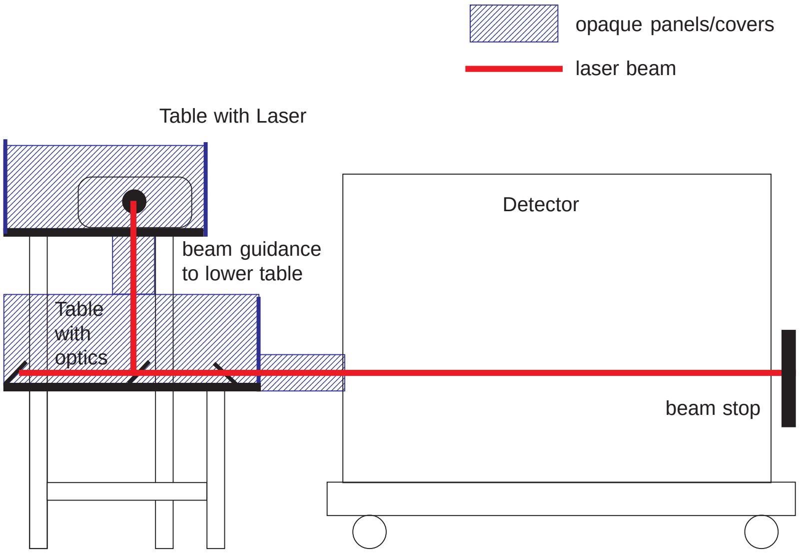

Figure 3.25: Planned laser setup. The beams will be entirely enclosed.

In the output of the laser head all wavelengths (i. e. 1064 nm, 532 nm, and 266 nm) are present. To extract the desired 266 nm, a setup of two prisms (Prism Harmonic Seperator) is used, the other wavelengths are dumped. With a system of mirrors the beam is guided to second table and finally to the detector. It is also possible to split the beam to generate two tracks or use a special micro-mirror system to generate fan-shaped tracks in the chamber.

The laser's Power Supply Unit (PSU) is supplied with cooling water. The laser itself was succesfully tested but the optics and part of the safety installation has to be completed in order to obtain the operating permit.

Safety Measures

Following the safety regulations at CERN the following protection scheme has been finalized. The beam path will be completely enclosed by light-tight tubes, the optical instrumentation will be covered en bloc with black-painted aluminum sheets. This is the foreseen normal operating procedure.

For alignment of the laser the mirrors and beam have to be accessible, while it is necessary to ensure that no laser light can leave the laboratory and no one can enter while the laser is running. It is thus planned to complete the sealing of all windows with opaque materials (0.5 mm aluminum sheets painted flat black on the inside to reduce reflections); an interlock has been installed at the entrance door and interconnected to the internal interlock systems of the laser preventing the laser from operating when the door is open. A warning lamp is installed outside the laboratory and switched on automatically when the laser is running. Figure 3.25 gives an impression of the intended setup.

4 Data Analysis

The DATE software [39] is used to receive the data from the detector and writes it to disk in a RAW file format. A unique number is assigned to each run, the RAW data is written split into more files if the data volume exceeds a certain limit defined in the DATE software (1 GByte was used as a limit). To analyse the data a set of classes has been written within the `ROOT` framework [42].

The usual procedure of data analysis after recording the data consists of the following steps:

- The RAW data is converted into a ROOT file which is used by all further steps. The ROOT file contains many `Event` objects that are aggregated by a single `Run` object. The `Event` objects contain the data along with the mapping information. In the `Run` object meta information about the run is stored. The integrated compression of `TFile` reduces the date volume to about one third compared to the RAW data.
- Extraction of pedestal and noise information that is stored in a `Pedestal` object that is written to a pedestal file (only for pedestal runs).
- The pedestal information is used to perform baseline subtraction and zero supression. All the `Event` objects are transformed into `EventBS` objects that are written (along with the `Run` object) to a file. The class `EventBS` inherits from `Event`.
- For runs with the calibration pulser the zero-supressed data are used to extract the differences of the channels (as a relative gain). This information is stored in a `Calibration` object and also written to file.
- With the use of the calibration information the `EventBS` objects are then transformed to `EventCalib` (inheriting from `EventBS`) which have the signals normalized according to the calibration and are written to file.
- The cluster finder works on `EventBS` or `EventCalib` objects and creates a `Cluster` object containing the information. A `Clusters` or `SimpleClusters` object is created composed of many `Cluster` objects.
- Macros for the ROOT CINT are used to generate plots and extract properties of events or clusters. They use the other classes and the static functions of the `Run` class.

The `Run` class is the main class which contains the information about a single run and provides functionality to load data from disc, perform zero supression, find clusters etc. It acts only as a kind of abstraction layer, the code performing the operation is part of the corresponding classes.

The class `Event` contains the data of one event along with the mapping information, it is created by calling a static member function and uses the `AliTPCRawStream` and `AliRawReaderDate` classes from the `AliRoot` framework. It is stored in a `ROOT` file and taking advantage of the integrated compression of `TFile` it reduces the size of the raw data to about one third.

The `Pedestal` class is created from many events (typically one complete run) and stores the pedestal and noise information for every single pad and stored to a `ROOT` file as well. It contains a function to extract the pedestal values from a given event, the Run class loops over all events in a run. The pedestal and noise values are obtained from gauss fits to the ADC values of all timebins in many events and calculated for every channel.

The stored `Pedestal` class is used by the `EventBS` class (which inherits from `Event` to perform an offline baseline subtraction and zero supression. The desired zero-supression threshold is given in units of the noise value σ_{noise}. The result is again stored to a `ROOT` file, with a compression factor of 30 compared to the raw file size (for a 3 σ threshold).

The class `Calibration` is created from the data of a pulser run and contains the relative gains. It is used to convert `EventBS` objects to `EventCalib` objects. The class `EventCalib` inherits from `EventBS`.

The `Cluster` class contains all values extracted by the cluster finding algorithm. Its purpose is only to aggregate the information about a single cluster and is thus much like a C-struct (with all member variables public).

Cluster finding is performed by the classes `Clusters` and `SimpleClusters` it also contains the information about every cluster (stored in an `TObjArray` of `Cluster`). The cluster finding algorithm of the two classes are different. The class `Clusters` looks for local maxima and extends the cluster in the time, row, and pad direction until it either hits zero or the beginning of another cluster (indicated by rising ADC values). A glich filter that accepts a given number of samples in time that are larger is optional. The class `SimpleClusters` also starts at local maxima but assumes a fixed size of the cluster, i. e. a given but fixed number of pads, rows, and timebins are evaluated. Both classes store the information in `Cluster` objects and calculate the values given below for each cluster.

Since the Run and Cluster classes are the main classes that are used in the analysis scripts their functions and variables are described to more detail below.

4.1 The Run class

The class Run serves two purposes: Instances of the class are stored along with the Event objects to a file and provide meta information on the run as well as functions that allow access to the event. Static functions provide the functionality to write and read data to files and act as an abstraction layer between the functions of the other classes and the ROOT macros.

For all methods that are reading or writing data to files the run number can also be passed as a parameter instead of a filename. In this case the environmental variables `$ RAW_DATA` and `$ ROOT_DATA` are evaluated for the path, the filenames are generated automatically from the run number and type of file. If the same operation (with different parameters) is performed twice (e. g. zero supression with different thresholds) and the run numbers are used instead of filenames the second evaluation will override all previous data.

Below follows a description of the static functions that are used to write data:

`ConvertOldFile`
converts the data from an "old-type" file to the current format [1]

`ConvertToRoot`
converts the RAW data to a ROOT file containing Event and Run objects

`WritePedestals`
Takes a ROOT file, extracts the pedestal and noise information and writes the resulting Pedestal

---

[1] This was necessary because the data format (Event class) underwent major changes in the course of data analysis and most of the recorded data was only available in the old format (most of the RAW data had to be deleted due to limited disk space).

object to file. As an option it can skip events tagged as “noisy events” and channels that are believed to be defective (i.e. not showing a reasonable signal).

`WriteCalibration`
Takes a file with zero-supressed data and extracts the calibration information which is written to file in a Pedestal object.

`WriteBS`
Converts the data from a ROOT file to a file with zero-supressed and baseline subtracted Events. As parameter the zero-supression threshold (default: 3 σ_{noise}) can be passed along with the direction to skip noisy events.

`WriteCalib`
Takes a calibration run as parameter and converts a zero-supressed file to a calibrated file containing EventCalib objects.

`WriteClusters`
Invokes the clusters finder to extract clusters from a given zero-supressed file and writes the cluster information into a cluster file.

`WriteCalibClusters`:
Does the same as WriteClusters, but when called with a run number as argument it uses a different naming of the files.

`WriteSimpleClusters`:
Looks for clusters with the “simple” algorithm that integrates over a fixed number of pads, rows and timebins.

The static functions that are used to read the data from file are all named with LoadXXX. They read an create an object by reading it from a file and return a pointer to this object. Object ownership is transferred to the caller who has duty to delete is. These static functions are

`Load`:
Loads a Run containing non zero-supressed data from file and returns a Run object.

`LoadCalibration`:
Reads a calibration file and returns a Calibration object.

`LoadCalib`:
Same as Load but for calibrated data.

`LoadBS`:
Same as Load but for zero-supressed data.

`LoadPedestal`:
Load and returns a Pedestal object from file.

`LoadClusters`:
Reads a cluster file and returns a Clusters object.

`LoadCalibClusters`:
Same as LoadClusters but for Clusters from calibrated data.

`LoadSimpleClusters`:
Similar to LoadClusters returns a SimpleClusters object.

4.2 The Cluster class

Instances of the `class Cluster : public TObject` are solely used to store the information about clusters extracted from the zero-supressed data. Thus all member variables are public and it contains no functions at all.

Below follows a description of the member variables which are all of primitive types defined by `ROOT`.

`UInt_t clusterID`:
A unique number to identify the cluster within a run (starting at 1).

`UInt_t clusterNumber`:
Number of the cluster within one event (start at 1).

`UInt_t run`:
Unique number of the run (assigned consequecutively by the `DATE` software).

`UInt_t pedRun`:
Number of the run that was used for pedestal and noise calculation.

`UInt_t event`:
EventID corresponding to the cluster.

`UShort_t nPads`:
The number of pads (= channels) contributing to the cluster.

`UInt_t nValues`:
The total number of contributing elementary ADC values (timebins × pads).

`Bool_t isIsolated`:
Is the cluster "isolated" in space and time (not overlapping with other clusters nor touching boundary; see below)?

`Bool_t isOverlapping`:
Is the cluster overlapping with other clusters (either in space or time)? Among others the `qSum` value might be incorrect.

`Bool_t isAtBoundary`:
Is the Qmax value of this cluster in the first or last timebin? Part of the signal is definitely lost.

`Bool_t isToBoundary`:
Is the first or last timebin contributing? In this case part of the signal might be lost.

`Bool_t isAtEdge`:
Is the pad with the Qmax value at the (spatial) edge of the readout area? The edge of the readout area can also be a channel marked as defective. In this case it is likely that part of the signal is lost.

`Bool_t isToEdge`:
Is a pad at the (spatial) edge of the readout area contributing? Part of the signal might be lost.

`Float_t sigma`:
The sigma noise value (ADC counts) of the pad with the maximal value.

`Double32_t qMax`:
The Qmax value, ADC value of the highest peak in the cluster (baseline subtracted).

`Double32_t qSum`:
The Qtot value, total charge of the cluster calculated as the sum over the ADC values of all pads and timebins contributing.

`UShort_t padMax`:
The pad of maximal signal (starting at 0 in each row).

`UShort_t rowMax`:
The row containing the pad with maximal signal (starting at 0 for the first row in the OROC).

`UShort_t timeMax`:
The Timebin of maximal signal.

`Double32_t padSum`:
The cluster position in pad direction calculated as center-of-gravity.

`Double32_t rowSum`:
The center-of-gravity position of the row.

`Double32_t timeSum`:
Center-of-gravity position in time.

`UShort_t padLow`:
Lowest pad number contributing.

`UShort_t padHigh`:
Highest pad number contributing.

`UShort_t rowLow`:
Highest row number contributing.

`UShort_t rowHigh`:
Highest row number contributing.

`UShort_t timeLow`:
First timebin contributing.

`UShort_t timeHigh`:
Last timebin contributing.

`UShort_t sizePad`:
Cluster “size” in direction of padrow (=`padHigh`-`padLow`+1).

`UShort_t sizeRow`:
Cluster ”size“ in direction of row (=`rowHigh`-`rowLow`+1).

`UShort_t sizeTime`:
Cluster “duration” (=`timeHigh`-`timeLow`+1).

5 Measurements and Results

With the setup described in the previous chapter it is possible to study the characteristics of the chamber under various conditions, especially under higher gains than currently used in the TPC. The measurements carried out within this thesis concentrated on investigating the gain with the use of an iron-55 X-ray source. Besides that the pedestal and noise behavior and calibration pulser data were carefully inspected. Data with cosmic rays were taken mainly as an operational test of the trigger setup.

For the measurements described in this chapter the voltages listed in table 5 are applied unless otherwise noted. The setting of the electronics and the ambient conditions encountered are also indicated in this table.

drift electrode	−3000 V
anode wires	1550 V
edge wires	600 V
cover strip	0 V (grounded)
gating wires offset	−70 V
gating wires bias	±90 V
RCU firmware version	0908
number of timebins	1000
sampling frequency	10 MHz
zero supression	off
baseline subtraction	off
trigger	software via DCS
gas flow	10 l/h
oxygen fraction	20.5 to 24.5 ppm
temperature	19.1 to 21.7 °C
pressure	954 to 972 mbar

Table 5.1: The default voltage and electronics settings and operating conditions. The pressure has not been under survey for all runs.

The terms *Qmax* and *Qtot* are used throughout this chapter. Qmax denotes the ADC value corresponding to the maximum pad and time bin (it is the amplitude of the discretized signal or cluster). The total number of ADC counts in a cluster or signal is named Qtot and is calculated as the sum over all timebins (for a signal) and – in the context of clusters – also the sum over all pads.

5.1 Test with FEE off

One of the first tests done with the chamber was the operation with the FEE off and high voltage on. During the commissioning of the TPC an anode wire broke under this configuration and had to be replaced. This lead to the concern that this could be caused – or at least promoted – by a charge-up of the readout pads. The charge sensitive preamplifiers have a large impedance to ground when powered off and (positive) charge created in avalanches could accumulate at the pads.

The chamber in the test setup was running for long periods of time[1] with the FECs off and anode voltage applied without any noticeable effect. During gain measurements a wire broke, which turned out to be a thicker edge-wire (see appendix A); the FECs were turned off at that time.

After completion of the electronics a dedicated test was performed. For this test the FECs were switched on and the iron-source was placed at the chamber center with the gating grid permanently open to produce as much charge as possible. The currents on the anode ($\approx$12 nA) and edge wires ($\approx$0 nA) as well as the cathode wires ($\approx$ 4.5 nA) were monitored over several ten minutes before the FECs were switched off. The currents were furthermore monitored for more than three hours without any evidence for a charge-up (no current changes). This leads to the conclusion that it does not implicate an endangerment to leave the HV on with the FECs off.

5.2 Pedestal and noise studies

The output of the ADC is – even in the absence of a phyiscs signal – not zero. Electronic noise is inherent to all electronic circuits. In addition, the wires in the chamber, the tracks on the PCB and the Kapton cables connecting the FECs to the padlane act as antennas and couple external electromagnetic fields to the input of the ADC. These effects cause fluctuations of the signals called *noise*. These fluctuations occur around a mean value that is called *pedestal*. It is a permanent offset of the ADC but might chance over time e. g. due to temperature effects.

Pedestal and noise values are important to know: For every ADC channel the pedestal value has to be subtracted before the data can be processed further. This can be done in the ALTRO (as part of the second baseline subtraction) or during the offline analysis. In the course of this work only non zero-supressed data has been taken and both pedestal substraction and zero supression were performed offline. The noise value determines the threshold for zero-supression and influences the energy resolution. The design specification for the TPC electronics demands a noise of 1000 electrons [30], corresponding to one ADC count (with a conversion gain of 6 ADC counts/fC). The values achieved for the electronics on its own is lower, about 700 electrons. With the TPC in the final setup values below 1 ADC count have been achieved for most channels [7]. A compilation of noise and pedestals for the test setup is shown in table 5.2.

To obtain the pedestal and noise values the detector is run with a random (software) trigger. Usually 100 to 200 events are recorded, ensuring sufficient statistics. Figure 5.1(a) shows the signal from one channel and one event obtained during a pedestal run. For every channel (and all events in the run) the ADC values are filled into a histogram (see figure 5.1(b)), and a gaussian distribution is fitted to the data. Its mean value is stored as the pedestal and the standard deviation (sigma) is used to characterize the noise value. The advantage of fitting a gaussian over simply taking mean and RMS of the distribution is that the fit is less sensitive to outliers.

The pedestal distribution for all channels (figure 5.2(b)) is gaussian-shaped around a mean value of about 50 ADC counts and not different from the distribution measured with the TPC [7]. The map (figure 5.2(a)) reveals that there are two FECs that have noticeably different pedestals, but are still within the specification. Two FECs are missing in RP5: The topmost one (FEC 19) was not working at all and has been exchanged later and at the bottom one card (FEC 0) is not installed at all, the pads are connected to chamber ground. Also a dead ALTRO on FEC 18, RP 5 is visible

---

[1] At the time not all readout components were available and operational but first tests were performed.

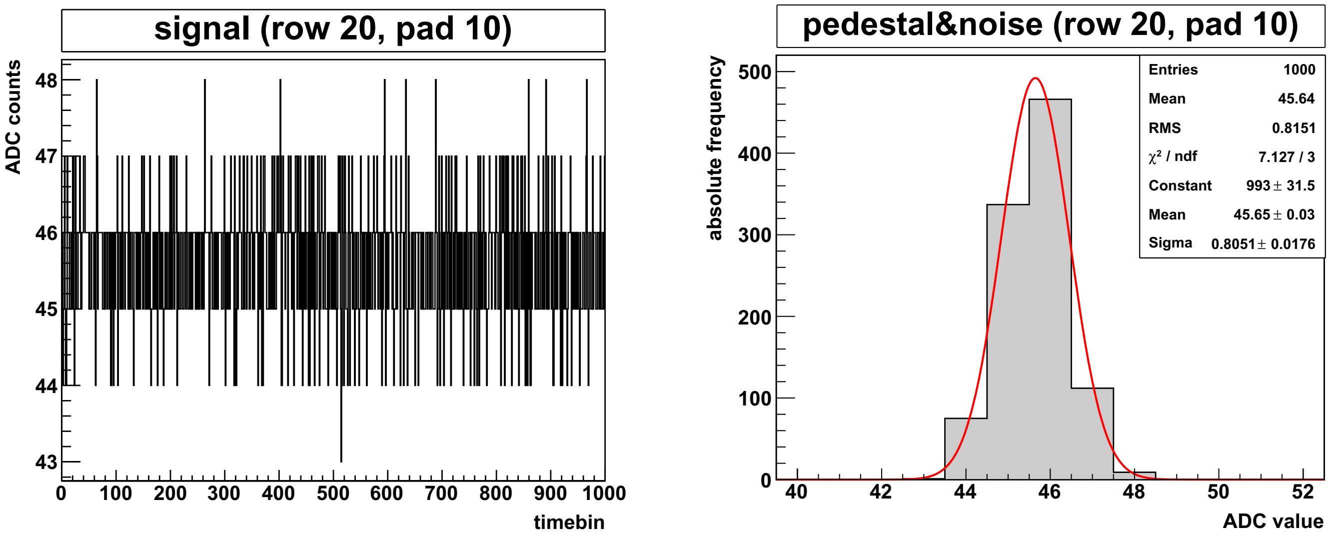

(a) Signal from an individual pad.

(b) Distribution of the signal with a fitted gaussian to determine pedestal and noise.

Figure 5.1: Illustration of pedestal and noise for a single channel and one event. For the actual extraction of pedestal and noise information a few hundred events are used.

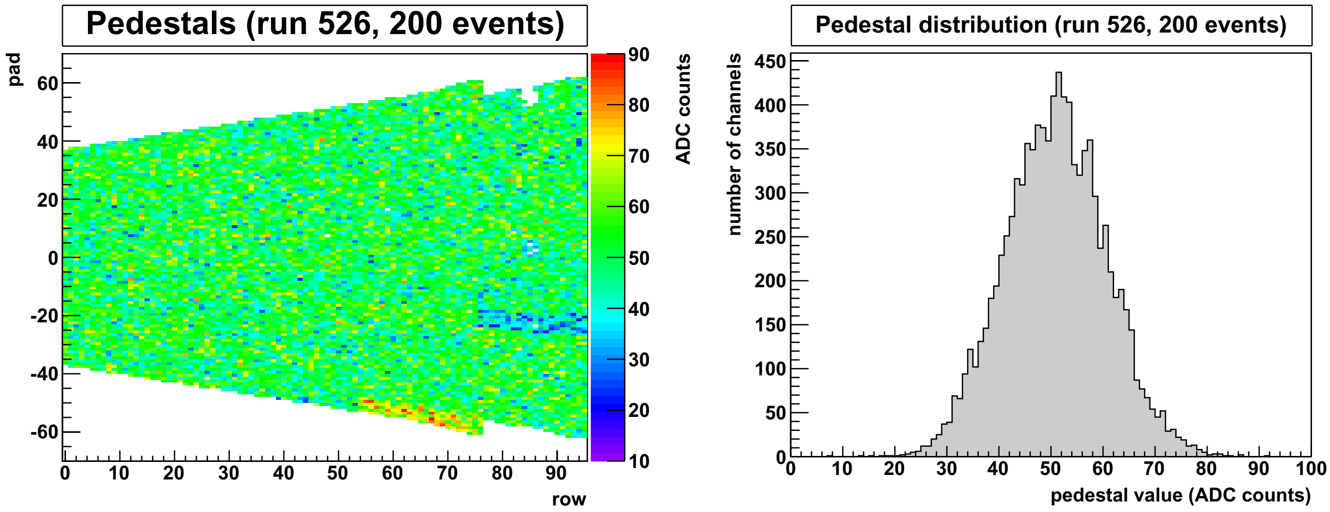

(a) 2-dimenional distribution of the pedestal values for individual channels. FECs with unusual pedestals are clearly visible as well as dead/missing FECs and one dead ALTRO.

(b) Overall pedestal distribution.

Figure 5.2: Pedestal distributions.

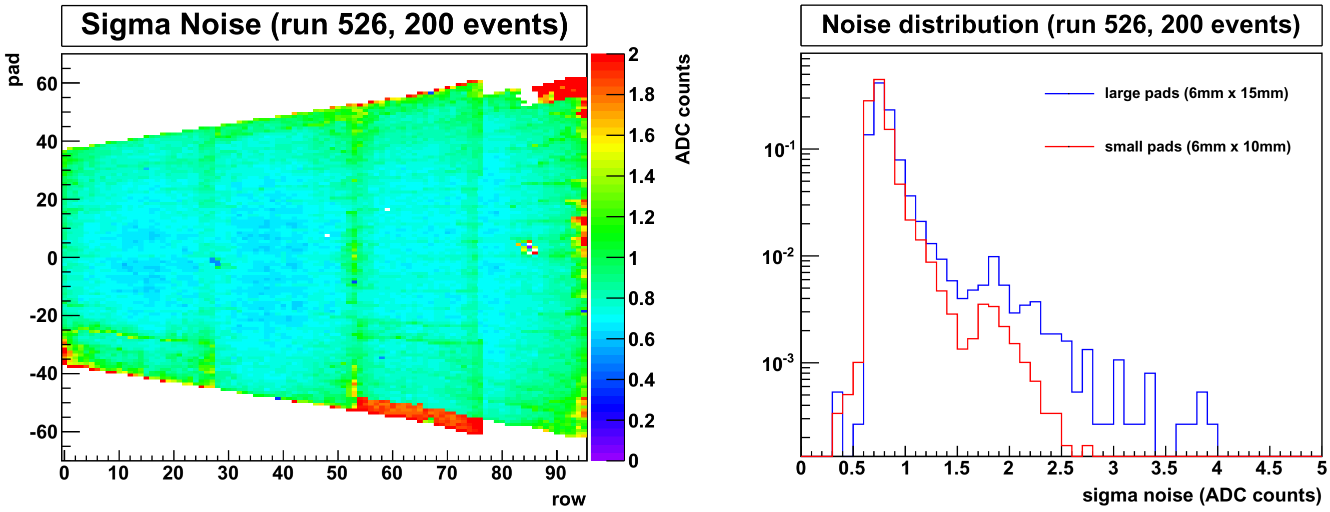

(a) 2-dimenional distribution of the noise.

(b) Noise distribution seperately for both padsizes, normalized to unit integral.

Figure 5.3: Noise in the chamber.

The noise distributions (figure 5.3) show that most channels have an RMS noise below or round 1 ADC count. Despite the fact, that two FECs have a much higher noise, a pattern of the noise is visible with generally higher noise at the edges of the chamber and at the boundaries of the readout partitions. Along the boundary between RP3 and RP4 (rows 53 and 54) the noise is more pronounced than on the other readout partition boundaries. This might be related to the fact that this is also the junction of the different parts of the padplane. The boundaries between single FECs display a slighly higher noise that is attributed to the ribs of the aluminum body. From the innermost partition (RP2) to the outermost partiton (RP5) increasing noise is seen. This can be partly explained by the different PCB track length which leads to a higher capacitance and as a consequence to higher noise. Likewise the different padsizes should lead to different noise values (higher for the larger pads). Figure 5.3(b) seems to confirm this, but the map (figure 5.3(a)) does not display a noticeable change in noise at the padsize boundary (located between row 63 and 64). This leads to the conclusion that the higher noise for the larger pad is not attributed to the padsize.

In the TPC the noise situation was improved by several modifications[7]:

- The noise induced by the LV power supplies (PL512) was reduced by exchaning capacitors and embedding ferrites to the PS. In the test setup an “old-type” LV PS (PL508) is used which did not cause relevant noise during its operation in the clean room.
- The analog grounding scheme of the FECs was changed, some grounding cables have been replaced by thicker ones; some cables have been removed. This was not adopted to the test setup but it seems worth to try this in the future.
- The ground bounce effect caused by simultaneous access of all ALTROs to their memory was reduced by desynchronizing groups of channels to start writing at different clock cycles.

In the test setup three major sources of noise could be identified:

- The readout and control bus connection of the CAMAC crate housing the HV PS induced enormous noise when data was transmitted. Since the readout of the CAMAC is usually done once a second and takes only a very short time this noise is only visible in very few events. To avoid any problems the CAMAC reading was stopped during data taking.

	small pads (6 x 10 mm^2)	large pads (6 x 15 mm^2)	all pads
noise mean (ADC counts)	0.81	0.90	0.85
noise RMS variation (ADC counts)	0.20	0.34	0.26
fraction of channels with noise > 1 ADC count	8%	15%	11%
pedestal mean (ADC counts)	51.1	50.5	50.9
pedestal RMS variation (ADC counts)	9.7	9.5	9.9

Table 5.2: Summary of noise and pedestal properties obtained for the test chamber.

- The ethernet cables connecting the DCS boards to the switch caused high noise when transmitting data. Since data transmission is done in bursts this results in some “noisy events” when the data aquisition is done during such a burst. These events can be identified since they show a characterstic pattern in time with positive and negative (corresponding to the baseline) peaks of almost the same amplitude. Removal of the events did however not lead to a large improvent in the noise situation and had little influence on the results.

- The cooling unit with its circulation pump (running continuously) and vaccum pump, compressor and ventilator (running in diffrent time intervals) couples additional noise to the electronics. This situation could be improved by moving the cooling unit away from the chamber (at present the distance ist only about 1 meter) but requires re-routing of the cooling lines.

The overall performance of the setup with respect to noise seems to be sufficient for the desired measurements. Table 5.2 shows an overwiev over the noise characteristics. The gain measurements were done at the center of the chamber and the center of readout partition 2 to reduce the influence of the noisy edges and corners.

Noise and pedestal values were recorded in a dedicated pedestal run for every measurement with different conditions. One might think that pedestal values could change over time (e. g. due to temperature changes in the FECs) but this was not observed (the FECs were always turned on at least a couple minutes before data taking). The noise and pedestal values also did not show any significant dependence on the anode voltage or gating setttings.

5.3 Calibration pulser data

With the calibration pulser as described in section 3.6.4 reference data were taken to determine the variations in electronic gain and to correct for those variations if required. The pulser was adjusted to deliver signals with a width of 160 μs and a period of 320 μs, the amplitude of these pulses was 900 mV (see figure 5.4). Since the pulser data were taken with a software trigger the pulse frequency of about 3 kHz leads to one pulse in every third event. A total of 300 event ensures sufficient statistics for these studies.[2]

The signals induced on the pads (figure 5.5(a)) are – as expected – in amplitude and integral proportional to the size of the readout pads but have the same shape for both pad sizes. The pad signals have a large main peak (coming from the rise of the pulser signal) followed by a smaller peak and an undershoot in between them (caused by distortions of the pulser signal as seen in section 3.6.4). The main peaks

---

[2] The calibration was later repeated with a pulser frequency of 50kHz for higher statistics, this did not lead to different results.

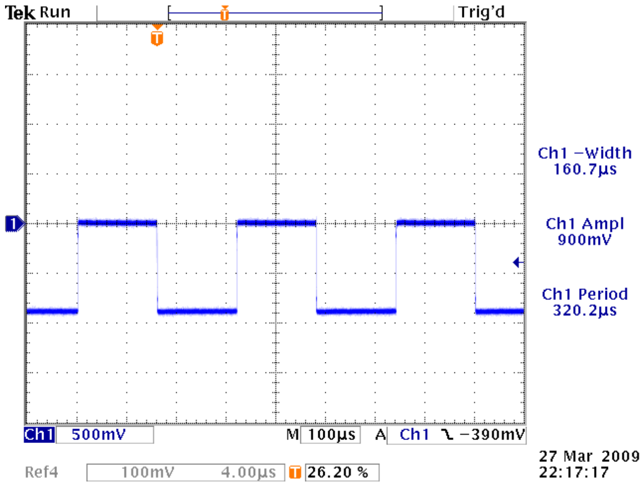

Figure 5.4: Pulser signals fed to the cathode wire grid.

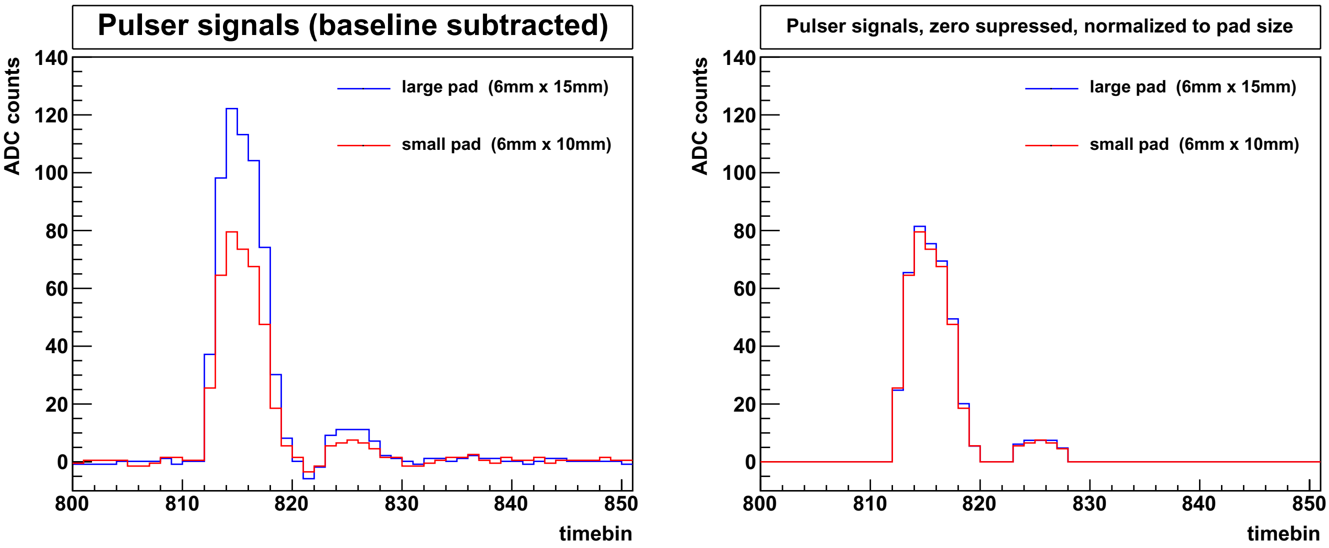

(a) After pedestal subtraction.

(b) After zero-supression and normalization to the pad size.

Figure 5.5: Pulser signals seen by adjacent pads in row 63 (small pad) and row 64 (large pad).

integrated charge is used for the electronics gain equalization[3]. Zero supression and pedestal subtraction is performed prior to the analysis of the pulser data (see figure 5.5(b); the undershoot ensures that the smaller peak is never joined to the main pulse. To extract the gain all the Qtot values for one channel are normalized to the padsize and stored in a histogram. The mean of a fitted gaussian function is further normalized to the global mean resulting in a “calibration factor” describing the gain of one channel relative to the overall mean. The global mean is calculated from the fit of a gaussian distribution likewise.

It should be noted that the setup was changed with reference to the noise and pedestal measurements described in the previous section: two damaged FECs (18 and 19 in RP5) have been replaced; in return two other cards (FEC 19 in RP3 and FEC 7 in RP5) failed. Figure 5.6(a) shows the relative gain for the all channels. Several structures are visible:

- In rows 47, 48 and 95 the electronic gain is much higher compared to the surrounding pads. This is the result of floating anode wires which usually pick up a fraction of the signal.
- Blocks of 16 adjacent pads having almost the same relative gain and depict regions connected to the same PASA and ALTRO chips.
- Apart from large areas were values are missing (due to missing or defective FECs) some single channels have no value: this is caused by channels not (properly) connected to the padplane and single dead channels.
- A substanial variation ($\approx 5\%$) of the gain correlated to the row posistion, but coming in “steps”.

The last point cannot be attributed to manufacturing differences of the electronics. The correlation plot of gain vs. row (figure 5.8) clearly exhibits a structure with different mean values for different row ranges. This structure does not follow the readout partitions, so different supply voltages as well as grounding issues do not seem to be plausible. Most likely the variations seen are related to geometrical imperfections and different wire connections or positions.

Since the aim of the calibration pulser measurements is to equalize differences of the electronics the variation of the signals related to different sources have to be removed. Thus is was decided to calculate the calibration seperately for regions showing a signifcantly different average gain. From figure 5.8 seven different segments, each with an individual number of rows, were identified. The gain was calculated for every segment individually with the procedure described above. The rows 47, 48 and 95 were explictely removed from calculation of the calibration. The result as shown in figures 5.6(b), 5.7(b) and 5.8(b) is much more uniform overall.

Note: The ^{55}Fe source used for the (gas) gain measurements irradiates only a small area of the readout chamber. The different calibration methods described above only lead to differences when comparing measurements done at various source positions.

For the further analysis of the data obtained with the ^{55}Fe source cluster finding was performed with no calibration, the segmented calibration and global calibration to compare the different methods. The calibrations with global resp. segmented normalization are refered to as *global calibration* and *segmented calibration*.

5.4 Measurements with the Fe-55 source

The aim of the measurements is to determine the gas gain without relying on the electronic conversion gain as well as the combined gain of both, gas and electronics. This makes it possible to disentangle

---

[3] The maximal ADC value (Qmax) was tentatively used for calibration and did not lead to different results.

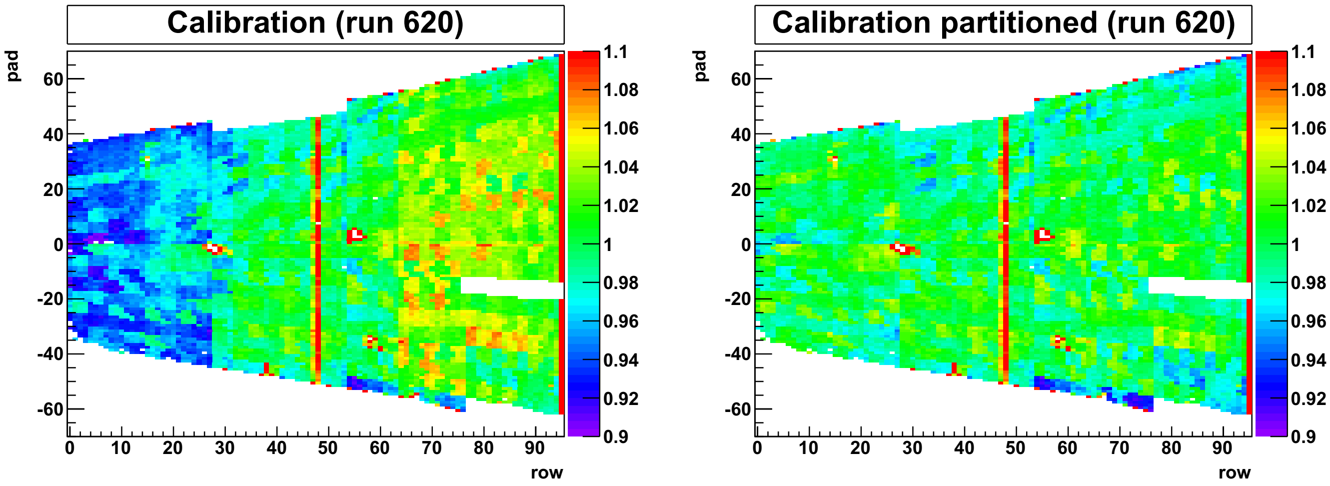

(a) Global normalization: an overall structure with increasing gain to higher row numbers is visible.

(b) Segmented normalization: the overall structure has disappeared.

Figure 5.6: Electronic gain variations obtained from pulser data. Regions of different PASA chips are visible as well as floating anode wires.

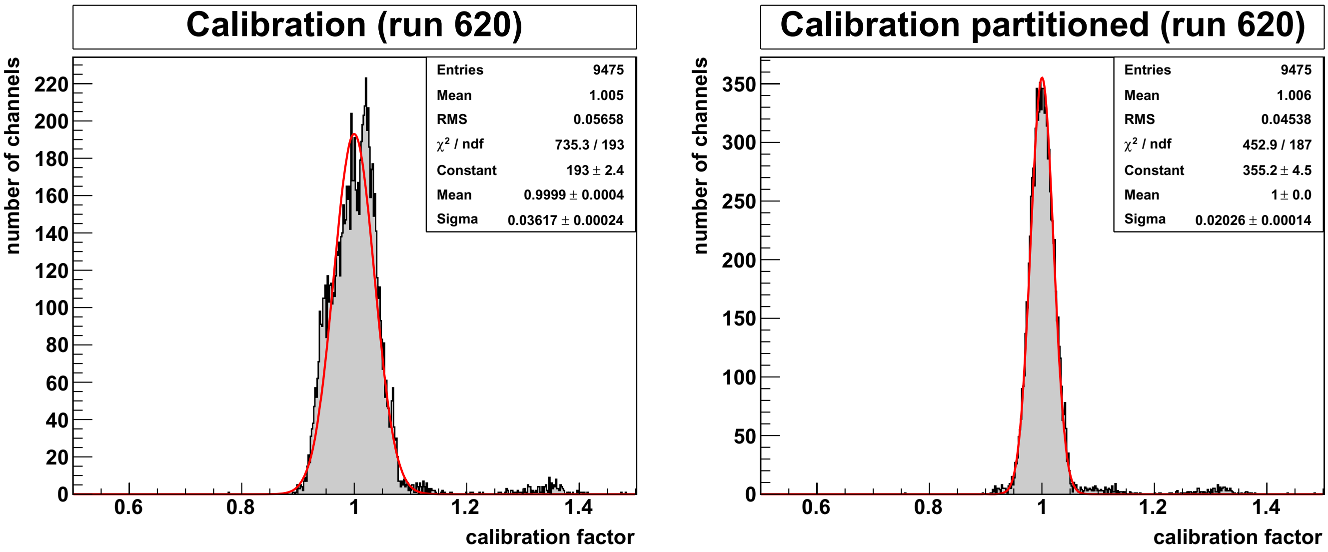

(a) Global normalization.

(b) Segmented normalization.

Figure 5.7: Distriubtion of the relative gain for all channels.

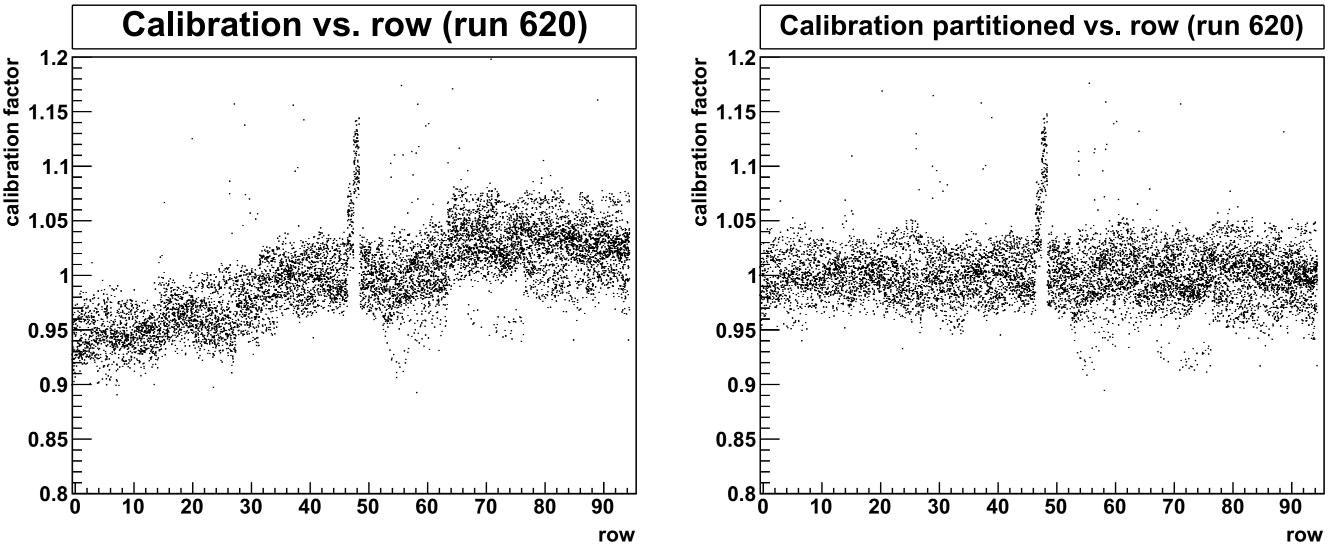

(a) Global normalization.

(b) Segmented normalization.

Figure 5.8: Correlation of the relative gain with respect to the row position of the pad. Regions of different gain are visible as well as the floating wire.

the two signal amplication mechanisms. Variations of the gain with anode and gating voltage, source position and gas density are examined and the data also allow to study characteristics of the electronics.

For the measurements with the X-rays emitted by the iron source only a random trigger can be used, the activity of the source is large enough to produce one (or more) absorbed X-rays in most of the events. The use of a random trigger implies that no information on the position in the drift direction can be extracted from the time of detection. However, the position of the cluster in drift direction is correlated to the distance from the source on the readout plane for geometrical reasons.

Two different source positions are used for almost all (except section 5.4.8) measurements, one being the big hole at the chamber center and the other one located at the center of readout partition 2 (see also figure 3.5 on page 23). From Figure 5.13 the irradiated part of the padplane is apparent. The spot that is irradiated by the source is about 5 cm in diameter (FWHM) for the small holes and 10 cm for the large hole at the center. The source used for the test setup had an activity of 5.5 MBq at the time the measurement producing about 12 kHz of absorbed X-rays for the small holes and 52 kHz for the large hole (see section 5.4.5).

5.4.1 The decay of Fe-55

Iron-55 is unstable and decays with a half life of 2.744 years via electron capture to the ground state of manganese-55 (see figure 5.9). The decay is succeeded by the emission of an Auger electron or characteristic X-ray from ^{55}Mn. The X-rays are mainly from the $K_{\alpha 1}$ and $K_{\alpha 2}$ shells with an energy of 5.9 keV (I=24.4%) and K_β with 6.49 keV (I=2.86%); other lines are negligible.

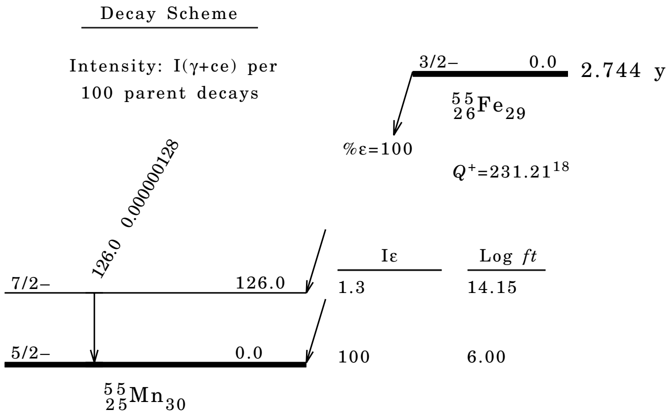

Figure 5.9: Decay scheme for Fe-55. [43]

5.4.2 Method of the gas gain measurement

The method follows the basic idea described in [29] and is based on measuring the currents on the sense wires (with and without an ^{55}Fe source irradiating the chamber) and the absoption rate of X-rays produced by the ^{55}Fe source. The anode current is – in the absence of the source – determined by leakage currents of connectors, HV capacitors, insulation etc. and the charge created inside the active volume by the background radiation (predominantly cosmic rays). With the source the current increases according to product of absorption rate and gas gain.

Thus the gas gain G can be calculated as

$$G = \frac{I - I_0}{e\ rN}$$

where I and I_0 are the sense wire currents with and without source; r is the rate of X-rays absorbed in the active volume of the detector and N is the total number of electron-ion pairs produced on average by each absoped X-ray.

The total number of electrons created was calculated as the average over the different gas components and X-ray energies:

$$N = \frac{\sum_i \alpha_i\ E_i}{\sum_j \alpha_j\ W_j} \approx 167$$

where i denotes the sum over the X-ray energies E_i weighted by their relative intensities α_i and j denotes the sum over the gas components (Ne, CO_2, N_2) with their fraction α_j and the average energy to create on electron-ion pair W_j. The informations on the X-rays are taken from [43], the W values are taken from [44].

It is obvious that this simple approach cannot be true to the full extend; in principle the W values have to be measured for every gas mixture [45]. The gain was measured at different anode voltages up to 1650 V and different positions of the source.

5.4.3 Anode current

The anode current is measured with the HV PS (iseg CHQ 222M) as described in section 3.6.3 and recorded with a PC. The current measurement has a resolution (not accuracy) of 0.1 nA though the

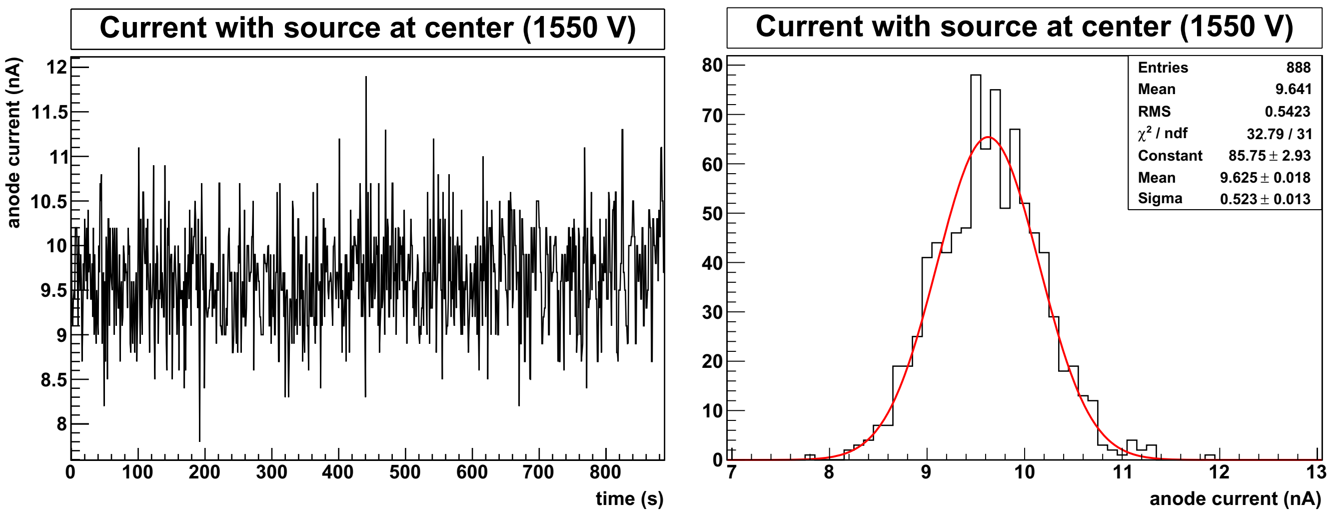

(a) Variations of the current over time.

(b) Histogram to determine the mean current.

Figure 5.10: Examples of the sense wire currents measured with the iseg HV PS.

measured current shows huge fluctuations. Figure 5.10(a) shows an example of a current measured with this method. The current is measured over a time of typically 5 to 15 minutes with a rate of 1 Hz (to achive statistical uncertainties below 1%) and averaged over this time (See figure 5.10(b)). The error of current measurement claimed by the manfacturer is ≈ 5 nA [46] in the required range, this would not be sufficient to determine the gain at the small holes where the current difference is of the order of a few nA. For the analyis an accuracy of 0.1 nA was assumed. A large uncertainty remaines (especially for the measurements at the small holes and/or low anode voltages) which also gives the major contribution to the gain uncertainty. The noise superimposed to the current measurement is not white, i. e. it has a stronger component at lower frequencies. Besides that current variations on long timescales are caused by variations of the gas gain with temperature and pressure variations. The leak current of other compontents (HV capacitors) also shows some change over time.

The currents are always measured with and without the source, the difference in currents is directly proportional to the gas gain. To minimize systematical errors due to leak current variations it is preferable to perform both measurements within a short time. This requires to remove and put back the source between anode voltage changes, which could lead to a different aborption rate (due to slightly different source positions). The gain at the chamber center was measured with this procedure. For the gain measurement at RP2 data has first been taken with the source and lowering the voltage down to 1150 V and afterwards without source and rising the voltage to 1600 V.

5.4.4 Fe-55 signals and clusters

The electrons created in the chamber by absorption of X-rays (from ^{55}Fe decays) drift to the amplification region where they are amplified by avalanche creation at the anode wire and induce signals on the cathode pads. The range of the primary electrons is about 1.5 mm in the gas mixture (calculated from [45]), the diffusion of the electron cloud during the drift is in the same range. The observed spread over pads and rows is a convolution of the primary range, the diffusion and the pad response function.

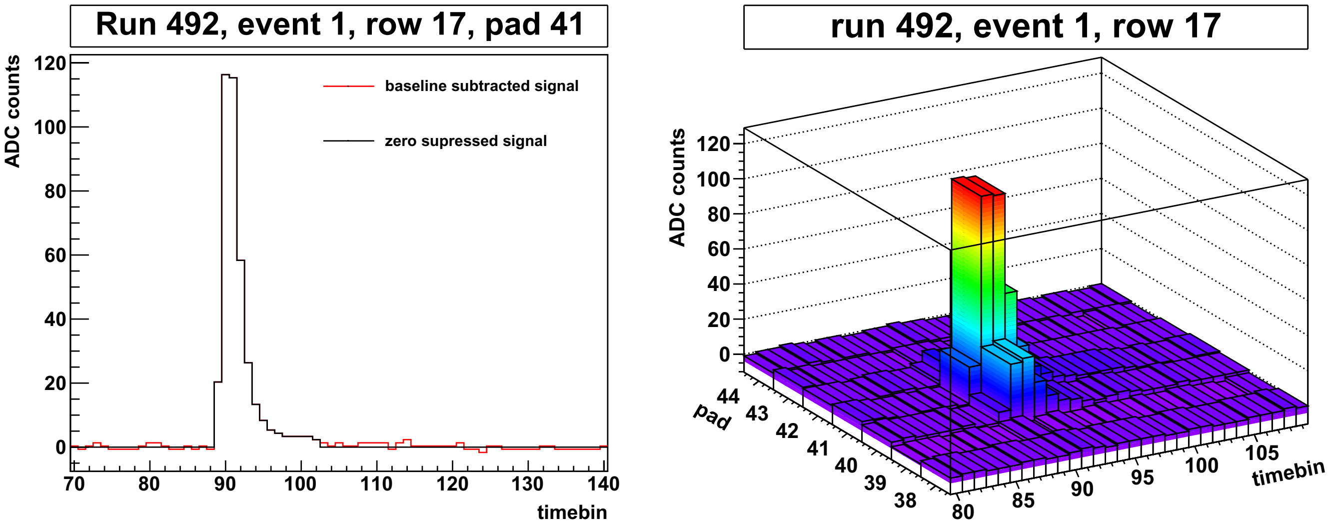

(a) Single pad.

(b) Section of one row, non zero-supressed data.

Figure 5.11: Signals on the pads from ^{55}Fe X-rays.

The total (integrated) signal is ADC counts on the padplane from one absorbed X-ray releasing a number n_e of primary electrons in the gas is

$$Q = n_e \cdot G \cdot a \cdot c \cdot G_c$$

where G is the amplification factor (gas gain), a describes the loss of electrons (electron attachment during drift, electrons captures by gating or cathode wires), c is the signal coupling to the pads and G_c is the conversion gain of the electronics (in ADC/fC). The relation is a description of the average values assuming G, a, c, G_c are all independent of n_e. This assumption implies in particular the linearity of electron amplification (no space-charge effects) and linearity of the electronics signal processing.

All contributions to Q are subject to statistical variations, which can be described by a gaussian distribution around the average value with a standard deviation σ. Assuming independence of all contributions the width of the resulting Q distribution is

$$\sigma_Q = \sqrt{\sigma_{n_e}^2 + \sigma_G^2 + \sigma_a^2 + \sigma_c^2 + \sigma_{G_c}^2}.$$

In addition there are local variations for different pads/channels and noise picked up by the pads leading to a further broadening of the Q distribution. The width spatial distribution of the Q over the pads and rows is characterized by the pad response function, the range of primary electrons and diffusion.

The Qtot value is calculated as the sum of all pads and timebins of the signal created by an absorped X-ray which are above a given threshold. This threshold is indispensable to remove at least part of the noise. Thus the Qtot value represents only a fraction of the full signal with the value of this fraction depending on the threshold and the pulse amplitude. The Qmax value is the maximal height of the signal integrated over one pad and one timebin. For a constant shape of the signal $Qmax$ contains on average always the same fraction of Q.

Figure 5.11 show signals from the ^{55}Fe X-rays for a single (a) and adjacent pads in a row (b). For the further analysis cluster-finding is performed on the zero-supressed and baseline-subtracted data. If a calibration is applied it is done after the zero-supression and prior to cluster finding. The cluster finding algorithm as described in section 4.2 looks for local maxima in all three dimensions (row, pad and timebin) and extends the cluster in all dimensions until it either end up at zero (corresponding to

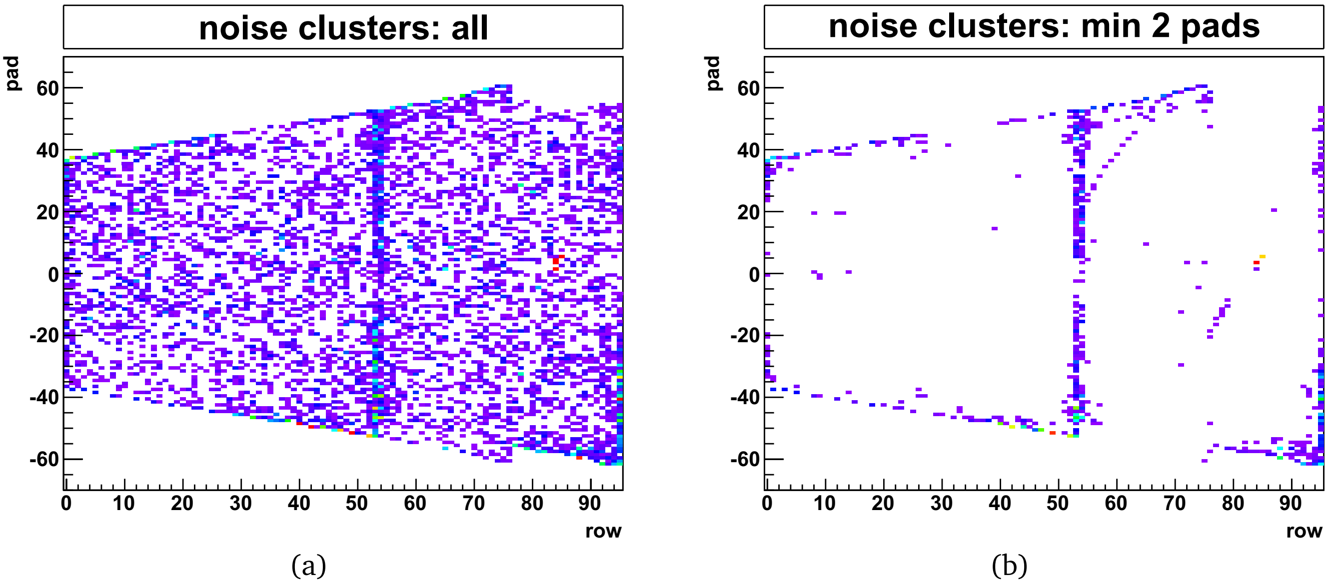

(a)

(b)

Figure 5.12: Distribution of clusters reconstructed from noise. The requirement to have the cluster spread over at least over two pads removes ≈ 90% of the noise.

a signal below zero-supression threshold) or encounters a larger signal. For the signal of each channel in time a "glitch rejection" is performed allowing one timebin to have a lower value then the adjacent timebins while still being assigned to the same cluster. The various properties that are calculated and stored are described in section 4.2.

It is a characteristic of the cluster finder that every signal above threshold is assigned to (at least) one cluster with the integrated charge of one event beeing equal to the Qmax sum over all clusters. With the adopted zero-supression threshold of $3\sigma_{\text{noise}}$ many clusters are reconstructed that are pure noise. These noise clusters predominantly have only a single channel contributing and low Qtot and Qmax values making it easy to cut them out. Figure 5.12 shows reconstructed clusters from "black" events (no source), the requirement to have two pads in a row contributing is used throughout the analysis of the clusters. As apparent from figure 5.12 the noise is concentrated at the edges of the chamber and in rows 53-54. The noise in the rows 53-54 is particularly problematic since it coincides with the large hole at the chamber center. This is the only spot where the currents can be measured quite precicely (the absorption rate and thus the currents are larger by a factor of five compared to the small holes).

Cutting out the noise with the requirements to have more than one pad contributing and a Qmax threshold of half the peak position yields the 2-dimensional spatial distribution displayed in figure 5.13 for the two source positions. This distribution is well described by a 2-dimensional gaussian distribution. The peak position together with the standard deviation of the distribution can be used to remove all clusters that are located far away from the source position and thus likely to be noise. This was done for part of the analysis (chamber center) with a 4σ cut.

The spectra of Qmax and Qtot (see figures 5.14 and 5.15 show, as expected, an approximately exponential decrease of the noise. It seems obvious to cut on the clusters Qmax and/or Qtot values for seperation of the noise. To determine the number of clusters different methods with different cuts have been used (see next section). The presence of the iron source produces more clusters with low charge (this is visible from figure 5.16). Most of these additional clusters are an artifact of the cluster finding algorithm which might split a cluster into parts if is recognizes multiple local maxima (caused by fluctuations of the signal or inapplicable calibration values) or caused by signals that are only partly recorded/evaluated because

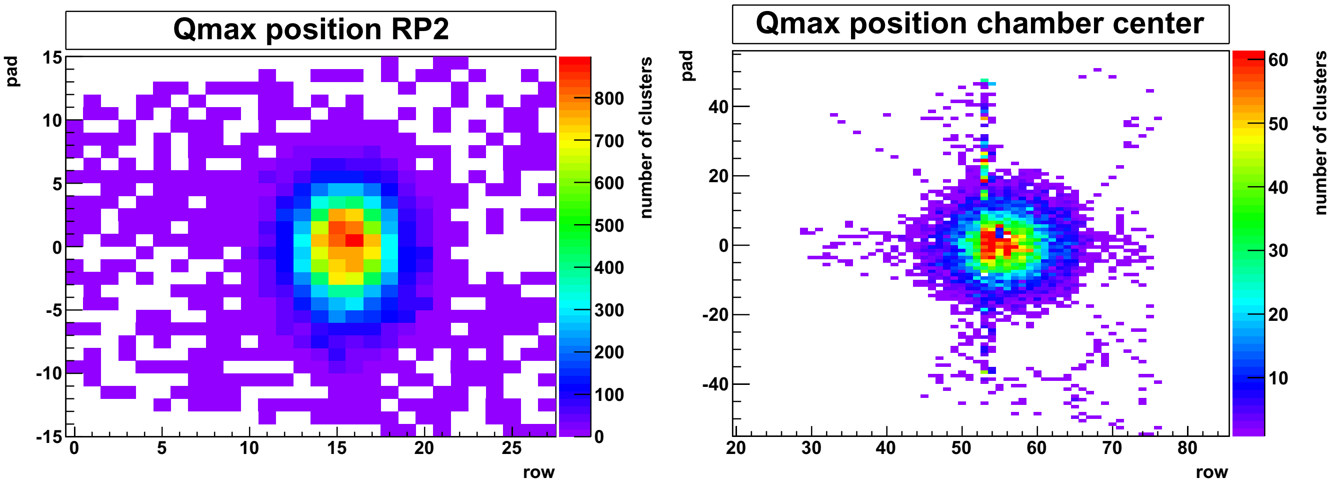

(a) (b)

Figure 5.13: Distribution of the positions of absorbed X-rays from the Qmax position for readout partition 2 (a) and the cente spot (b). Only Qmax values above a given threshold are regarded.

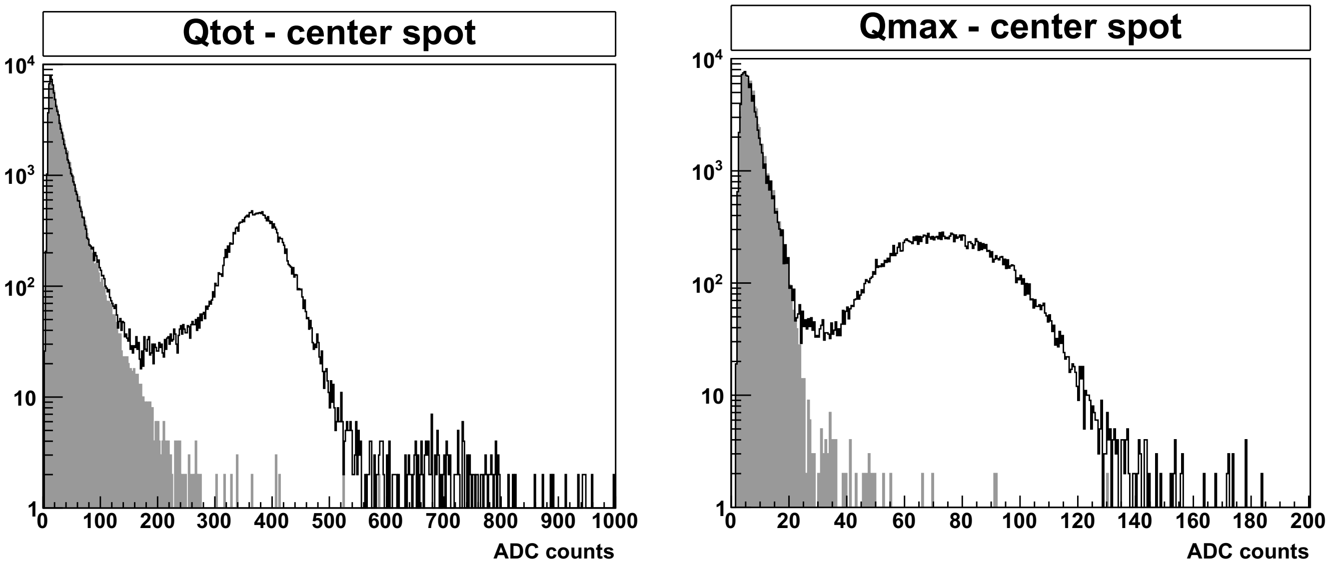

(a) (b)

Figure 5.14: Comparison of Qtot (a) and Qmax (b) spectra. The grey filled area shows the noise/background (taken without source) the black line is the data obtained with source. The anode voltage was 1550 V and the segmented calibration is used.

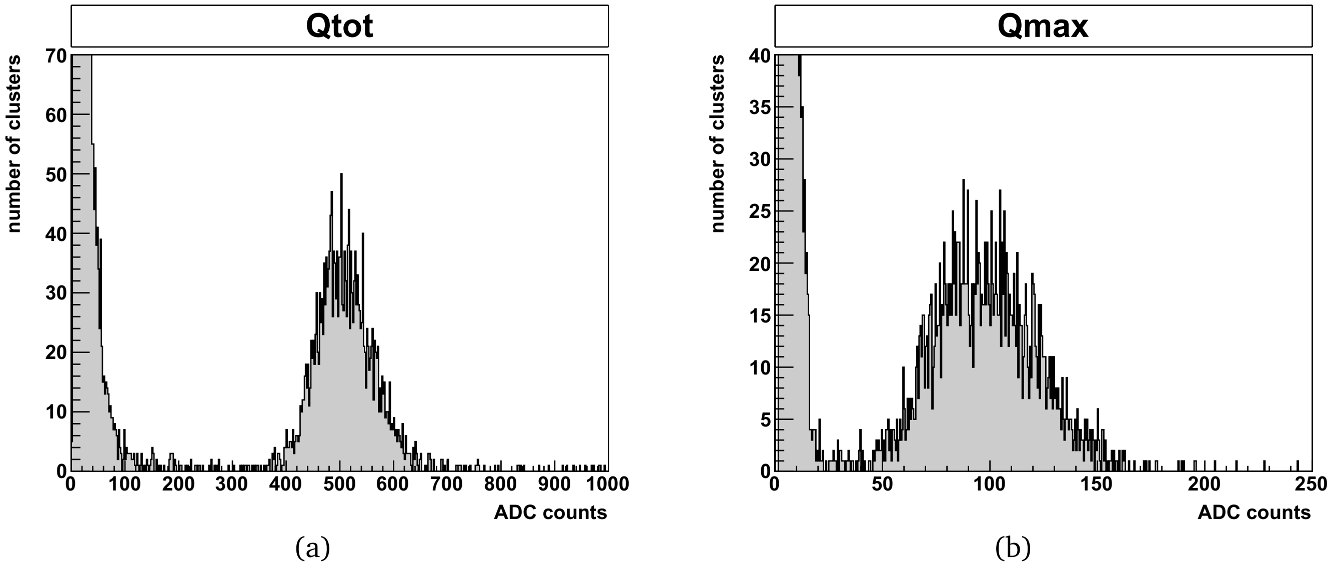

(a) (b)

Figure 5.15: Qtot (a) and Qmax (b) spectra taken with high gain (anode voltage 1600 V) at RP2 without any cuts. The ^{55}Fe peaks are clearly seperated from the noise.

they are located next to channels removed from the analysis (defective or very noisy channels) or are cut-off by the readout window. These effects can be removed in a large part by cuts on the clusters properties, the resulting correlation of Qmax and Qtot contains clusters extending continously to low Qmax/Qtot values (with the source). It seems reasonable to attribute these clusters to X-rays absorbed in the central electrode (electrons enter the drift region with less energy) or in the amplification region (not all produced electrons are fully amplified).

To determine the cuts it is useful to look at the correlation of various cluster properties. Besides the correlations between Qmax, Qtot and the number of pads (shown in figures 5.16 and 5.17) the correlation between Qtot/Qmax and the distance from the source turned out to be very useful. To separate the noise one can either cut on Qmax or Qtot or both. An easy to implement way is to cut on Qtot in a way that all clusters below half of the peak position are removed. This cut was used as a standard cut in the further analysis.

The correlation of Qmax/Qtot with the number of pads (see figure 5.17) reveals that most ^{55}Fe clusters have 4-6 pads contributing while the noise extends from single pads (not seen on the plot) to large number of pads (more than 10). The Qmax value is not correlated to the number of pads, the Qtot shows some increase. The strong noise seen at the border of the readout partitions (see also figure 5.12(b)) accounts for more than 98% of the noise clusters. This problem is only present for measurements at the center spot, additionally there are more dead channels in this region (cf. figure 5.6). At RP2 the noise is lower and thus the rate of aborbed X-rays (next section) and peak positions can be determined more accurately but the anode currents are small and measured less precise.

With a cut on the Qtot (half of the peak position – as described above) the ^{55}Fe clusters are selected; the spread of clusters observed is shown in figure 5.18. These distributions are very similar all over the chamber and show that most clusters extend over three pads in the pad direction and two rows. This, along with the information of the signal duration, can also be used as an effective way to cut out the noise.

To compare the calibration methods these cuts were used, along with a cut on Qmax. The resulting Qtot and Qmax distributions for (segmented) calibration and uncalibrated data are shown in figure 5.19. The

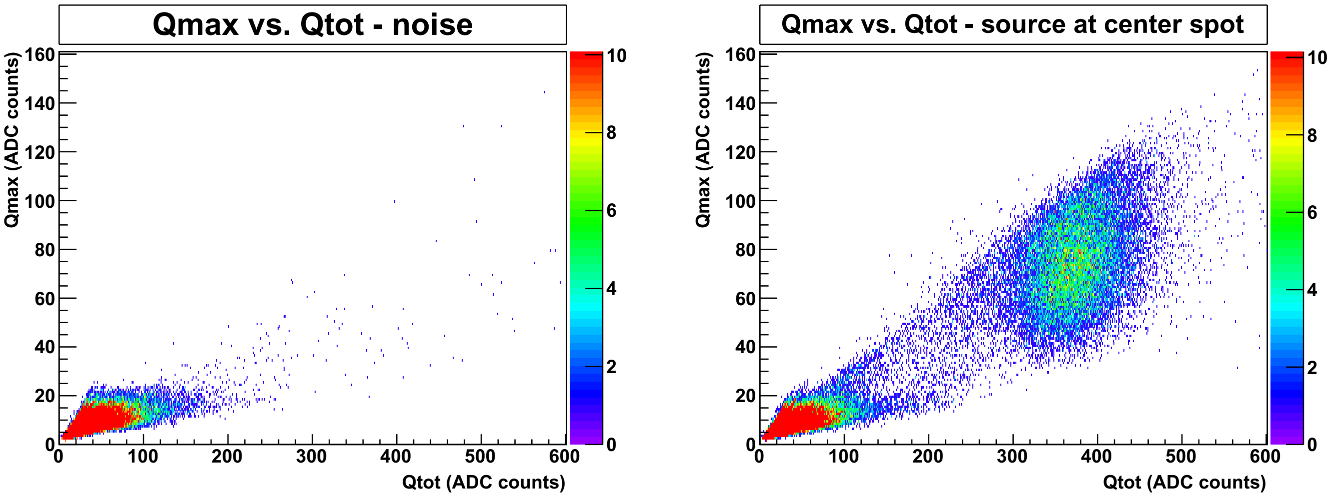

(a) Without source.

(b) With source.

Figure 5.16: Correlation of the Qmax and Qtot values for clusters around the center spot (RP4 and RP5). Clusters with signals in only one pad are omitted.

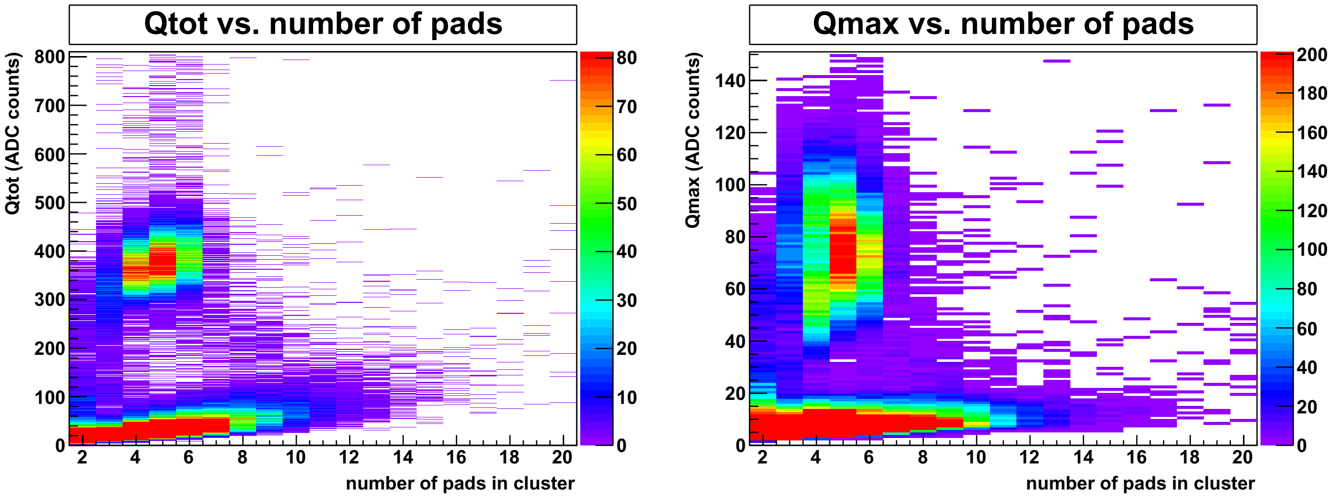

(a)

(b)

Figure 5.17: Correlation of Qtot (a) and Qmax (b) with the number of pads in the cluster.

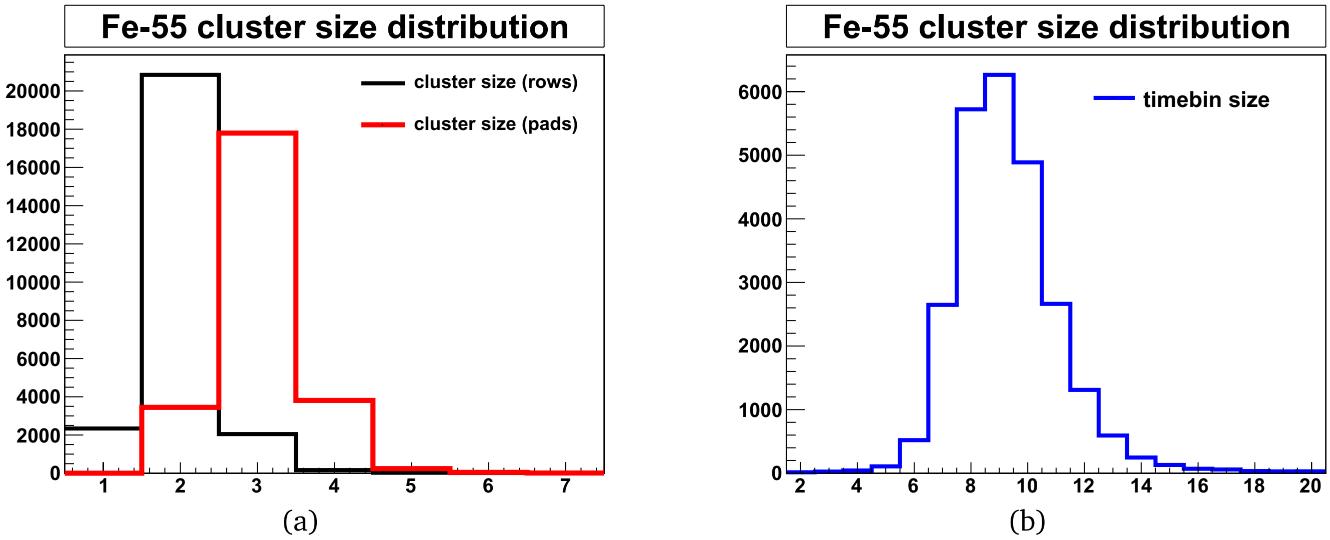

Figure 5.18: Cluster size distribution in pad and row (a) as well as time (b) dimension (at chamber center). The noise clusters are removed.

data were taken at RP2 to remove the influence of the noise and allow an inspection of the peak width which was expected to more narrow with the proper calibration. However the effect of the calibration is too small (local variations $\approx$ 5%) compared to the the peak width (Qmax FWHM about 50%) to be visible in the spectra. The calibration with global normalization only differs in the peak position from the segmented calibration.

At the chamber center (corresponding to rows 45-65) there is almost no difference between the two calibration methods and the uncalibrated data, except for the pads close to the floating wire. For the further analysis the segmented calibration was used for the data at RP2 and no calibration was used for the measurements at the chamber center. In the course of the gain calculation the different calibration methods are compared once more, incorporating the results from the anode current measurements.

5.4.5 Rate of absorbed X-rays

While the cathode current can be measured directly and quite precise the rate of absorped X-rays is somewhat more diffcult to obtain.

The rate of absorbed X-rays can be determined in two ways, using the anode or pad signals:

- For an exclusive measurement of the gas gain it is in principle also possible to determine the rate from the signals created on the anode wires, this method was employed in the course of post-production test of the ROCs[29].

  The signals created on one partition of the sense wires are amplified with a charge sensitive preamplifier (connected to the wires through a capacitor) located as close as possible at the detector (approximately 10 cm away) the output is shaped and amplified by a timing amplifier (NIM standard), with a discrimminator and a counter unit is is possible to count the absorped X-rays. However the gas gain for this method has to be very high to get an acceptable signal-to-noise ratio.

  During the assembly of the test setup this method was intended (cf. section 3.4.2) as a comparative measurement of the gas gain not depending on the electronics. But it turned out that the achieved

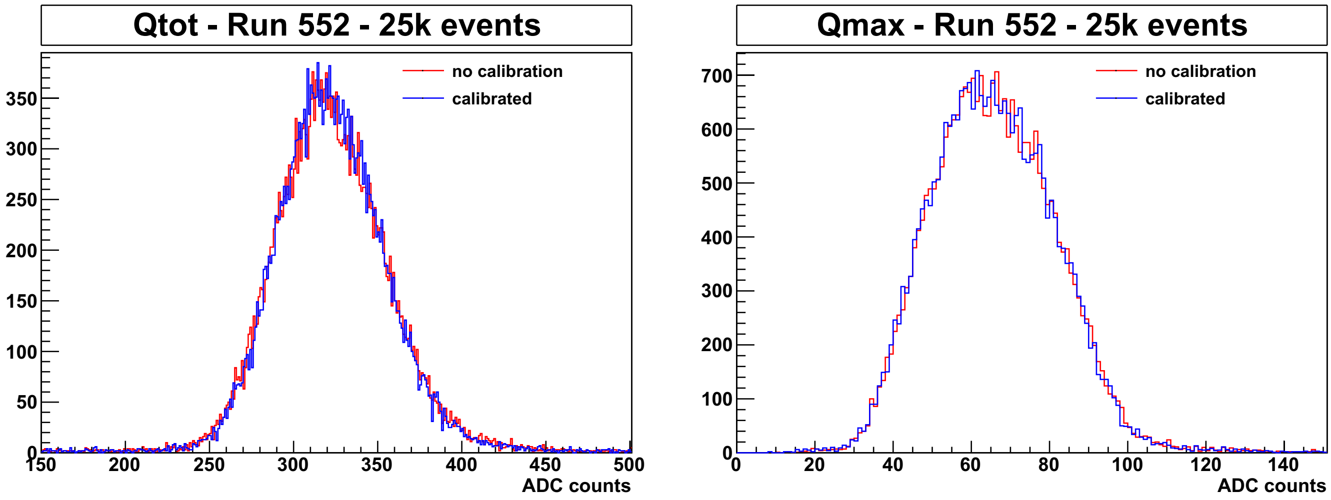

(a) qtot

(b) qmax

Figure 5.19: Comparison of the (segmented) calibration and uncalibrated data taken with high statistics at RP2 (anode voltage 1550 V).

SNR (at anode voltages up to 1650 V) did not allow to discriminate the ^{55}Fe signals from the noise [4]

- The second method is to take the signals read out from the pads and look for clusters caused by absorbed ^{55}Fe X-rays. Applying appropriate cuts on the cluster properties it is possible to deduct the absorption rate. This method was employed for the gain measurements and is described below.

With the trivial assumption that the rate of absorption does not depend on the anode voltage is sufficient to determine this rate once at a high gain where it is easier to discrimminate between noise and “real” signals. But, as pointed out above, the anode current has to be measured also with the source removed making it necessary to remove the source between measurements at different voltages. The position of the source is thus never exactly the same resulting in a slightly different absorption rate.

Three different methods of calculating the absorption rates are employed. Figure 5.20 gives a compilation of the values obtained with different methods and gains for the source at RP2 and chamber center.

For low gains (accordingly low anode voltages) the different methods result in considerable different rates, while at high gains the rates are more consistent though they still display systematic differences. This is at least true for the values from RP2; at the chamber center the higher noise causes larger fluctuations. The rates used to determine the gain are $r_{\mathrm{RP2}} = (11.8 \pm 0.2)$ kHz respectively $r_{\mathrm{center}} = (52 \pm 2)$ kHz and are chosen to reflect the range of values from different methods. As intuitively expected these rates do not depend on the chosen calibration.

Event counting

The most simple way to determine the number of absorbed ^{55}Fe X-rays is to look at the total charge (accumulated over all pads and measured in ADC units) in every event. Since the number of absorbed

---

[4] If the gain is large enough this becomes possible and it was done during first tests of the chamber (with a Ne-CO$_2$ gas mixture at 1500 V) leading to the incident described in appendix A.

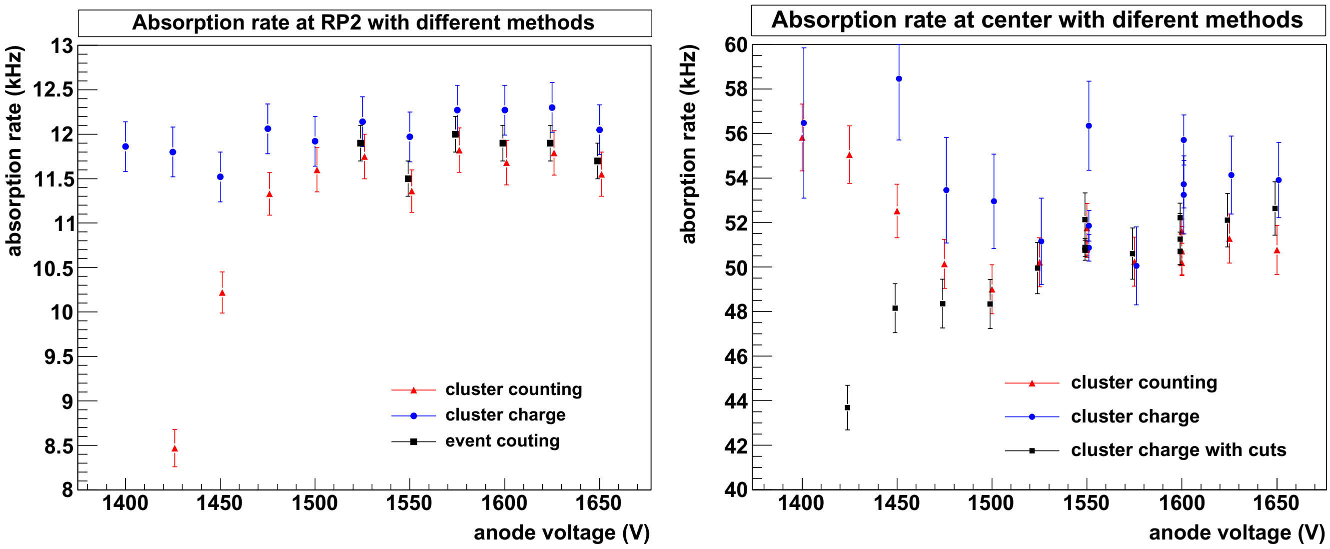

(a) Small hole at RP2: the absorption rate is approximately 12 kHz.

(b) Large hole at chamber center: approx. 52 kHz.

Figure 5.20: Illustration of different methods (described in the text) to determine the absorption rates. At higher gains the results are fairly consitent. The errorbars reflect only statistical uncertainties.

photons is always an integer the total charge spectrum should show peaks for 1, 2, 3, ... absorbed photons with a seperation according to the charge created by one X-ray. Figure 5.21 shows the spectrum for different gains (= anode voltages). The number of aborped X-rays per event n is completely random and thus follows a Poisson distribution around the mean value $r\tau$:

$$P_\tau(n) = \frac{(r\tau)^n}{n!} \cdot e^{-r\tau}$$

where r is the absorption rate and $\tau = 100\ \mu$s is the time of one event, calculated as number of timebins times the sampling rate.

The rates calculated with this method (figure 5.20(a)) for different gains show no significant dependenance on the gain. Combining the measurements with different anode voltages (1525 V to 1650 V) the absorption rate for the source at RP2 was estimated to $r = (11.82 \pm 0.09)\ 10^3\ \mathrm{s}^{-1}$ by χ^2 minimization. It matches well with the rate obtained from cluster analysis (see below). The observed frequencies for three or more absorbed X-rays were grouped together in one class, still a systematically higher frequency for larger numbers was observed. The peak-to-peak distance agrees well with the position of the peak in the QMax spectra.

The method described above has the advantage that is does not depend on the details of the cluster finding algorithm or cuts on the clusters properties but it is only applicable for high gains where the contributions from different numbers of absorbed X-rays are clearly seperated. Similarly the noise background has to be sufficiently low, which is not the case at the chamber center and thus this method could only be used for RP2. Comparison of the results to the other methods (which are relying on the cluster data) gives a useful verification and benchmark of these methods.

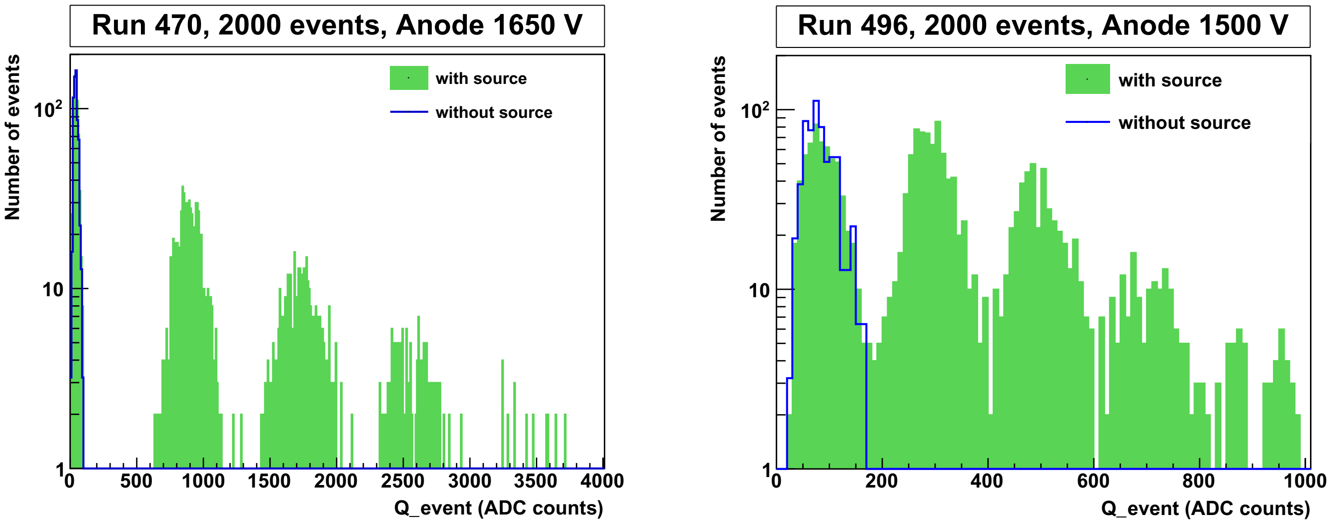

(a) High gain: contributions from different numbers of absorbed X-rays are clearly separated.

(b) Low gain.

Figure 5.21: Distribution of total (integrated) charge of events measured at RP2 with different anode voltages. The Notice the logarithmic y scale and different x ranges.

Cluster counting

A different method is to impose appropriate cuts on the cluster properties to extract the clusters caused by absorped X-rays from the background (see also section 5.4.4) and count them. It is apparent from figure 5.15 that the most simple way is a cut on the clusters Qtot which has to be adjusted for every voltage. Since the iron peak is easily identified the cut was done halfway between this peak and the background peak. To remove the background the reconstructed clusters from runs without source were counted in the same manner. The difference remaining directly yields the absorption rate.

The best overall-fit value with this method is $r = (11.61 \pm 0.07)\ 10^3\ \mathrm{s}^{-1}$ for RP2, where the given uncertainty is coming only from statistics (systematical effects are not considered).

With a different, more generic cut (signal in more than one pad, distance from source smaller than 4σ and Qmax of the cluster larger than 20 ADC counts) the rate was $r = (11.65 \pm 0.10)\ 10^3\ \mathrm{s}^{-1}$, where the larger uncertainty is caused by less runs that could be used (1400 V – 1650 V).

While for high gains (high anode voltages) the calculated rates are found to be constant (for both source positions) lower gains resulted in an increase of the rate for the chamber center and a decrease for RP2 (see figure 5.20(a)). This behavior can be explained by the difference noise situation. With lower gain the Qtot peaks (and thus the cut position) is shifted to lower values. For RP2 where the noise is low this results in cutting out the lower tail of the iron peak and thus gives a lower rate. For the chamber center this effect is overcome by noise clusters above the cut, yielding a higher rate.

Cluster charge

As stated before the presence of the source also produces more clusters with low Qtot. Similarly, the total charge of a single event which contains no absorbed X-ray is (on average) increased compared to an event which was recorded without source. This increase is about 2% of the charge created by one absorbed X-ray and most likely caused by X-rays aborbed in the central electrode Mylar foil or in the amplification region. The measured gain can be corrected for this additional charge by replacing the absorption rate with an effective absorption rate, approximately 0.2 kHz larger for the source at RP2.

For a more accurate calculation of this effective rate the integrated charge of all clusters was calculated for events with and without source. The difference is then divided by the mean charge created by one fully absorbed X-ray (peak position of Qtot). To reduce the noise clusters with only a single pad contributing were omitted. The results for RP2 (as shown in figure 5.20(a)) are almost independent of the gain and the resulting best-fit using all values is $r = (12.01 \pm 0.09)\ 10^3\ \mathrm{s}^{-1}$.

For the chamber center with the increased noise this method leads to stronger fluctuation with larger errors (due to the larger background). Thus the rate calculation was repeated with additional cuts on the clusters (this is labeled *cluster charge with cuts* in figure 5.20(a)). These cuts were chosen to remove nearly all the noise and are made up of the following requirements: more than one pad, more than three timebins, distance from source smaller than 4σ and Qmax larger than 20 ADC counts. These selection criteria were applied for all voltages leading to a drop in the calculated rates for low gains.

5.4.6 Gas gain

The absorption rates $r_{RP2} = (11.8 \pm 0.2)\ 10^3\ \mathrm{s}^{-1}$ resp. $r_{center} = (52 \pm 2)\ 10^3\ \mathrm{s}^{-1}$ with 167 released electrons per absorbed X-ray leads to an average charge creation rates $\dot{Q}_{RP2} = (316 \pm 6)\ \mathrm{fC\ s}^{-1}$ and $\dot{Q}_{center} = (1.39 \pm 0.06)\ \mathrm{pC\ s}^{-1}$. The gain was calculated from these rates and the measured currents according to 5.4.2. The errors of the absorption rates and number of electrons created lead to a systematical deviation of all measured values for the gas gain. They are therefore not present in the following plots.

The gaincurves for the two spots of the chamber are shown in figure 5.22. Note that the conditions (pressure, temperature) were quite different. For both measurements the gain has an approximately exponential dependance on the voltage. A fit of an exponential function $G(U) = k \cdot 2^{U/U_2}$ to the data points above 1450 V yields the same slope with $U_2 = 76$ V, i. e. the gain doubles when increasing the anode voltage by 76 V. The constant k is about 15% larger for the center spot reflecting the difference in gain.

With increasing gain the pulse amplitude ($\widehat{=}$ Qmax) and integral ($\widehat{=}$ Qtot) increases. The plots of the peak positions of Qtot and Qmax versus gain (Figures 5.23 and 5.24) allow the assumption of a linear dependence, i.e. a linear response of the electronics. From the values for the chamber center (figure 5.24(b)) the Qmax dependence complies with the proportional relation

$$Q_{\mathrm{max}}(G) = 0.01516(9) \cdot G$$

where the constant is determined by a fit to the data assuming proportionality. The Qtot peak position also displays a linear dependance on the gain (figure 5.24(a)). For RP2 (figure 5.23) Qmax and Qtot peak positions were calculated from both the uncalibrated data (segmented calibration is not different) and using global calibration and are plotted along with the fits from the chamber center. The low accuracy of the gain measurement does not allow to rule out one of the calibrations, they are both compatible with the data from the center spot (where the different calibrations do not lead to significant differences).

The linear relation of both Qmax and Qtot would imply also a linear dependence between them. Figure 5.25(a) shows the correlation between Qmax and Qtot for all measurements including the different calibrations for RP2. As expected, the calibration changes Qmax and Qtot by the same factor not leading

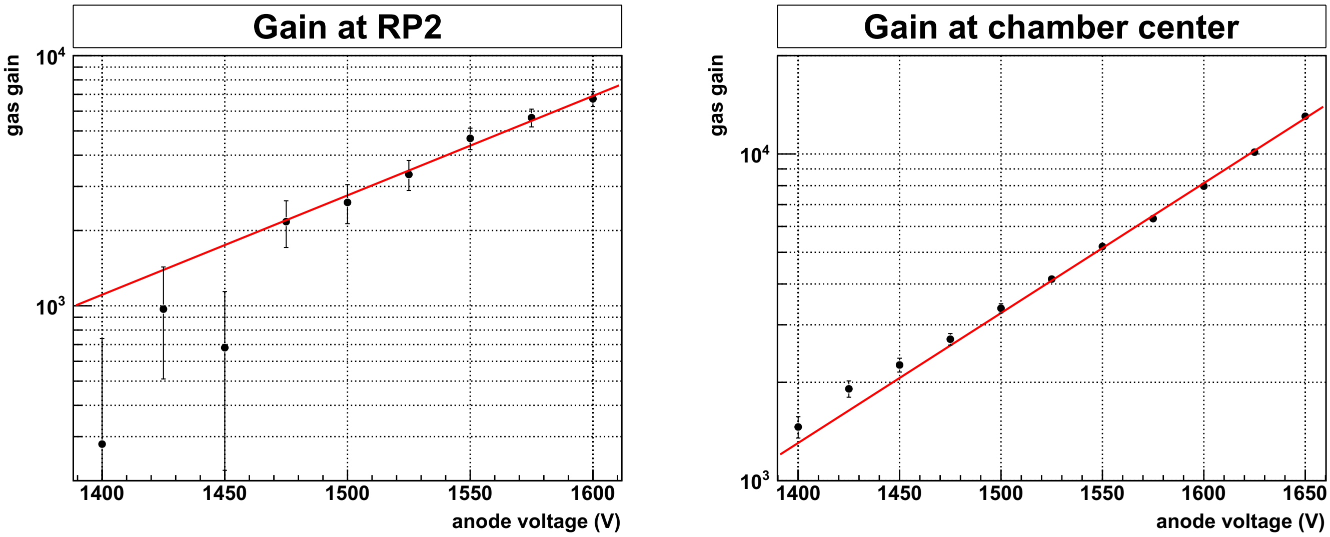

(a) (b)

Figure 5.22: The gas gains calculated from anode currents and absorption rates. The line is an exponential fit to the data omitting the data points with anode voltages 1400 V to 1450 V. The errorbars only contain uncertainties of the current measurement.

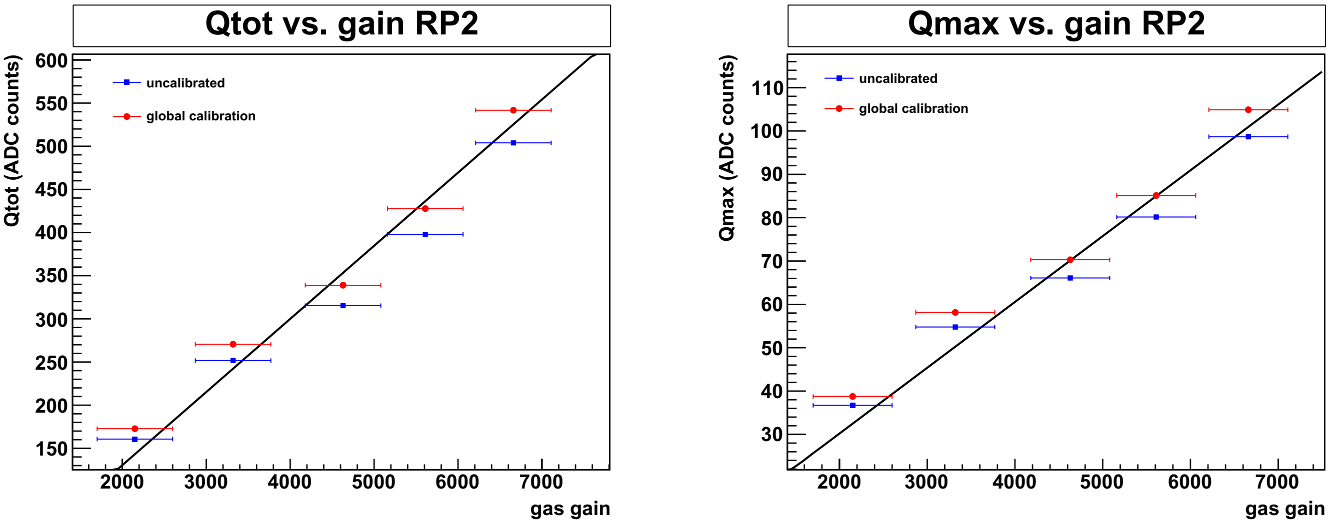

(a) (b)

Figure 5.23: Qtot (a) and Qmax (b) peak positions as a function of the gas gain at RP2 comparing the effects of the calibration. The solid lines represent the relation expected from the measurements at the center spot (figure 5.24).

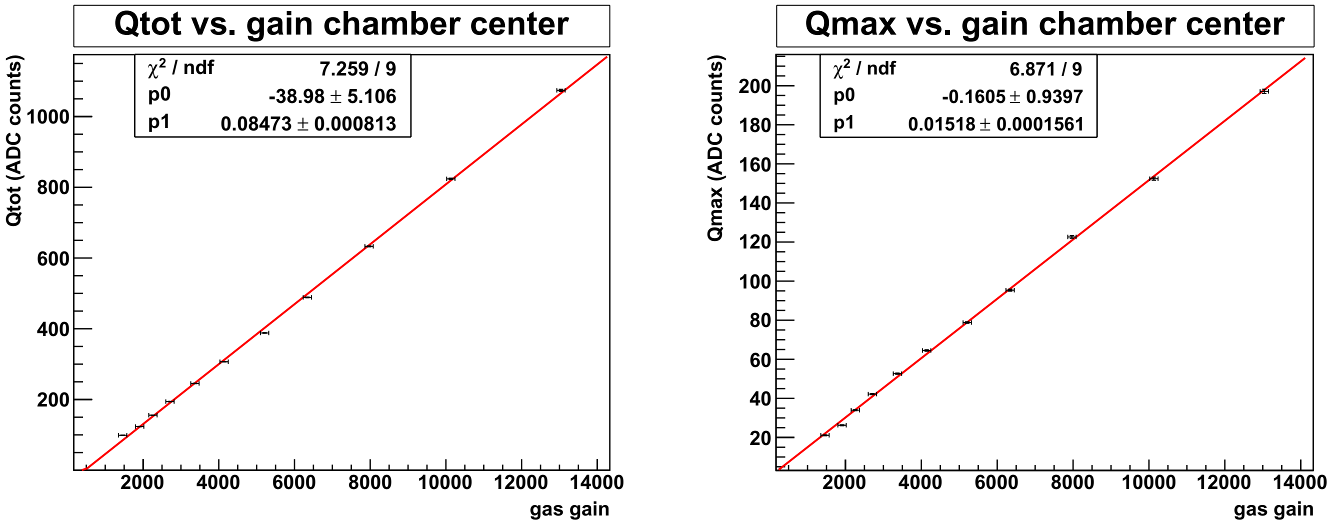

(a) (b)

Figure 5.24: Qtot (a) and Qmax (b) peak positions for the chamber center. The lines are linear function fits to the data.

to a different relation between them. The relation between Qmax and Qtot is however not linear, this is indicated in the plot by two lines representing fits to the low Qtot and large Qtot values respectively. The Qmax value, which is the integral signal of one pad, one row and one timebin, always contains the same fraction of the total signal. In figures 5.23 and 5.24 this nonlinearity is masked by the large gain uncertainties. The Qtot values rise faster than Qmax since the fraction of the signal that is detected depends on the pulse height. As a result of the zero-supression procedure Qtot does not contain the full signal but only the part (in time, row and pad) that is above a given and fixed threshold. The ratio Qtot/Qmax quantifies the fraction of the signal incorporated in the Qtot value. As shown in figure 5.25 this ratio rises with increasing Qmax (or equivalently increasing gain) and exhibits evidence of saturation for larger Qmax values, for high gains it should approach the full charge of the cluster.

5.4.7 Energy Resolution

The energy resolution R of a detector is defined as [47]

$$R = \frac{\mathrm{FWHM}}{\mathrm{Mean}} = \frac{2.35\sigma}{\mu}$$

where the latter part assumes a gaussian distribution around a mean value μ with a standard deviaton σ. This was used to determine the energy resolution for the 5.9 keV X-rays. After application of the cuts to remove the noise (more than one pad, Qtot $> 0.5\mu_{\mathrm{Qtot}}$) mean and width are obtained from the fit of gaussian distribution to the data of the all remaining clusters. The resolution was determined for both source positions using the Qmax and Qtot values of the clusters and is shown in figure 5.26 as a function of Qmax. As pointed out above Qmax can be regarded as a measure of the gain.

The resolution approaches about 25% for Qtot and 60% for Qmax for pulses larger than 20 ADC counts. The observes overall resolution has many contributions: different number of primary electrons produced, electron loss during the drift, statistical and local variations of the gas gain, signal coupling to the pads and conversion gain plus the noise.

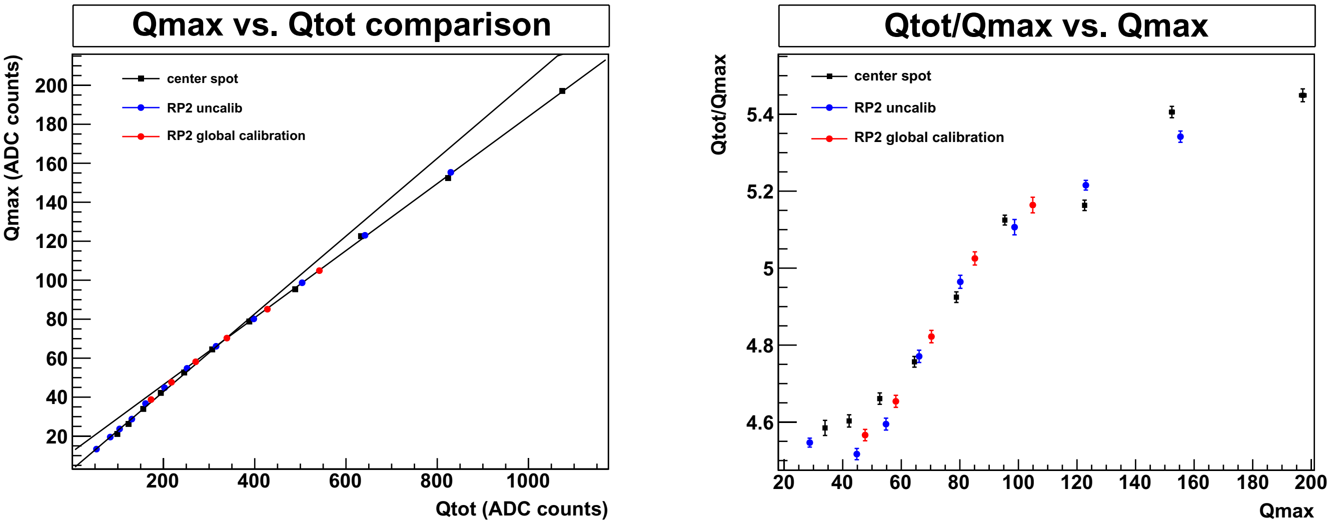

(a) Qmax versus Qtot peak positions. The lines are straight line fits to the lower and upper half of the data points.

(b) The ratio of the peak positions as a function of Qmax.

Figure 5.25: Qmax and Qtot peak positions for both source positions with different gains and calibrations (RP2).

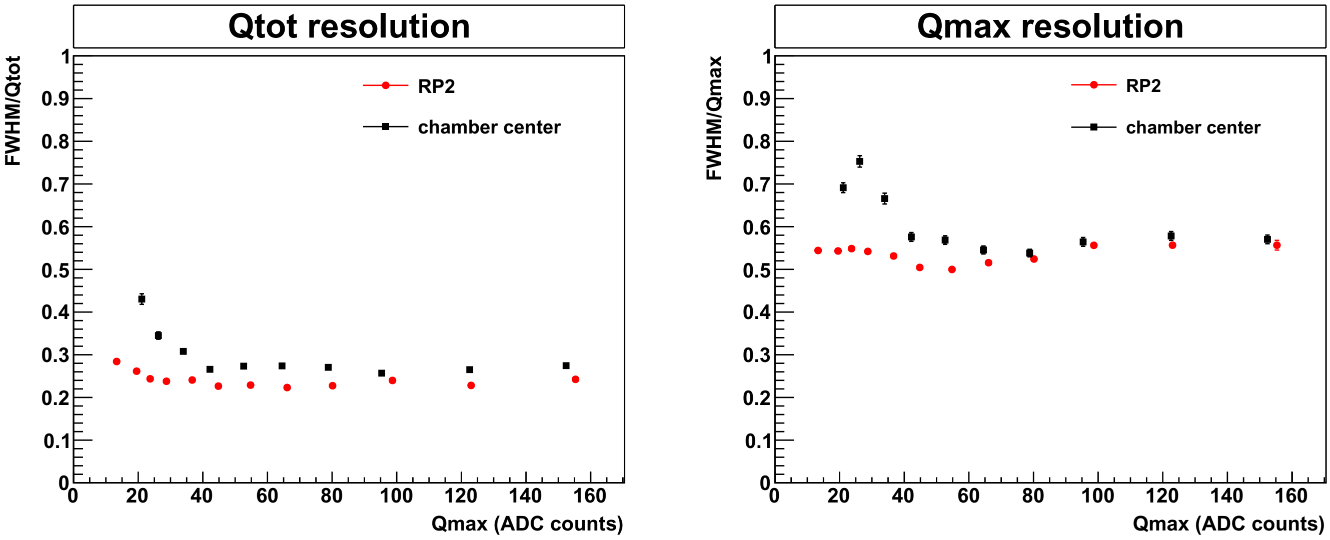

(a)

(b)

Figure 5.26: Enery resolution for Qtot (a) and Qmax (b)

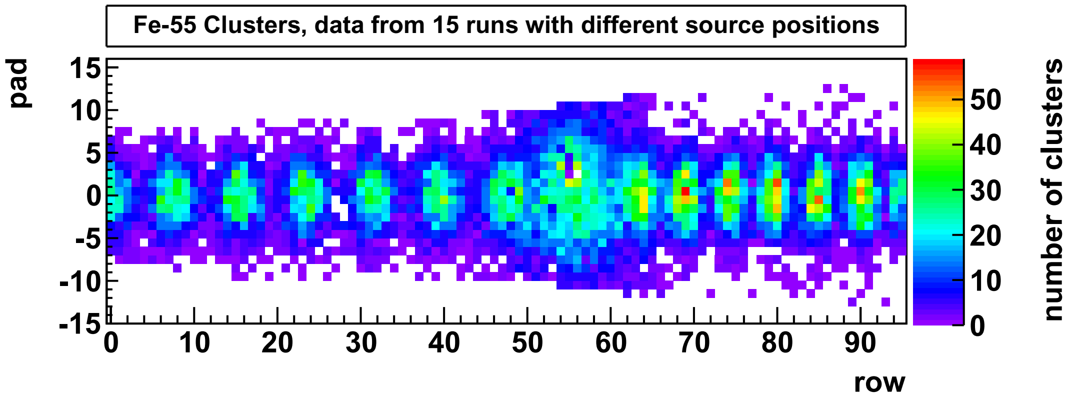

Figure 5.27: Two-dimensional distribution of the clusters in the chamber.

5.4.8 Gain variation across the chamber

In the previous sections the gain was determined for only two selected positions (chamber center and center of RP2). The choice of these position was reasoned by low noise (RP2) and large absorption rates (chamber center). The difference in gain is substantial ($\approx 20\%$) and much larger than expected from the pulser data. However it remains unclear to which extend these variations are caused by different ambient conditions (i. e. pressure, temperature and oxygen content) or if they are truly a feature of the chamber. The pulser data suggests some geometrical imperfections that should also lead to differences in the gas gain.

All this motivated the further investigation of the gain variations across the chamber. For that purpose data were taken with the source positioned at each of the 15 holes (see also figure 3.13) along the row direction. All four readout partitions were read out, with four FECs each. The restriction to only a few FECs reduces the data volume while still detecting about 99% of all absorbed X-rays. All runs were taken in direct succession with stable conditions ($V_{\text{anode}} = 1550$ V; $p = 960$ mbar; $T = 20.5$°C; 24.5 ppm O_2). The analysis is based on the Qmax peak position and takes advantage of the proportionality of the gain and Qmax descibed above. With this method it is possible to determine the gain row-by-row. Consequentially the anode currents were not recorded and no absorption rate is calculated. Is is assumed that the signal coupling to the pads in equal across the chamber. Figure 5.27) show the distribution of the ^{55}Fe clusters, which are separated from the noise by a cut on Qtot (half the global Qtot peak value). It reveals that X-rays are absorbed all along the row position allowing to extract the Qmax for every row. In the range between the holes there are fewer absorbed X-rays; with 1000 events taken for each source position there just enough statistics to extract Qmax.

The variation of the peak position with respect to the row under consideration shows a strong variation across the chamber. With the assumption that the signal coupling to the pads is either constant or adequately described by the calibration the gas gain is proportional to the Qmax peak position. Figure 5.28 shows the the variation of the Qmax peak position across the chamber both for the (global) calibrated data and uncalibrated data. The segmented calibration leads to very similar results as the uncalibrated data.

It is apparent that the Qmax value with the iron source shows a similar qualitative change across the chamber as it was obsevered with calibration pulser data, although much stronger. Overall, Qmax increases to larger row numbers, from row 64 on the pads are larger and pick up a larger fraction of the signal. The calibration does not remove these large variations but leads to slightly smaller differences.

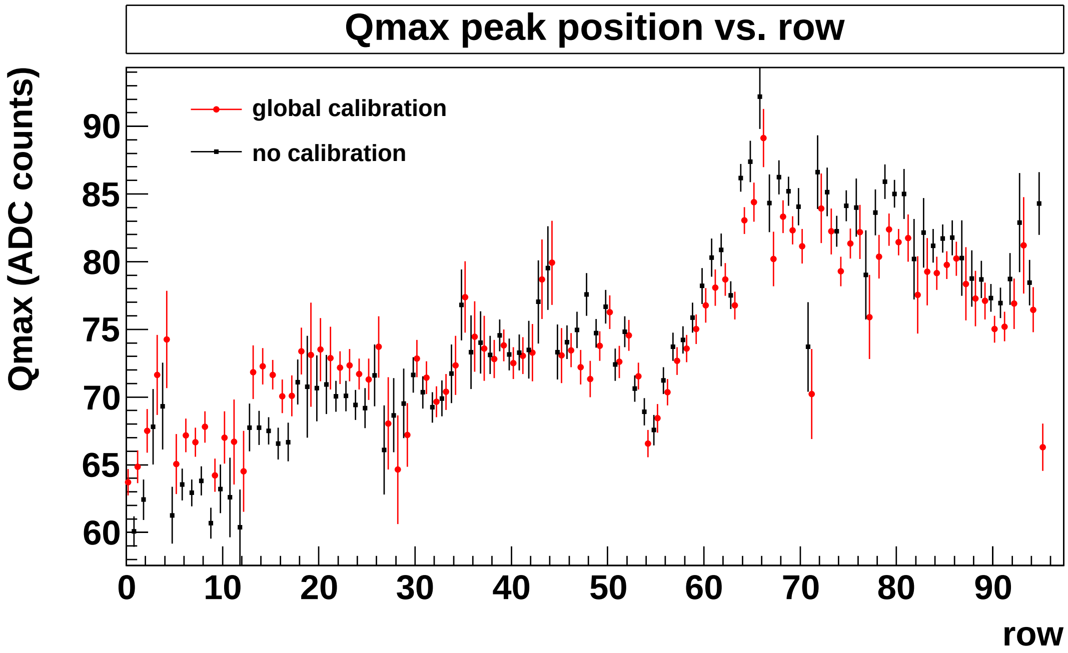

Figure 5.28: Qmax variations across the chamber. The values with/without calibration are slightly displaced to be better visible.

Figure 5.29(a) shows the relative gain variations across the chamber extracted from the pulser and iron data. For the ^{55}Fe data compared to figure 5.28 the step at the padsize boundary was removed by defining the relative gain of rows 63 and 64 to be equal. The pulser data was already normalized to the pad size (see section 5.3). The correlation of the pulser and iron data is most directly seen in figure 5.29(b) and leads to the conclusion that variations seen across the chamber have the same origin for both measurements. It seems plausible that these variations are caused by differences of the anode-padplane and cathode-anode distances. The large fluctuations of the Qmax values from ^{55}Fe data are – at least partially – caused by staticistal uncertainies (only few absorped X-rays in some rows) and the fact that only a small number of pads in each row is contributing enhancing the effect of pad-by-pad differences.

The gain calculated from the Qmax peak positions is shown in figure 5.30 as a function of the distance (radial direction) from the outside edge of the test box, the center hole is located at 629 mm and the center of RP2 at 249 mm. The influence of the different pad sizes was removed as described above. Compared to figure 5.28 and 5.29 all clusters located around the source position are taken into account and the uncalibrated data were used.

The variation of the gain across the chamber is larger than expeced, it reaches a relative difference up to almost 25% for the maximal and minimal gain and can be parametrized by parabola. These large variations are specific to the chamber in the setup and probably caused by mechanical imperfections. The variations seen in the TPC with krypton data (a method very similar to the iron method) are much lower [25].

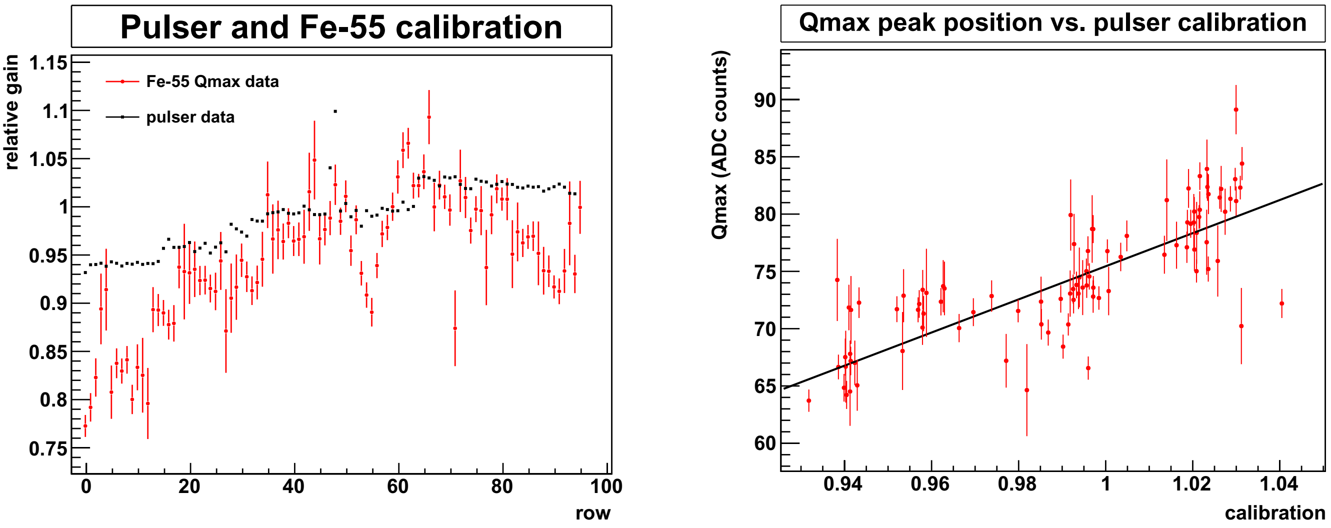

(a) (b)

Figure 5.29: Comparison of the relative gains (calibration) from pulser/iron data (a) and correlation of the iron Qmax value with the pulser calibration (b).

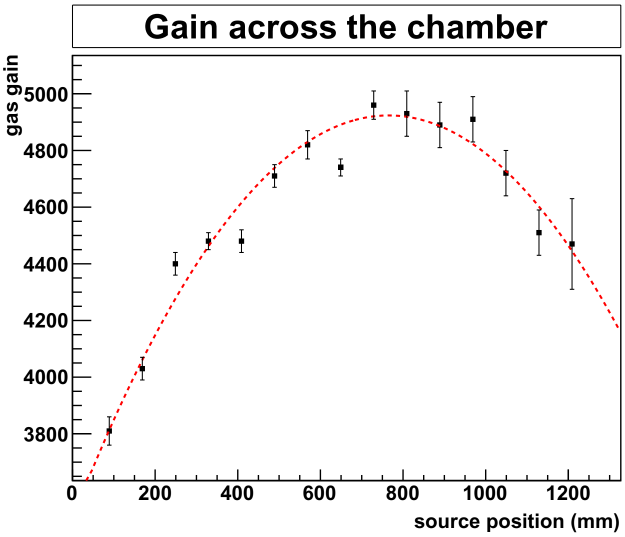

Figure 5.30: Gain variations across the chamber calculated from the Qmax peak position.

5.4.9 Gain variations with pressure and temperature

Relative variations of the gas density lead to a relative change in amplification that can be described by [44]

$$\frac{\mathrm{d}G}{G} = -\alpha \frac{\mathrm{d}\rho}{\rho}$$

where the scaling is determined by the parameter α. The density itself depends on the pressure and temperature, assuming an ideal gas the dependence for the gain becomes

$$\frac{\mathrm{d}G}{G} = -\alpha \left(\frac{\mathrm{d}p}{p} - \frac{\mathrm{d}T}{T} \right).$$

The experimental measurement of α requires data where all other conditions that lead to gain variations are constant (anode and gating voltages, oxygen content and source position). For the measurements described in the previous sections it was aimed at low variations in all these conditions. For the Temperature and oxygen content this is possible at least to some extend, whereas the pressure can not be influenced. To study densitiy-related variations only very few runs are left that have the source at the same position and similar oxygen level (difference <0.5 ppm). The temperature variation in these runs was 21.0 °C ± 0.5 °C with pressures ranging from 954 mbar to 970 mbar. The use of the Qmax peak position to quantify the gain resulted in coefficients $2 < \alpha < 6$ with large uncertainties. This implies a change in gain of 0.2-0.6% per mbar respectively 0.7-2% per °C and agrees with the values given for Ne-CO_2 in [48, 27]. For an investigation of the gain dependence on the oxygen content the recorded data were not sufficient.

5.4.10 Electronics conversion factor

Based on the results of the gas gain and peak positions above the characterization of the electronics is feasible. The total charge collected on the anode wires for one ^{55}Fe cluster is $Q = N_e \cdot e$ where N_e is the total number of electrons created by the avalanche, this is $N_e = n_e \cdot G$ (where $n_e = 167$ denotes the number of primary electrons released and G is the gas gain). The Qtot and Qmax peak positions are shown in figure 5.31 as a function of Q; they do not depend explicitly on the gain.

The linearity seen in figure 5.31 is a consequence of the linear dependence of Qmax and Qtot on the gain, but as apparent from the Qmax vs. Qtot plot (figure 5.25(a)) the Qmax shows an additional nonlinear dependence on the pulse height, or equivalently charge[5] that is due to the zero-supression. The relation of Qmax and Qtot on the charge collected on the anode wire Q can be described as

$$Q_{\mathrm{max}} = Q \cdot \alpha_{\mathrm{max}} \cdot c \cdot G_c = Q \cdot f_{\mathrm{max}}$$

$$Q_{\mathrm{tot}} = Q \cdot \alpha_{\mathrm{tot}}(Q) \cdot c \cdot G_c = Q \cdot f_{\mathrm{tot}}(Q)$$

The *conversion factors* $f_{\{\mathrm{tot,max}\}}$ contain the signal coupling to the pads c, the conversion gain of the electronics G_c and the fraction of the total charge that is detected α. While α_{max} should be constant (i. e. independant of Q), α_{tot} should increase with increasing Q.

Figure 5.32(b) shows the conversion factor f_{max} as a function of total charge on the anode wires Q. It exhibits no dependence on Q (the seemingly drop at low gains is not significant) and is about $f_{\mathrm{max}} = 0.57$ ADC counts/fC. The Qtot conversion factor is shown in figure 5.32(a) and shows a dependence on Q, that suggests saturation for high gains. For high gains it yields about $f_{\mathrm{tot}} \approx 3.1$.

---

[5] More preciesly it depends on the integral of the pulse, the pulse shape in time and the distribution over the pads. The assumption that these are preserved for different pulse amplitudes justifies the dependence only on the amplitude.

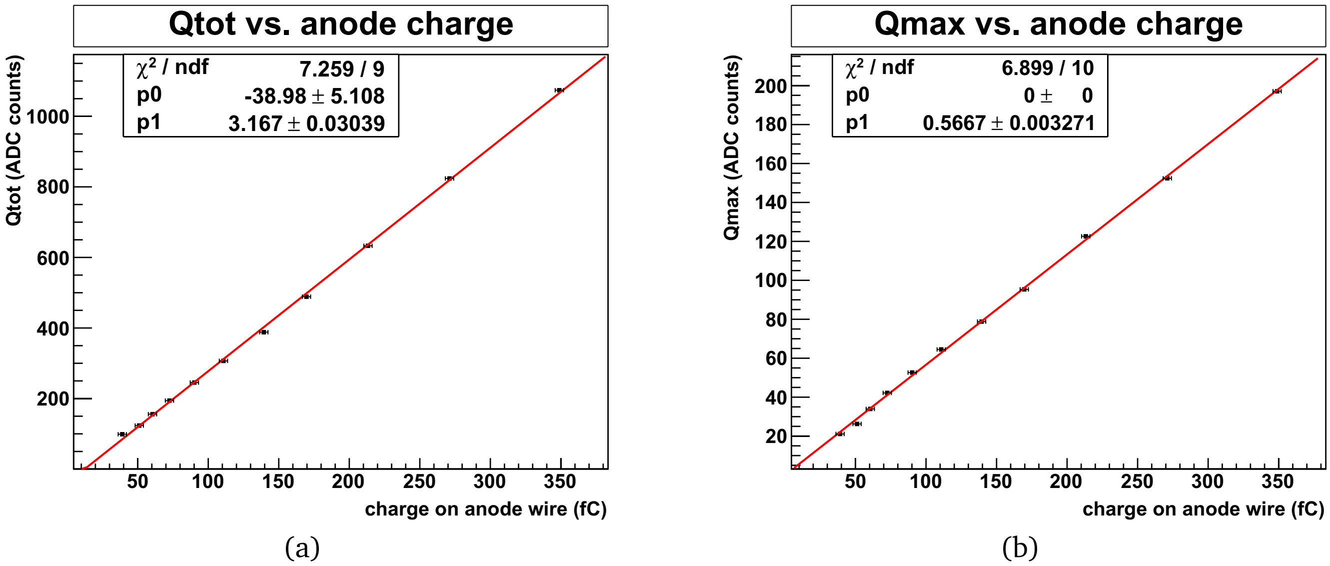

Figure 5.31: The peak positions of Qtot (a) and Qmax (b) as a function of the total charge on the anode wires.

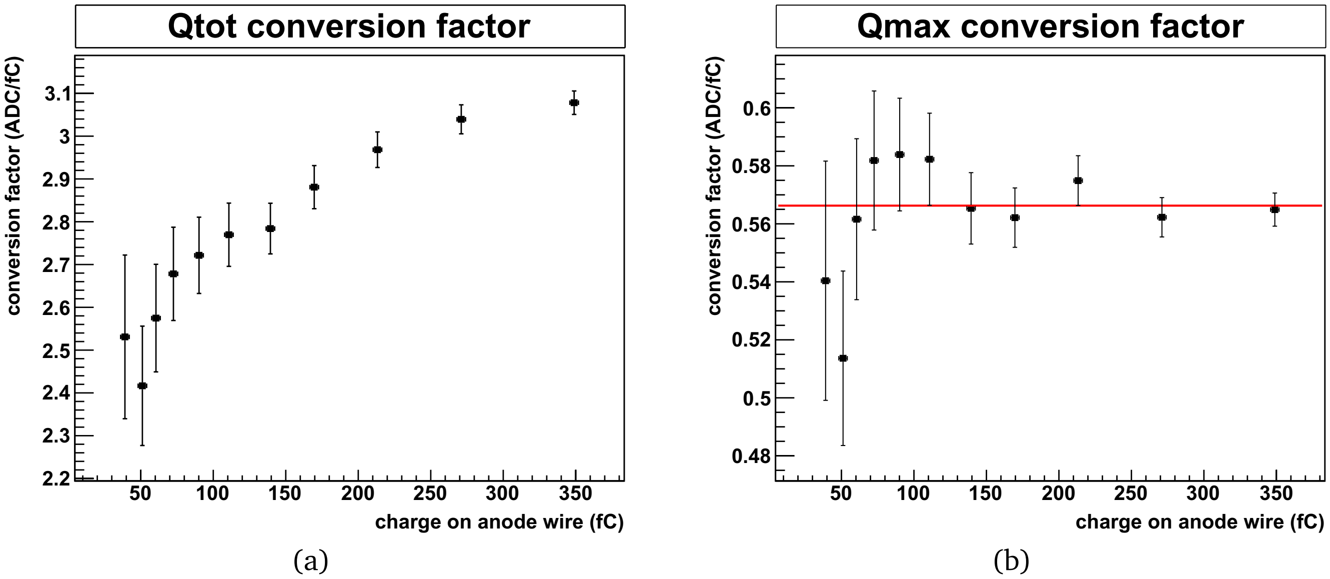

Figure 5.32: The conversion factors for Qtot (a) and Qmax (b) as a function of the gas gain. They are the product of signal coupling to the pads and converstion gain of the electronics. For Qmax they also contain the fraction of the charge in the peak value.

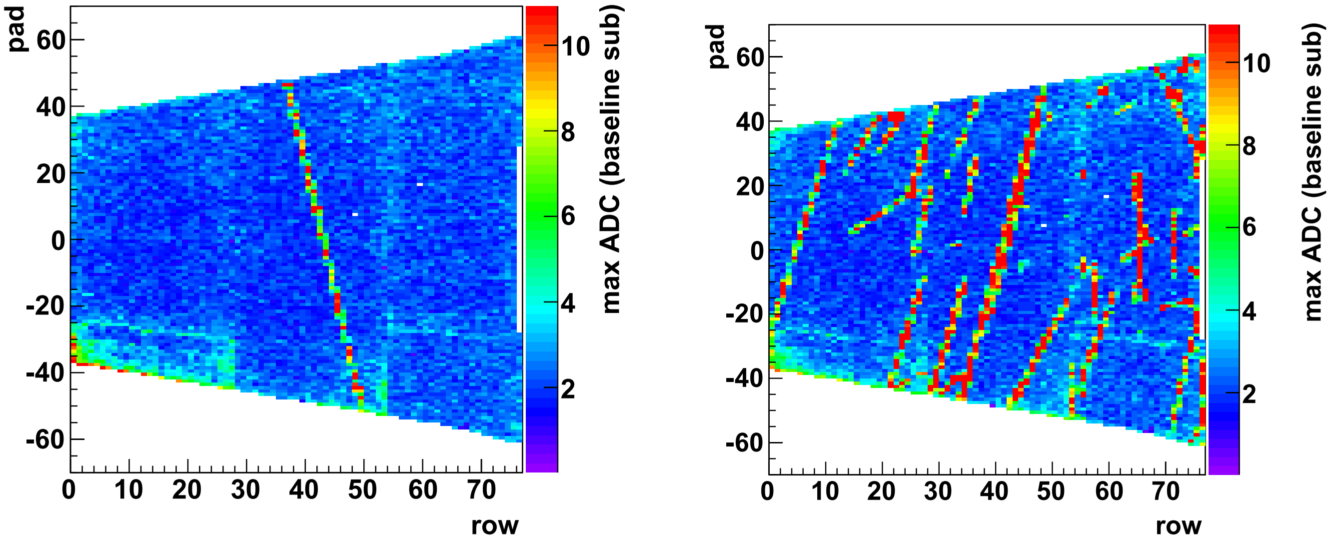

(a) Single particle (probably muon) event.

(b) Cosmic shower.

Figure 5.33: Typical events observed with the cosmic trigger.

5.5 Test of the cosmic trigger

With the setup of the two scintillators in coincidence as a cosmic trigger (see section 3.6.5) connected to the modified DCS boards a few runs were taken to verify that the setup is functional. Compared to the measurements with software trigger a different RCU firmware had to be used which also had a different data format leading to problems with the reading of the data. Different types of cosmic events could be observed with the detector (examples are shown in figure 5.33, events with a single track, a few tracks and many tracks created by cosmics showers.

6 Summary and Outlook

The test setup with one fully equipped sector has been successfully installed and tested. The setup includes a gas box with field cage, one outer readout chamber with the full readout chain and all services. The laser system, that will complete the setup, is intended to become operational in the near future. To achieve this mainly the safety measures and the optics to adjust and guide the beam have to be completed. With laser beams that simulate tracks through the chamber detailed studies on drift velocity, gating efficiency, pad response function, two-track resolution will be possible. For the readout control unit a new firmware became available in April 2009 featuring a new data format and the implementation of the external trigger. It is suggested to test and use this new firmware in the test setup.

The chamber was operating stable at anode voltages up to 1650 V, the incident that occured during early measurement turned out to be attributed to a manufacturing defect. No problems were experienced with the combination of switched off electronics and nominal anode voltage. In the future the chamber could also be operated at higher voltages to inspect the limits.

With the test setup the pedestal and noise behavior of the chamber were investigated. With the use of a radioactive source the gas gain was determined for different anode voltages and local variations of the gain could be observed. The results from these measurements were used to characterize the electronics.

Part of the measurements suffered from large noise and it seems worth to explore possible improvements. It is indicated that improvements can be achieved with a change in the grounding scheme of the electronics corresponding to the TPC, by relocation of the cooling unit and rerouting of the cooling lines and with a shielding of the ethernet connections to the electronics.

Especially for drift velocity studies it seems worth to replace the drift voltage power supply. This would allow measurements at a drift field of 400 V/cm, corresponding to the field in the TPC. If repaired front end cards are available, they could be used to replace defective and high-noise cards in the setup.

A Broken Wire Incident

During gain measurements in the context of first tests of the readout chamber and test setup a wire broke in the evening of August 21st, 2008. At this time the chamber was operated with a gas mixture containing no nitrogen (90% Ne plus 10% CO_2) and an anode voltage of 1500 V (the cover was grounded and the edge was left floating according to the records). Nitrogen acts as a quencher by absorption UV photons and consequently lowers the gain at given voltage.

A large fraction of the FECs were installed in the setup and connected to the pads but since no RCUs and DCS boards were available (and the LV PS was missing) they could not be used for readout and not even be powered up. The pads that were not connected to FECs were grounded through dummy connector cards.

With the electronics not operational the absorption rate was determined with the method of a preamplifier counter connected to the anode wires (see also section 5.4.5). The source was located at the small hole close to the outer edge of the chamber (position 1129 mm in figure 3.5 corresponding to row 90). The absorption rate was determined to $r = 11.8$ kHz[1], with the measured anode currents this resulted in a gas gain of about $G = 2.3 \cdot 10^4$, not noticeably exceeding the nominal gain of $2 \cdot 10^4$ [30]. All chambers installed in the TPC have been tested at even higher gains, the chamber used in the test setup did not pass this test and was thus not installed in the TPC [25].

Several hours before the incident the chambers HV PS had tripped. After that trip the chamber operated at various anode voltages, before the wire broke the voltage was 1500 V for about half an hour. After the incident (which caused the HV PS to trip) the PS for the gating pulsers was also showing a higher current and has been switched off.

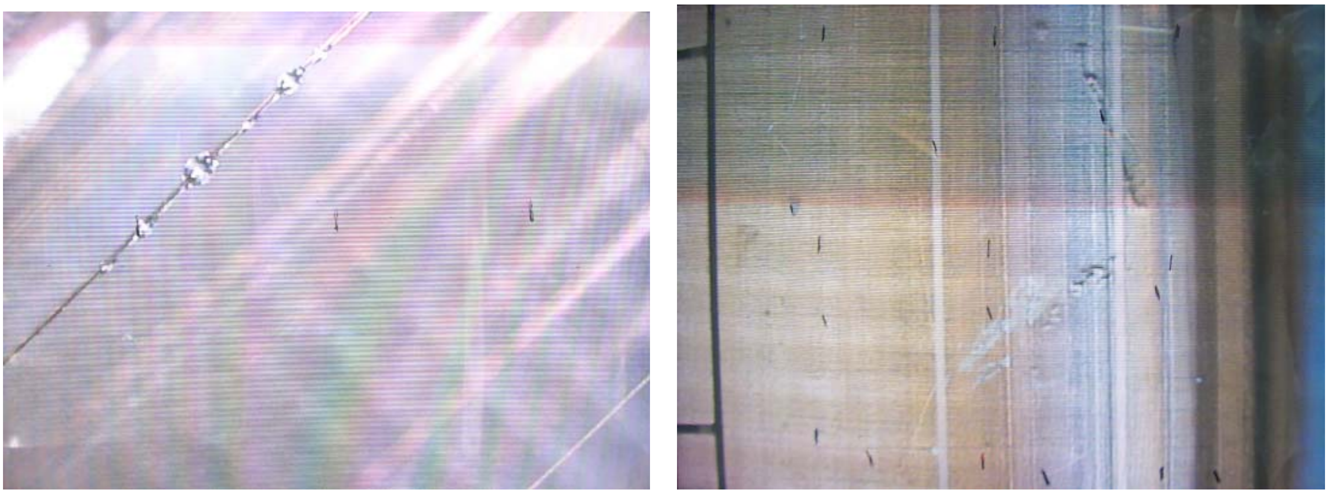

(a) Glue drops on the second edge wire.

(b) Damage of the grounded part of the padplane. The beginning of the readout pads is seen on the lefthand side.

Figure A.1: Inspection of the chamber with a magnifying camera.[49]

---

[1] Note that this matches well with the rates deteremined in section 5.4.5.

A first check for conductive connections between the wire showed that an anode wire in the last partition of anode wires was broken and touching the gating grid. The repair of the chamber took about one week and was conducted in the clean tent by experts from GSI. The broken wire turned out to be the inner one of the thicker (75 μm) edge wires, which is held at anode potential. The inspection of the chamber revealed that the pad plane was damaged on the grounded part (see figure A.1(b)), this is a secondary damage caused by the relatively large currents delivered by the gating pulser. On the second (intact) edge wire drops of glue were found (figure A.1). To be on the safe side this wire has also been replaced. The broken wire was inspected at GSI (figure A.2).

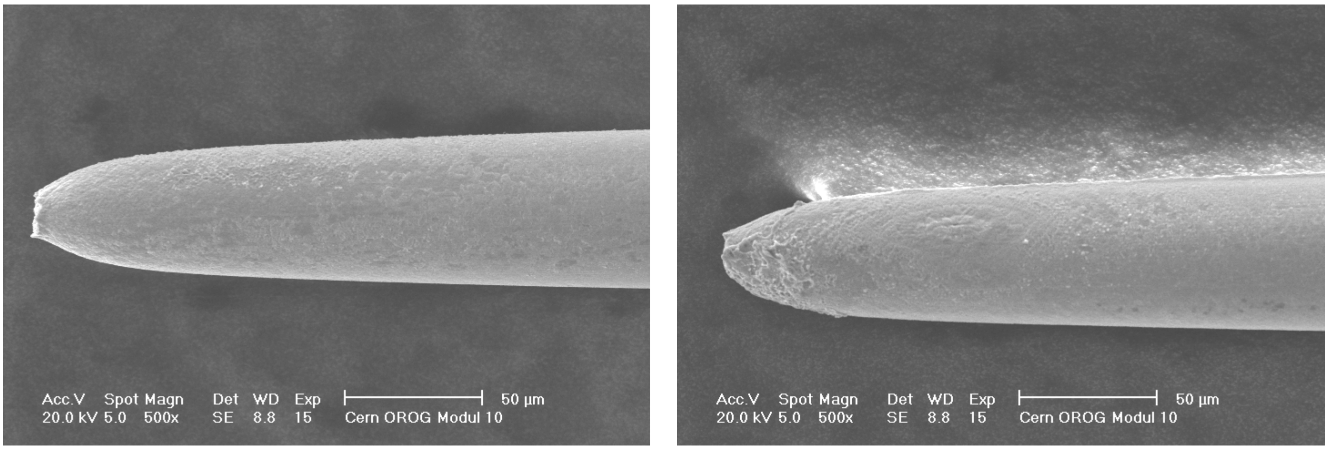

Figure A.2: SEM micrographs of the two endings. [50]

After the repair the chambers edge voltage has been set to 600 V to prevent similar incidents. The chamber has been extensively tested in this configuration, including anode voltages of 1500 V with the Ne-CO_2 gas mixture and was operating stable over many days. All measurements analysed for section 5 have been carried out with the repaired chamber and the Ne-CO_2-N_2 mixture.

It is believed that the wire rip was caused by melting as a result of an electrical discharge between the two edge wires. The outer wire, which is supposed to be held at the edge potential, was mistakenly grounded instead of the intention to leave it floating. This leads to a stronger electric field (and thus higher amplification factors) between the two edge wires and is a prerequisite for a discharge between the wires but cannot explain it alone. One reasonable explanation is that the glue formed not only big drops but also thin films that caused the emission of electrons from the grounded edge wire, in some kind of Malter effect [51]. Positive ions are drifting to the edge wire and deposit charge on the isolating glue film. This causes a higher field towards the wire that provoke the emission of electrons, which are amplified around the anode edge wire and produce more positive ions. Eventually this could lead to an ionization channel between the wires and, in consequence, to a discharge with high current driven by the buffer capacitors. This ultimately could lead to a warm-up weakening the wire, which is pulled apart by the stretching force of 1.2 N. This is however, just a theory.

It it also worth mentioning that the anode dark current was enormously reduced after the repair of the chamber (from 5.3 nA to 1.4 nA for an anode voltage of 1500V with gating open and no source). During the further operation of the chamber the anode dark current was larger, up to 3 nA were observed for 1500 V.

List of Abbreviations

ACORDE	ALICE Cosmic Ray Detector
ADC	Analog-to-Digital Converter
ALICE	A Large Ion Collider Experiment
AliRoot	ALICE ROOT
ALTRO	ALICE TPC Readout
ATLAS	A Toroidal LHC Apparatus
BNC	Bayonet Neill-Concelman
CAMAC	Computer Automated Measurement and Control
CAN	Controller-Area Network
CERN	European Organization for Nuclear Research
CMS	Compact Muon Solenoid
CO_2	Carbon dioxide
CsI	Caesium Iodide
CTP	Central Trigger Processor
CuBe	Copper-Beryllium
D-RORC	DAQ-RORC
DAQ	Data Acquisition
DATE	Data Acquisition and Test Environment
DCS	Detector Control System
DDL	Detector Data Link
DDL-SIU	DDL Source Interface Card
DHCP	Dynamic Host Configuration Protocol
DID	DIM Information Display
DIM	Distributed Information Management system
DIU	Destination Interface Card
EmCAL	Electromagnetic Calorimeter
FCB	Front-End Control Bus
Fe	Iron
FEE	Front-End Electronics
FMD	Forward Multiplicity Detector
FPGA	Field-Programmable Gate Array
FWHM	Full Width at Half Maximum
GSI	GSI Helmholtzzentrum für Schwerionenforschung GmbH
GTL	Gunning Transceiver Logic
GUI	Graphical User Interface
HLT	High-Level Trigger
HMPID	High Momemtum Particle Identification Detector
HV	High Voltage
IP	Interaction Point
IROC	Inner Readout Chamber
ITS	Inner Tracking System
JTAG	Joint Test Action Group
L0	Level-0 trigger
L1	Level-1 trigger

L2	Level-2 trigger
LDC	Local Data Concentrator
Pb-Pb	lead-lead
LHC	Large Hadron Collider
LTU	Local Trigger Uni
LV	Low Voltage
LVDS	Low-Voltage Differential Signaling
LVTTL	Low-Voltage TTL
MRPC	Multi-gap Resistive Plate Chamber
MWPC	Multi-Wire Proportional Chamber
N_2	Nitrogen
Ne	Neon
NFS	Network File System
NIM	Nuclear Intrumentation Module
OLE	Object Linking and Embedding
OPC	OLE for Process Control
OROC	Outer Readout Chamber
p-A	proton-nucleus
PASA	Preamplifier/Shaping Amplifier
PC	Personal Computer
PCB	Printed Circuit Board
PCI	Peripheral Component Interconnect
PCI-X	PCI extended
PHOS	Photon Spectrometer
PID	Particle Identification
PMD	Photon Multiplicity Detector
p-p	proton-proton
ppm	parts-per-million
PS	Power Supply
PSU	Power Supply Unit
PVSS	Prozessvirtualisierungs- und Steuerungs-System
PWO	Lead-tungstate, $PbWO_4$
QCD	Quantum chromodynamics
QGP	Quark-Gluon Plasma
RCU	Readout Control Unit
RICH	Ring Imaging Cherenkov
ROC	Readout Chamber
RORC	Readout Receiver Card
RP	Readout Partition
RS-232	Recommended Standard 232
SDD	Silicon Drift Detector
SHV	Safe High Voltage
SIU	Source Interface Card
SPD	Silicon Pixel Detector
SSD	Silicon Strip Detector
SSH	Secure Shell
T0	Time-0 detector
TCP/IP	Transmission Control Protocol/Internet Protocol
TOF	Time-Of-Flight Detector
TPC	Time Projection Chamber

TRD	Transition Radiation Detector
TTC	Trigger and Timing Circuit
TTCRx	TTC Receiver
V0	Vertex-0 detector
VI	Virtual Instrument
YAG	Yttrium Aluminum Garnet ($Y_3Al_5O_{12}$)
ZDC	Zero Degree Calorimeter
ZEM	ZDC Electromagnetic detector
ZN	ZDC Neutron detector
ZP	ZDC Proton detector

Bibliography

[1] ALICE Collaboration, *Technical Proposal for a Large Ion Collider Experiment at the CERN LHC*, CERN, 1995, CERN/LHCC/95-71, LHCC/P3.

[2] ALICE Collaboration, The ALICE Experiment at the CERN LHC, *Journal of Instrumentation*, 3(08):S08002, 2008.

[3] ALICE Collaboration, http://aliceinfo.cern.ch.

[4] *Definition of the ALICE Coordinate System and Basic Rules for Sub-detector Components Numbering*, CERN, Geneva, 2003, ALICE-INT-2003-038.

[5] C. Lippmann and D. Vranic, ALICE TPC Numbering Conventions, 2007.

[6] ALICE Collaboration, *Technical Design Report of the Inner Tracking System (ITS)*, CERN, Geneva, 1999, CERN/LHCC 99-12, ALICE TDR 4.

[7] Jens Wiechula, *Commissioning and Calibration of the ALICE-TPC*, Dissertation, 2008.

[8] ALICE Collaboration, *Technical Design Report of the Transition Radiation Detector*, CERN, Geneva, 2001, CERN/LHCC-2001-021, ALICE TDR 9.

[9] ALICE Collaboration, *Addendum to the Technical Design Report of the Time of Flight System (TOF)*, CERN, Geneva, 2002, CERN/LHCC 2002-016, Addendum to ALICE TDR 8.

[10] ALICE Collaboration, *Technical Design Report of the High Momentum Particle Identification Detector*, CERN, Geneva, 1998, CERN/LHCC 98-19, ALICE TDR 1.

[11] ALICE Collaboration, *Technical Design Report of the Photon Spectrometer (PHOS)*, CERN, Geneva, 1999, CERN/LHCC 99-4, ALICE TDR 2.

[12] D. C. Zhou (for the ALICE Collaboration), PHOS, the ALICE-PHOton spectrometer, *Journal of Physics G: Nuclear and Particle Physics*, 34(8):S719–S723, 2007.

[13] Hisayuki Torii (for the ALICE-PHOS Collaborations), The ALICE PHOS Calorimeter, *Journal of Physics: Conference Series*, 160:012045 (6pp), 2009.

[14] ALICE Collaboration, *The Electromagnetic Calorimeter - Addendum to the Technical Proposal*, CERN, Geneva, 2006, CERN-LHCC-2006-014, CERN/LHCC 96-32-Add3.

[15] ALICE Collaboration, *Electromagnetic Calorimeter - Technical Design Report*, CERN, Geneva, 2008, CERN-LHCC-2008-014, ALICE-TDR-014.

[16] ALICE Collaboration, *The forward muon spectrometer - Addendum to the ALICE Technical Proposal*, CERN, Geneva, 1996, CERN/LHCC 96-53, LHCC/P3-Addendum 1.

[17] ALICE Collaboration, *Technical Design Report of the Dimuon Forward Spectrometer*, CERN, Geneva, 1999, CERN/LHCC 99-22, ALICE TDR 5

[18] ALICE Collaboration, *Addendum to the Technical Design Report of the Dimuon Forward Spectrometer*, CERN, Geneva, 2000, CERN/LHCC 2000-046, Addendum 1 to ALICE TDR 5.

[19] ALICE Collaboration, *Technical Design Report of the Zero Degree Calorimeter (ZDC)*, CERN, Geneva, 1999, CERN/LHCC 99-5, ALICE TDR 3.

[20] A. De Falco, R. Arnaldi, E. Chiavassa, C. Cicalo, P. Cortese, N. De Marco, G. Dellacasa, A. Ferretti, M. Floris, M. Gagliardi, M. Gallio, R. Gemme, A. Masoni, P. Mereu, A. Musso, C. Oppedisano, A. Piccotti, F. Poggio, G. Puddu, E. Scomparin, S. Serci, E. Siddi, D. Stocco, G. Usai, E. Vercellin, and F. Yermia. Zero degree Cherenkov calorimeters for the ALICE experiment. *RICH 2007 - Proceedings of the Sixth International Workshop on Ring Imaging Cherenkov Detectors*, volume 595, pages 267 – 269, 2008.

[21] ALICE Collaboration, *Technical Design Report of the Photon Multiplicity Detector (PMD)*, CERN, Geneva, 1999, CERN/LHCC 99-32, ALICE TDR 6.

[22] ALICE Collaboration, *Addendum to the Technical Design Report of the Photon Multiplicity Detector (PMD)*, CERN, Geneva, 2003, CERN /LHCC 2003-038, Addendum 1 to ALICE TDR 6.

[23] ALICE Collaboration, *Technical Design Report on Forward Detectors: FMD, T0 and V0*, CERN, Geneva, 2004, CERN-LHCC-2004-025, ALICE-TDR-011.

[24] A. Fernandez, S. Kartal, and C. Pagliarone. ACORDE – A Cosmic Ray Detector for ALICE, 2006.

[25] Chilo Garabatos, Private communication.

[26] Danilo Vranic, Private communication.

[27] R. Veenhof, *Choosing a gas mixture for the ALICE TPC*, ALICE-INT-2003-29, 2003.

[28] C. Garabatos. The ALICE TPC, *Nuclear Instruments and Methods in Physics Research A*, 535(1-2):197 – 200, 2004, Proceedings of the 10th International Vienna Conference on Instrumentation.

[29] C. Garabatos G. Augustinski P. Braun-Munzinger H. Daues J. Fiess U. Frankenfeld P. Glässel J. Hehner M. Ivanov R. Renfordt H. Sann H.R. Schmidt H. Stelzer, D. Vranic and B. Windelband. The ALICE TPC Readout Chamber: From Prototype to Series Production, ALICE-INT-2003-017, 2003.

[30] ALICE Collaboration, ALICE time projection chamber: Technical Design Report, CERN, Gevenva, 2000, ALICE TDR 7.

[31] L. Musa, J. Baechler, N. Bialas, R. Bramm, R. Campagnolo, C. Engster, F. Formenti, U. Bonnes, R. Esteve Bosch, U. Frankenfeld, P. Glassel, C. Gonzales, H.-A. Gustafsson, A. Jimenez, A. Junique, J. Lien, V. Lindenstruth, B. Mota, P. Braun-Munzinger, H. Oeschler, L. Osterman, R. Renfordt, G. Ruschmann, D. Rohrich, H.-R. Schmidt, J. Stachel, A.-K. Soltveit, and K. Ullaland, The ALICE TPC front end electronics, *Nuclear Science Symposium Conference Record, 2003 IEEE*, 5:3647–3651 Vol.5, Oct. 2003.

[32] R Campagnolo, J Baechler, R Bramm, Claude Engster, R Esteve-Bosch, C Gonzalez-Gutierrez, A Jimenez de Parga, A Junique, B Mota, L Musa, H Helstrup, J A Lien, D Roehrich, K Ullaland, H K Soltveit, Hans Ake Gustafsson, and L Oesterman. Performance of the ALICE TPC fron end card, 2003.

[33] A.J. Mota B. Musa L. Bosch, R.E. de Parga, The ALTRO chip: a 16-channel A/D converter and digital processor for gas detectors. *IEEE Transactions on Nuclear Science*, 50(6):2460–2469, 2003.

[34] *ALICE TPC Readout Chip User Manual*, CERN EP/ED, CERN, Geneva, 2002.

[35] R.; Junique A.; Musa L.; Alme J.; Lien J.; Pommersche B.; Richter M.; Roed K.; Rohrich D.; Ullaland K.; Alt T. Gutierrez, C.G.; Campagnolo, The ALICE TPC Readout Control Unit, *Nuclear Science Symposium Conference Record, 2005 IEEE*, 1:575–579, 2005.

[36] J. A. Lien *The Readout Control Unit of the ALICE TPC*, PhD thesis, Bergen TU, Bergen, Dec 2004.

[37] *RCU Firmware V2 User Manual*, CERN, Geneva, 2008.

[38] ALICE Collaboration, *Technical Design Report of the Trigger, Data Acquisition, High-Level Trigger and Control System*, CERN, Geneva, 2004, CERN-LHCC-2003-062, ALICE TDR 10.

[39] W. Carena, S. Chapeland, O. Cobanoglu, E. Denes, R. Divia, U. Fuchs, A. Hirn, S. Lord, J.C. Marin, I. Makhlyueva, K. Schossmaier, C. Soos, P. Vande Vyvre, T. Anticic, F. Carena, *ALICE DAQ and ECS User's Guide*, Alice internal note/daq, 2006, ALICE-INT-2005-015,

[40] ALICE DATE V5 User's Guide, ALICE Internal note/DAQ ALICE-INT-2005-015, CERN, Geneva, 2006.

[41] England Spectron Laser Systems, Rugby, *SL400 Series Pulsed Nd:YAG Laser, User Manual*, April 1996, Publication No. PB05002 Issue 3.

[42] ROOT: An Object Oriented Data Analysis Framework, http://root.cern.ch.

[43] Huo Junde, Nuclear Data Sheets for A = 55, *Nuclear Data Sheets*, 109(4):787 – 942, 2008.

[44] F. Sauli, *Principles of Operation of Multiwire Proportional and Drift Chambers*, CERN, Geneva, 1977, CERN 77-09.

[45] W. Blum and L. Rolandi, *Particle Detection with Drift Chambers*, Springer-Verlag, 1993.

[46] iseg Spezialelektronik GmbH, *Bedienungsanleitung CHQ x2xx Präzisions CAMAC Hochspannungsquelle der Baureihe CHQ HIGH PRECISON*, 2002.

[47] G. F. Knoll, *Radiation Detection and Measurement*, John Wiley & Sons, 2000.

[48] Juan F. Castillo Hernandez, *Development of a Ternary Mixture Monitor*, 2005.

[49] Michael Träger, Private communication.

[50] Jörg Hehner, Private communication.

[51] Louis Malter, Thin film field emission, *Phys. Rev.*, 50(1):48–58, Jul 1936.

[52] ALICE Collaboration, ALICE: Physics Performance Report, Volume I, *Journal of Physics G: Nuclear and Particle Physics*, 30(11):1517–1763, 2004.

[53] ALICE Collaboration, ALICE: Physics Performance Report, Volume II, *Journal of Physics G: Nuclear and Particle Physics*, 32(10):1295–2040, 2006.

[54] Luciano Musa, The time projection chamber for the ALICE experiment. *Nuclear Physics A*, 715:843c – 848c, 2003, Quark Matter 2002, Proceedings of the 16th International Conference on Ultra-Relativistic Nucleus-Nucleus Collisions.

[55] H. J. Eichler J. Eichler, *Laser: Bauformen, Strahlführung, Anwendungen*, 6. Auflage, Springer-Verlag, 2006,

[56] K. Kleinknecht, *Detektoren für Teilchenstrahlung*, 4. Auflage, Teubner Verlag, 2005.

[57] P. Braun-Munzinger H. Daues J. Fiess C. Garabatos J. Hehner M. Ivanov R. Renfordt H. Sann H.R. Schmidt H. Stelzer D. Vranic U. Frankenfeld, G. Augustinski. The ALICE TPC Inner Readout Chamber: Results of Beam and Laser Tests, ALICE-INT-2002-030, 2002.

Acknowledgments

First of all I would like to thank Prof. Dr. Peter Braun-Munzinger, who gave me the opportunity to write this thesis and participate in the unique ALICE experiment and Dr. Chilo Garabatos, my supervisor at CERN, who supported me in so many aspects. Many thanks also for proofreading my thesis.

I would also like to thank all those who have supported me to get the detector up and running, I know I bothered them sometimes. Many thanks to Jens Wiechula for the discussions and the support with AliRoot, I learned a lot from him. Also many thanks to Thomas Morhardt and Dr. Danilo Vranic for the great support during my time at CERN. Many Thanks to the electronics experts Dr. Luciano Musa, Dr. Christian Lippmann, Magnus Mager, Antoine Junique and Attiq Rehman. Thanks also to Dr. Filippo Costa from the DAQ Group and to Dr. Ulrich Frankenfeld. To Michael Träger and Jörg Hehner many thanks for repairing the wire that broke during my measurements. Special thanks to Yisel Martinez, it was pleasure to work with her during the summer.

Thanks also to the people from “Casa Rudi”, Dr. Hans-Rudolf Schmidt, Dr. Ulrich Frankenfeld, Prof. Dr. Peter Glässel, Jens Wiechula, Daniel Soyk and Patrick Schmidt, it was always a pleasure to stay there.

Last but not least I want to thank my parents and my brother, they have supported me throughout my studies. Special thanks to my father for proofreading my thesis.

Erklärung zur Diplomarbeit

Hiermit versichere ich die vorliegende Diplomarbeit ohne Hilfe Dritter nur mit den angegebenen Quellen und Hilfmitteln angefertigt zu haben. Alle Stellen, die aus Quellen entnommen wurden, sind als solche kenntlich gemacht. Diese Arbeit hat in gleicher oder ähnlicher Form noch keiner Prüfungsbhörde vorgelegen.

Darmstadt, den 22. Mai 2009

Michael Linus Knichel